②

主論文

# Search for $H$ dibaryon in $\Sigma^- p$ decay with scintillating fiber target as triggerable visual detector

Yoshitaka Itow

A dissertation submitted in partial fulfillment of
the requirements for the degree of

Doctor of Science

Department of Physics
Kyoto University

**Abstract**

A $H$ dibaryon search via $(K^-, K^+)$ reactions has been performed with a novel visual detector, scintillating fibers, as a triggerable active target using KEK 12-GeV Proton Synchrotron. The target is made of 30,000 plastic scintillating fibers and viewed by two sets of image intensifier tubes. The tracks are clearly identified as the images of photons in the pictures obtained with the image intensifier tubes. The position resolution of tracks has been obtained to be 290 $\mu$m. The target has been used for detecting three-dimensional images of $(K^-, K^+)$ reactions and decay products of the $H$. The $H$ dibaryon through the direct production process, $K^- + C \rightarrow K^+ + H + X$ followed by the sequential weak-decay, $H \rightarrow \Sigma^- + p$, then $\Sigma^- \rightarrow \pi^- + n$ , has been searched in about 8,000 pictures of $(K^-, K^+)$ reactions obtained with the target.

No evidence for the $H$ has been observed. The upper limit for the production cross section of $H$ has been obtained to be 0.35 $\mu$b to 0.5 $\mu$b for the $H$ mass of 2200 to 2230 MeV/$c^2$ and the lifetime of $10^{-10}$ to $10^{-9}$ sec with assumption that the decay branching ratio for $\Sigma^- p$ channel is 100% .

# Contents

Appendix

# 1 Introduction

## 1.1 $H$ dibaryon

In spite of the complex aspect of non-pertubative QCD, a simple picture of the naive quark-model of hadron, in which there are 3 quarks ($qqq$) in a baryon and quark-antiquark ($q\overline{q}$) in a meson, has been successful for describing the attributes of hadrons such as the charge, spin, and the magnetic moment. The mass of hadron has been discussed with various effective models which could describe the mass spectrum of hadrons. In these models the origins of mass is considerably different from each other. Also the models tell us little about the mechanism of the quark confinement which has been a long standing problem of hadron physics.

An extension of the quark picture leads us to possible existence of multi-quark states ($q^n\overline{q}^m$), so-called exotic hadrons. The existence of these exotics particles is closely related to the mechanism of the quark confinement. Both theoretical and experimental studies have been made on exotic hadrons [1] such as "baryionium" ($qq\overline{qq}$), "penta-quark" ($qqqq\overline{q}$), "hybrid meson" ($q\overline{q}g$) and "dibaryon" ($q^6$) in order to solve the long-standing problem of the quark confinement.

A six quark state ($q^6$) was studied by Jaffe in the framework of the MIT-bag model in 1977 [2]. He proposed the existence of a flavor-singlet dihyperon ($uuddss$), the $H$ dibaryon, which has strangeness -2 and is an iso-singlet ($I$=0) and spin-singlet ($J$=0) state. The predicted mass is 2150 MeV/$c^2$ so that the $H$ is stable against strong decay into $\Lambda\Lambda$ ($2M_\Lambda$=2230MeV/$c^2$). Such a large binding energy is originated in the "color magnetic interaction" due to the one-gluon exchange between quarks. This interaction is known to be important in the mass splitting of light hadrons.

For a N-quark hadron the color magnetic interaction is written as;

$$\Delta = \{8N - \frac{1}{2}C_6 + \frac{4}{3}J(J+1)\}\bar{M}, \tag{1}$$

where $N$ is the total number of quarks, $J$ is their angular momentum, and $C_6$ is the Casimir operator of SU(6) for the color-spin representation of the quarks. The $\bar{M}$ is the average interaction length. The mass of the hadron, $M$, is given by the formula;

$$M = \frac{4}{3}(4\pi B)^{1/4}[2.043N - z_0 + \alpha_c\Delta]^{3/4}, \tag{2}$$

where $B^{1/4}$ = 146 MeV, $z_0$=1.84, and $\alpha_c = g^2/4\pi$ =0.55. These parameters have been determined to reproduce the hadron mass spectra. With the most symmetric configuration for the color, spin and flavor of quarks, $C_6$ takes the largest value, 144, which results in the large mass shift of the $H$ below $2\Lambda$.

Since then, many papers have been devoted to calculate its mass with various models, such as the bag model [3, 4, 5], the quark cluster model [6, 7, 8], the skyrme model [9, 10], the Lattice QCD [11] and so on. Many of these calculations suggest that the $H$ is bound although predicted masses are scattered in wide range ( 1800 MeV/$c^2$ $\sim$ $2\Lambda$ mass ).

## 1.2 Experimental studies

Experimental studies have been made to search for the $H$ in two ways. One is to search for the signal in the missing mass spectrum for the production channel. The other is direct detection of the decay products.

At BNL, the $H$ was searched for in the missing mass spectrum of the reaction $p + p \rightarrow K^- + K^+ + H$. It gave an upper limit for the production cross section, 30-130 nb in the $M_H$ range from 2000 MeV/$c^2$ to 2500 MeV/$c^2$ (90% C.L.) [12], whereas the expected production cross section [13] is two orders of magnitude smaller than the obtained limit.

The existence of tightly bound $H$ was examined in the nuclear double beta decay processes, ${}^A_N N \rightarrow^{A-2}_{Z-1} N + H + \beta^+ + \nu$ and ${}^A_N N \rightarrow^{A-2}_{Z} N + H + \gamma$ [14]. The lower mass limit was obtained to be 1875.1 MeV/$c^2$, a few MeV/$c^2$ below the two neucleon mass.

Recently, observations of several weak-decay events of the $H$ have been reported by a group from Dubna. A propane bubble chamber has been exposed to 10-GeV/$c$ proton beams [15, 16]. They have claimed by means of a kinematically fitting method that neutral "Vee" particles have been interpreted as the $H$ decaying into $\Sigma^- p$. Another experiment has shown the $H \rightarrow \Lambda p \pi^-$ decay in a spark chamber with a Cu target exposed to neutron beam [17]. There remains, however, other possible interpretations for these events [18]. The $H \rightarrow \Sigma^- p$ event can be faked by inelastic scattering of $\Lambda$ such as $\Lambda + n \rightarrow \Sigma^- + p$. The $H \rightarrow \Lambda p \pi^-$ event can be faked by a two $\Lambda$ production event where one of the $\Lambda$ changes the direction by the elastic scattering. The identification of double strangeness transfer at the production point of $H$ is indispensable to deny such interpretations.

To improve the experimental significance it is desirable to identify both double strangeness transfer in the production channel and/or sequential weak decays in the decay channel. Dover et al pointed out in 1982 [19, 20] that the $(K^-, K^+)$ reaction on a nucleus target is a good channel for this purpose. In this reaction two production processes of the $H$ are considered. One is the direct $H$ production process;

$$K^- + (pp) \rightarrow K^+ + H, \tag{3}$$

where $(pp)$ is a proton pair inside a nucleus. The other is the $\Xi^-$ absorption process;

$$\Xi^- + (p) \rightarrow H + X, \tag{4}$$

where $(p)$ is a proton in a nucleus. The $\Xi^-$ produced via a $(K^-, K^+)$ reaction is slowed down by ionization and is captured in an atomic orbit.

In 1989 an emulsion-counter hybrid experiment (KEK-E176) using the $(K^-, K^+)$ reaction was performed at KEK. In this experiment, $(K^-, K^+)$ interaction points were determined with a $K^+$-spectrometer and $\Xi^-$'s produced at the first vertex were tagged. The $H$ was searched in $(K^-, K^+)$ reactions as well as in $\Xi^-$ absorption reactions with the emulsion target. The signal of the direct $H$ production via $(K^-, K^+)$ reaction was searched in the $K^+$ momentum spectrum. The result gave an upper limit for the production cross section to be 0.2%-0.6% ( 90% C.L.) of the quasi-free $\Xi^-$ production in the mass range of 1900 MeV/$c^2$-2160 MeV/$c^2$ [21]. The decay products of $H \rightarrow \Sigma^- p$ channel were also searched in the volume of 1 mm$^3$ around the $\Xi^-$ absorption points in emulsion. No evidence of the $H$ decay was found, and the upper limit for the $H$ production was deduced as 6% (90% C.L.) [22]. The result, however, was limited for the $H$ with short life ($\leq 10^{-10}$sec) due to the small fiducial volume of the scanning. Therefore, the question is still open for the $H$ with longer lifetime ($\geq 10^{-10}$sec).

Recently, the reaction, $\Xi^- + d \rightarrow H + n$, has been measured at BNL using tagged $\Xi^-$'s via $(K^-, K^+)$ reactions [23, 24]. The signal of the $H$ production is to be searched for in the neutron energy spectrum. The first result will appear soon [24].

## 1.3 Relation between the $H$ particle and double hyper-nuclei

The $H$ as a six quark state ($q^6$) is interesting also from the viewpoint of baryon-baryon interaction including the strangeness quantum number. Experiments on hyperon-neucleon scattering performed with a bubble chamber in 1960's have not provided enough data to determine either hyperon-neucleon or hyperon-hyperon interactions.

Another information is derived from the studies of double $\Lambda$ hyper-nuclei. More than 20 years ago, two events with double $\Lambda$ hyper-nuclei in emulsion were reported [25, 26]. In KEK-E176, a few cascade weak decays of double $\Lambda$ hyper-nuclei were found in about 100 candidates of $\Xi^-$ absorption at rest in emulsion [27]. One of the events was determined as either ${}^{10}_{\Lambda\Lambda}Be$ or ${}^{13}_{\Lambda\Lambda}B$. The binding energy of $2\Lambda$ ($B_{\Lambda\Lambda}$) was determined to be $8.5 \pm 0.7$ MeV for ${}^{10}_{\Lambda\Lambda}Be$ or $27.6 \pm 0.7$ MeV for ${}^{13}_{\Lambda\Lambda}B$. If the $H$ mass is less than $2\Lambda$ mass, the transition ${}^{A}_{\Lambda\Lambda}Z \rightarrow H +^{A-2} Z$ takes place through the strong interaction. Thus the lower limit of the $H$ mass might be deduced to be $2203.7 \pm 0.7$ MeV/$c^2$ from the larger $B_{\Lambda\Lambda}$. However, the possibility is still open for the H heavier than 2200 MeV/$c^2$. There has been, so far, no definite answer to its existence.

## 1.4 Motivation of the present experiment

Although the nuclear emulsion method has a very high spatial resolution ($\sim$1 $\mu$m), the effective volume to search for weak-decay products of neutral particles is limited within 1 mm$^3$, and the number of exposed beam particles is limited since it has no time resolution. The limits in previous experiments can be overcome by a counter hybrid technique together with a novel active target which has a large effective volume and a good time resolution.

Recently, scintillating fiber detectors have been developed for high-resolution trackers [29, 30, 31, 32], "spaghetti" calorimeters [33, 34, 35] and active targets [36, 37, 38, 39] for high-energy physics experiments. Furthermore the rapid progress in the opto-electronics technology has made it possible to break the limitations of the existing visual detectors.

We have developed a new type of visual detector, SCIFI-target, which has worked as a triggerable active target, utilizing plastic scintillating fibers and image intensifier tubes [40]. The present experiment (KEK-E224) has been planned using this detector to obtain pure $(K^-, K^+)$ reactions with higher statistics than the previous experiments and to search for the $H$ both via the direct process shown in Eq. 3 and via the $\Xi^-$ absorption process as shown in Eq. 4 by observing its decay products such as $H \rightarrow \Sigma^- p$.

The structure of the SCIFI-target is schematically shown in Fig. 1. The SCIFI-target consists of a bundle of plastic scintillating fiber of 500 $\mu$m$\times$500 $\mu$m. The effective volume is 8 cm$\times$8 cm$\times$10 cm in dimension. The size has been optimized for the detection of the typical hyperon decay. Thus the experiment is sensitive to the $H$ of which lifetime is in the order of $10^{-10}$ sec. The SCIFI-target has contained carbon and hydrogen atoms equally. Charged tracks have been observed around the interaction points three-dimensionally in the SCIFI-target. The target has been viewed orthogonally by two sets of image intensifier tubes (IIT) with large aperture (8 cm$\phi$). The IIT's are gated by external triggers.

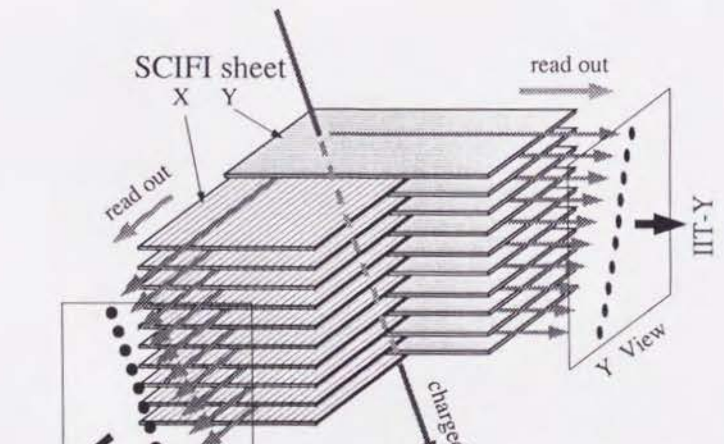


Figure 1: The schematic structure of the SCIFI-target providing three-dimensional track information.

This detector has several advantages; (i) The SCIFI-target provides visual images of $(K^-, K^+)$ reactions, the following secondary interactions and the decay products.

(ii) Owing to the capability of the plastic scintillating-fiber for high rate, the obtainable event rate of $(K^-, K^+)$ reactions is much higher than those in the experiments with other existing visual detectors (emulsion, bubble chamber etc). (iii) The readout device, IIT, can be easily gated with external trigger signals. Because of the gating operation most of the tracks due to background reactions have been eliminated in the picture. Therefore, it is easy to identify a neutral particle from its decay mode. These unique advantages of the SCIFI-target provide us a new method for studying of the $H$ dibaryon, and open a new field of hyperon physics at intermediate energy region.

In this paper we focus on the study of the direct $H$ production in the mass range from 2200 to 2230 MeV/$c^2$ by means of the observation of the decay products in the SCIFI-target. Since the direct $H$ production is a quasi-free reaction, a possible signal of $H$ production can be identified as a peak in the $K^+$ momentum spectra in the reaction shown in Eq. 3. For heavier $H$ mass of interest, however, the peak corresponding to the $H$ production is hardly separated from a large tail of the quasi-free $\Xi^-$ production process in the $K^+$ momentum spectrum. Therefore, the existence of the $H$ could be examined by means of the observation of its decay products in the pictures obtained with the SCIFI-target. The $H$ has been identified as the weak decay sequence;

$$H \rightarrow \Sigma^- + p, \quad \text{then} \quad \Sigma^- \rightarrow \pi^- + n. \tag{5}$$

The present experiment was performed at the K2 beam line in KEK 12-GeV Proton Synchrotron. The SCIFI-target was exposed to 1.66-GeV/$c$ $K^-$ beam with the intensity of $2\times10^4$/spill. The momenta and velocities of the incident and scattered particles were analyzed with high resolution spectrometers both upstream and downstream of the target. Using information from the spectrometers, the double strangeness transfer at the first vertex were confirmed. Thus only the data on $(K^-, K^+)$ reactions in the SCIFI-target have been analyzed. About 8,000 pictures of $(K^-, K^+)$ reaction have been collected and analyzed to search for the $H$.

The experimental setup is presented in Section 2. In Section 3 we describe the SCIFI-target in detail, including the data handling method and the basic performance of the SCIFI-target. We describe the procedure for the analysis of the direct $H$ production search in Section 4. The results and discussions are given in Section 5.

The conclusion is given in Section 6.

# 2 Experimental setup

## 2.1 KEK K2 beam line

The experiment was performed at the K2 beam line in KEK 12-GeV Proton Synchrotron (PS). The specification of the K2 beam line is listed in Table 1. Primary protons were extracted from the PS during 2 seconds after every 2 seconds of acceleration cycle, and transported to the primary target point of the K2 beam line. A schematic view of the K2 beam line is shown in Fig. 2. The K2 beam line was

| | |
|---|---|
| beam length | 28.9 m |
| primary target | platinum (6 mm×3 mm×60 mm) |
| production angle | 0 degree |
| momentum range | 1–2.1 GeV/$c$ |
| angular acceptance | ±50 mrad.(H)×±6.5 mrad.(V) |
| beam size (r.m.s.) | 7.8 mm(H)×5.8 mm(V) |
| momentum byte | 3.6% |

Table 1: The specification of the K2 beam line.

designed to produce an enriched kaon beam with the momentum of 1 GeV/$c$ to 2 GeV/$c$. The production target is made of a platinum rod with the size of 6 mm wide, 3 mm thick and 60 mm long. The secondary particles of $K^-$, $\pi^-$ and $\overline{p}$ produced in the direction of 0 degree were bent with the dipole magnet D1 by 23 degree. The beam was focused at the position of the momentum slit by quadrupole magnets Q1 and Q2. Then it passed trough an electro-static mass separator (SEP) of 6 m long which had electrodes with 10-cm gap providing electro-statical field of 60KV/cm vertically. The particles were splitted in respect of the mass by SEP, and then vertically focused by quadrupole magnets Q3 and Q4 at the position of the mass slit with a gap of 1mm which discriminated $K^-$'s from $\pi^-$'s and $\overline{p}$'s. The vertical position of the $K^-$ was adjusted by the correction magnet (CM) in order to get the highest yield of $K^-$'s. Finally, the beam was bent and focused on the SCIFI-target by the dipole magnet D2 and the quadrupole magnets Q6 and Q7.

We used the $K^-$ of 1.66 GeV/$c$, since it gave maximum yields for the $(K^-, K^+)$ reaction. Typical intensity of $K^-$ was $2\times10^4$/spill with the primary proton of $2.1\times10^{12}$/spill.

Typical $K^-/\pi^-$ ratio was 1/4. The beam size on the target center was 7.8 mm (r.m.s) in horizontal and 5.8 mm (r.m.s.) in vertical. The momentum byte was 3.6% (FWHM), and the width of incident angle was 104 mrad. (r.m.s) in vertical and 27 mrad. (r.m.s) in horizontal.

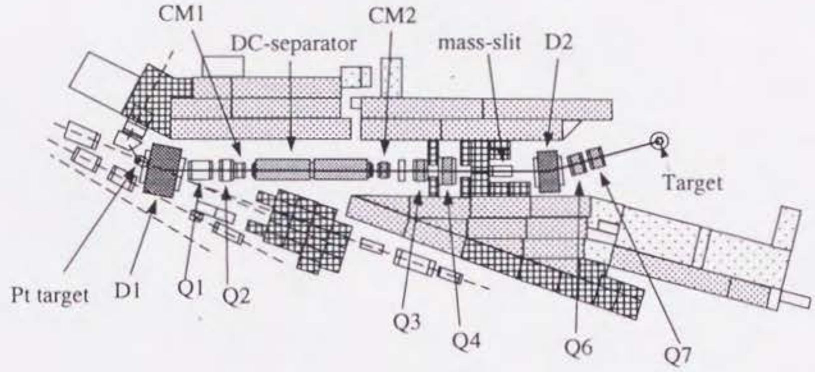


Figure 2: The top view of the K2 beam line.

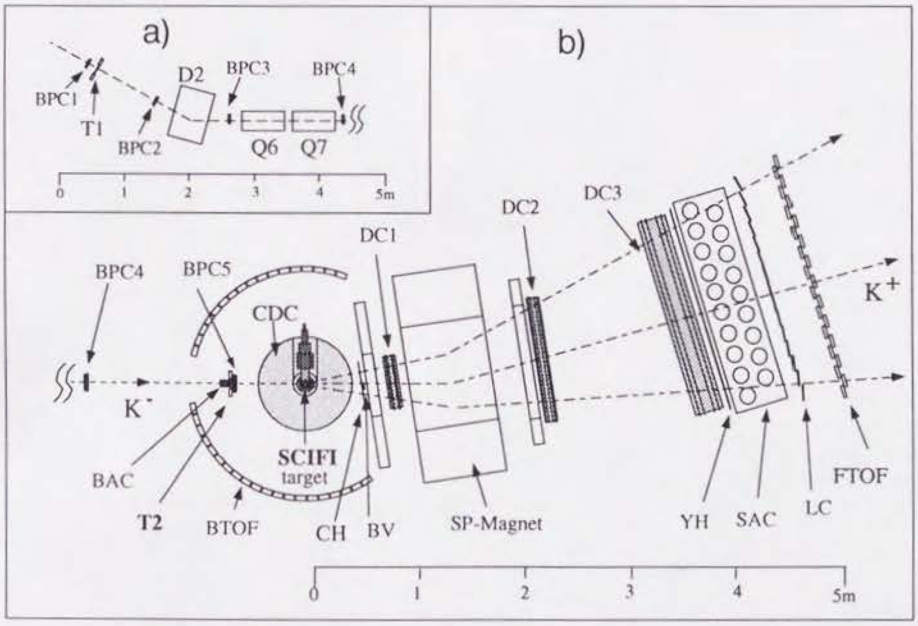


Figure 3: The top view of the experimental setup. a) The beam spectrometer. b) The $K^+$-spectrometer. See the text about the description of each component.

## 2.2 Beam spectrometer

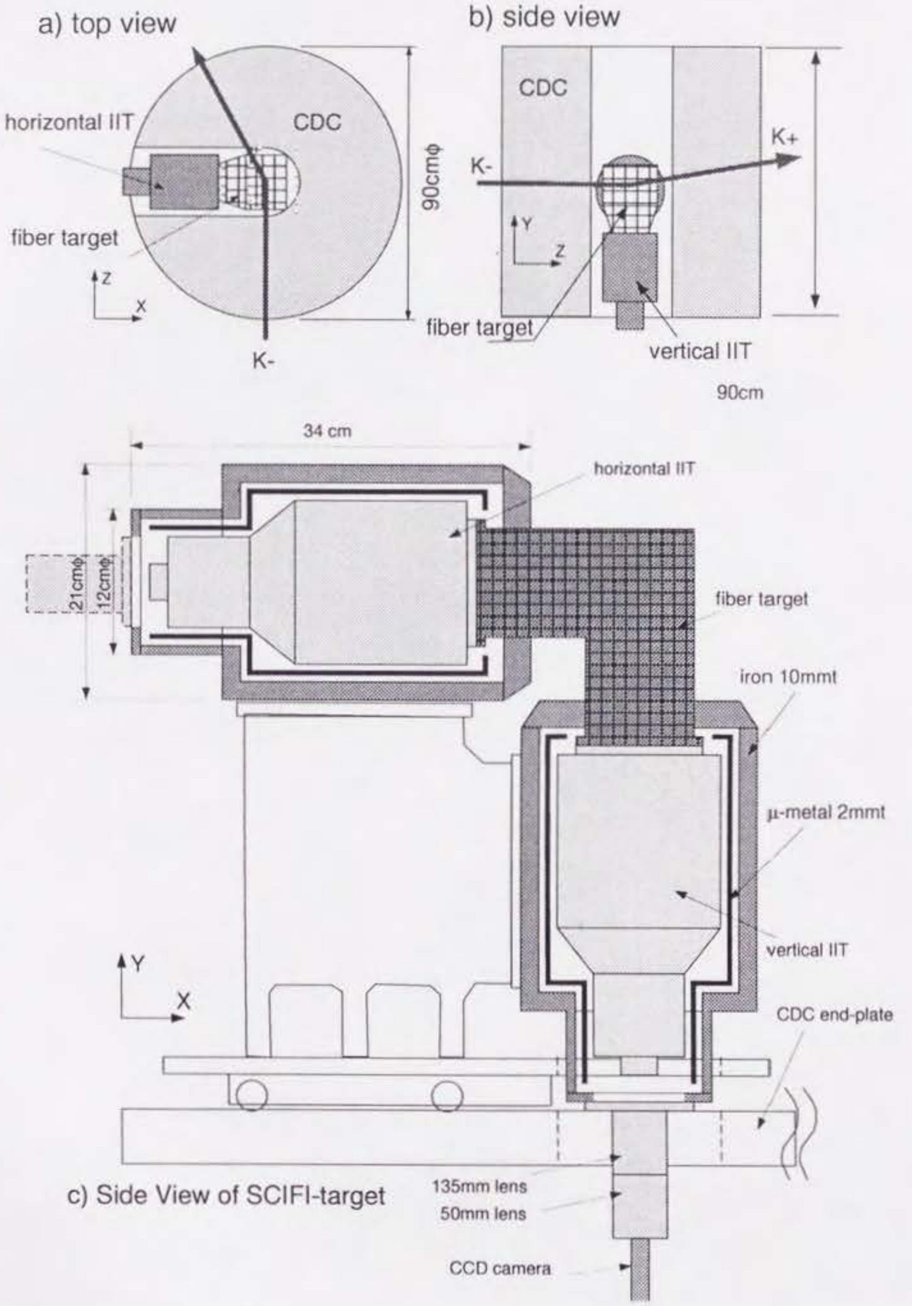


Figure 4: A schematic view of the setup of CDC and the SCIFI-target; a) the top view and b) the side view. The SCIFI-target was installed inside of CDC. The side view of the SCIFI-target is shown in c). The target was viewed by two IIT's which were cased in the magnetic shields. Each end of the IIT was read out by the CCD camera through the lens system.

The identification and the tracking of the incident particles were performed with two scintillation counters (T1, T2), a silica aerogel Čerenkov counter (BAC) and 5 sets of multi-wire proportional chambers (BPC1–5). These counters were placed upstream of the SCIFI-target as shown in Fig. 3 together with other experimental apparatus.

The T1 and T2 are made of plastic scintillators (NE pilot-U) of 5 mm thick, 5 cm high, and 10cm and 5 cm wide, respectively. Each of them was viewed by two sets of photo-tubes (HAMAMATSU R2083) from both ends. The T1 and T2 were located 6 m apart from each other. The signal from them were used to get the time-of-flight information of the incident particles with the resolution of 85 psec (r.m.s).

Blocks of slica aerogel (BAC) were used to eliminate $\pi^-$, $\mu^-$ and $e^-$ in the incident beam. They had a refractive index of 1.041 which corresponded to the $\beta$ threshold of 0.961 for the Čerenkov radiation. The blocks had sizes of 8 cm wide, 8 cm high and 3 cm thick and were viewed by a photo-tube (HAMAMATSU R1250). It was sensitive to the Čerenkov light from the incident $\pi^-$ of 1.66 GeV/$c$ ($\beta$=0.997) but was not sensitive to the incident $K^-$ with the same momentum ($\beta$=0.959). The rejection efficiency for the $\pi^-$ was more than 99%.

The BPC's were MWPC's having anode wires with 1 mm spacing and carbon-coated cathode planes. The "magic gas", mixture of Ar, freon($CF_3Br$), $C_4H_{10}$ and methylal with mixing ratio of 73:24:0.5:3 was used for BPC's. The incident particles were tracked with BPC1, BPC2 and BPC3 located upstream of D2, and BPC4 and BPC5 located downstream. The tracks obtained with BPC's were used to determine the momenta of the incident particles and gave the positions in the SCIFI-target.

## 2.3 $K^+$-spectrometer

### 2.3.1 Spectrometer magnet

The spectrometer magnet "KURAMA" was a window-frame-type dipole magnet which analyzed the momenta of scattered particles. The pole piece was 80 cm long, 50 cm high and 100 cm wide. The end-guard plates of 8 cm thick were equipped both upstream and downstream of the magnet. The aperture of the downstream end-guard was 100 cm wide and 60 cm high, whereas the upstream one was 50 cm wide and

30 cm high. The aperture of the upstream one was smaller than downstream one in order to reduce the effect of the fringing magnetic field on the IIT's. The magnet center was located 130 cm downstream of the target. The direction of the magnet was rotated by 0.15 rad. with respect to the beam direction. The maximum field strength was 1.1 T and $B \cdot dl$ was 1.08 T·m for particles with momentum of 0.8~1.3 GeV/$c$.

### 2.3.2 Drift chambers

The drift chambers DC1, DC2 and DC3 were located downstream of the SCIFI-target to track the scattered particles. These chambers and cylindrical drift chamber (CDC) were used for the tracking of scattered particles.

The DC1 consisted of two X planes, Y and U planes, where the wires of U plane was tilted by 15 degrees from vertical to solve the stereo ambiguity. The spacing of sense wire was 10 mm, and the drift distance was 5 mm. The cathode planes were made of aluminum coated foils. The effective area was 50 cm wide and 35 cm high. It was located at the entrance of the spectrometer magnet. The typical efficiency was 99.5%. The position resolution was 220 $\mu$m for the X planes and 400 $\mu$m for the Y planes.

The DC2 which consisted of two X planes and two Y planes was located just downstream of the spectrometer magnet. The effective area was 120 cm×120 cm. The anode wires were surrounded by hexagonally located potential wires. The spacing between adjacent anode wires was 9 mm. The typical efficiency was 90.3%. The position resolutions were 230 $\mu$m for the X planes and 270 $\mu$m for the Y planes, respectively.

The DC3 consisted of two X planes and two of Y planes. It was located 120 cm downstream of the DC2 having an effective area of 180 cm wide and 90 cm high. The distance between the sense wire and the potential wire was 28 mm for X planes and 30 mm for Y planes. The distance between the sense wire and the cathode plane was 7 mm for X planes and 6 mm for Y planes. The typical efficiency was 93.5%. The position resolutions were 310 $\mu$m for X planes and 390 $\mu$m for Y planes, respectively.

Mixed gas of Ar-ethane (1:1) was used for all the drift chambers. The potential wires of DC1 and DC3 were made of gold-plated Cu-Be of 75 $\mu m\phi$ and of 150 $\mu m\phi$, respectively. These of DC2 were made of aluminum of 200 $\mu m\phi$. The anode wires of all the chambers were made of gold-plated tungsten of 20 $\mu m\phi$.

### 2.3.3 Aerogel Čerenkov counter for spectrometer

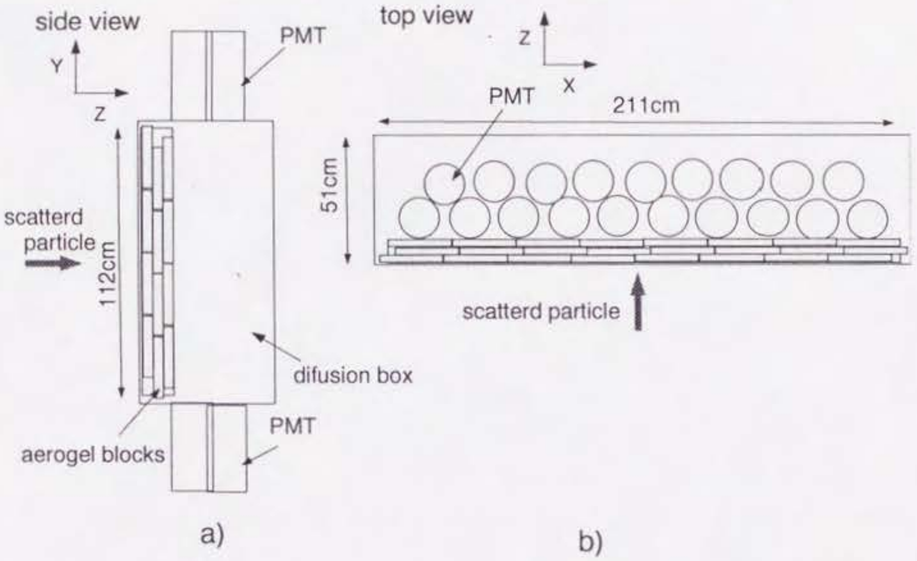


Figure 5: The schematic view of the SAC, a) the side view and b) the top view.

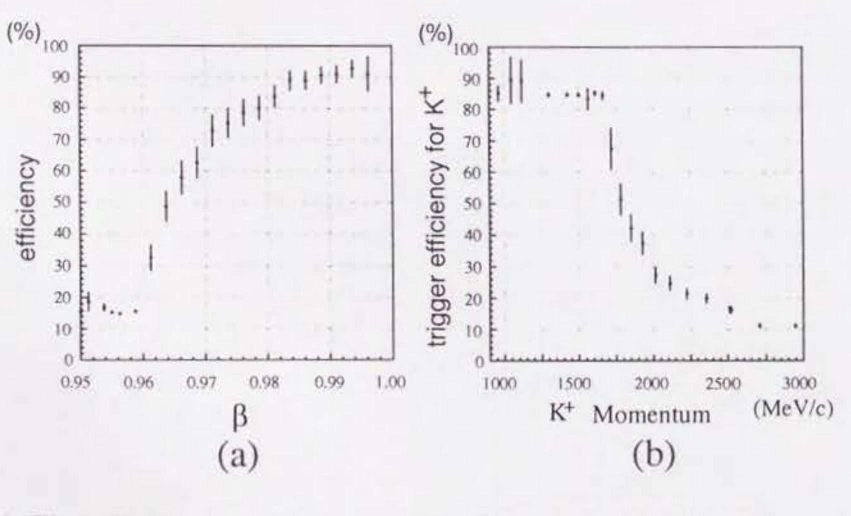


Figure 6: a) The efficiency of SAC as a function of $\beta$. b) The trigger efficiency of SAC for $K^{+}$'s as a function of the momentum.

The silica aerogel Čerenkov counter (SAC) with sensitive area of 200 cm wide and

100 cm high was located downstream of the DC3. It eliminated the contamination of $\pi^+$'s in the scattered particles. The refractive index of the silica aerogel was 1.041 which corresponded to the $\beta$ threshold value of 0.961. The schematic view of SAC is shown in Fig. 5. The silica aerogel blocks of 25 cm×25 cm×3 cm were stacked in three layers along the beam direction. The positions of blocks were staggered with 1.5 cm in X and Y directions in order to prevent possible inefficiency due to "punch-through" of $\pi^+$'s. The blocks were installed in a diffusion box of which walls were covered with white paper (Milipore). The box was viewed by 38 photo-tubes (HAMAMATSU R1250 and RCA 8854) from the top and bottom. The averaged number of photo-electrons was about 3 for the minimum ionizing particle. The trigger efficiency for $K^+$ of 1.6 GeV/$c$ was 85%, and the efficiency for $\pi^+$ with a momentum above 1 GeV/$c$ was 90% as shown in Fig.6.

### 2.3.4 Forward TOF hodoscope

The forward TOF hodoscope was used for the "time-of-flight" measurement to obtain the velocity of the scattered particles. The "time-of-flight" (TOF) of scattered particles were measured between the T2 counter and the forward TOF hodoscope (FTOF). The FTOF consisted of 24 scintillators of 12 cm wide and 3 cm thick. The height was 130 cm for central 10 counters and 110 cm for the others. The both ends were viewed by photo-tubes (HAMAMATSU H1949). The FTOF was located 5 m downstream of the SCIFI-target. The typical resolution was 110 psec (r.m.s). Each counter of FTOF provided the vertical hit position by means of the time difference between the signal from two photo-tubes of both ends. The spatial resolution of 14.8 mm (r.m.s) was obtained.

### 2.3.5 Trigger hodoscopes

The hodoscope CH which consisted of 12 scintillators of 3.5 cm wide, 17 cm high and 1 mm thick was located just upstream of the spectrometer magnet. It was used to provide the scattering angles of particles for the first-level trigger as well as the second-level trigger.

The Y-hodoscope (YH) was a vertical one which consisted of 6 plastic scintillators of 196 cm wide, 16 cm high and 4 mm thick. They were viewed by photo-tubes from both ends. It was placed just upstream of SAC in order to identify the charged particles coming into SAC. The YH defined the geometrical acceptance of the spectrometer which was 0.09 str. for the particle with the momentum of 1.1 GeV/$c$.

The non-interacting beam veto counter (BV) was a plastic scintillation counter placed just upstream the spectrometer magnet. It was used to veto non-interacting $K^-$'s. This counter covered the angular accesptance of $\theta \leq 0.063$ rad. to the beam trajectory.

## 2.4 Target area

### 2.4.1 SCIFI-target

The SCIFI-target was the central detector which worked as a target for $(K^-, K^+)$ reactions as well as a tracker for all the tracks of charged particles around the $(K^-, K^+)$ reaction vertexes. The SCIFI-target consisted of a bundle of plastic scintillating fibers of 500 $\mu$m×500 $\mu$m (8 cm×8 cm×10 cm in dimension). The target was viewed orthogonally by two sets of image intensifier tubes (IIT). The IIT's were gated by the first-level trigger and later by the signal of second-level trigger in order to select the pictures of interest. The output of IIT's were viewed by CCD video cameras. The SCIFI-target was installed at the center of CDC as shown in Fig. 4. The detailed description and the performance are described in Section 3.

### 2.4.2 Cylindrical drift chamber

The cylindrical drift chambers (CDC), which surrounded the SCIFI-target, was used to detect reaction products escaped from the SCIFI-target as well as the incident $K^-$'s and the outgoing $K^+$'s. The inner radius of the CDC was 16 cm, and the outer radius was 38.4 cm. The height of CDC was 90 cm. The CDC consisted of 6 vertical layers and 2 stereo layers with wires tilted by 5.71° to the vertical direction. The chamber had an identical cell structure of wires. The anode wires were made of gold-plated tungsten of 20 $\mu$mm$\phi$. The potential and field-shaping wires were made of gold-plated Cu-Be of 100 $\mu$m$\phi$. Mixed gas of Ar-ethane (1:1) was used for CDC.

The typical efficiency was 93% to 96%. The position resolution was 270 $\mu$m.

## 2.5 Trigger logic

The trigger logic of the present experiment was utilized to select the images of the IIT's. The IIT's consisted of three stages. The first stage kept the images during the decay time of phosphor, 2.4 $\mu$sec. The first-level trigger which was made up with the signals from the scintillation counters and the Čerenkov counters which identified a $(K^-, K^+)$ reaction in the SCIFI-target. It was applied to open the gate of the second stages of the IIT within 300 nsec after the incident particle was put in the target.

The maximum acceptable trigger rate for the image data acquisition system was less than 10 Hz due to the long read-out time of the CCD. To reduce the trigger rate the second-level "mass trigger" was made by using "time-of-flight" information of scattered particles. It determined the mass of scattered particle and eliminated $(K^-, p)$ reactions which was the major contamination in the events in the first level trigger. The second level trigger was applied to the third stage of the IIT's as well as the start signal for the image data acquisition system. The decision time of the second-level trigger was 14 $\mu$sec, while the decay time of phosphor of the second stage was about 50 $\mu$sec. The detail of the trigger logics can be seen in Ref. [42]. We briefly describe the logic, here.

The coincidence signal of the two beam counters T1 and T2 with the veto-signal from BAC was used to define the incident $K^-$. The $K^-$ which didn't interact in the target was rejected with the veto signal from the BV counter. The "$K^+$" was defined as the coincidence signal of CH and FTOF with the veto signal from SAC which identified $\pi^+$'s. The outgoing particles with positive charge were selected by the matrix-coincidence-logic (charge trigger) which identified the charge with the bending angle deduced from the combination of the hit positions of CH and FTOF. In addition, a signal from YH was required in order to reject neutral particles.

The events selected by the first-level trigger contained protons produced via $(K^-, p)$ reactions as the major backgrounds. The $K^+$'s were selected as the produced particles in the second-level trigger process using information of the mass which was obtained by the time-of-flight between FTOF and T2 as well as hit positions at CH and FTOF.

The hit positions of CH and FTOF were encoded and stored in the FI/FO memory (Lecroy Data-Stack). The momentum information was deduced from the bending angle given by the combination of the hits of CH and FTOF. The possible momenta were obtained from the pre-loaded table in the Memory-Lookup-Unit (Lecroy MLU) for each combination of the hits of CH and FTOF. The time-of-flight of FTOF were digitized with the fast encoding TDC system (Lecroy FERA). The time-of-flight was examined for every momentum by checking with another pre-loaded table in MLU. If the data was in the region which corresponded to $K^+$'s, the second-level trigger was fired. The trigger rate of protons were reduced by factor of 10 by means of this procedure. The efficiency was greater than 90% for the $K^+$ with the momentum larger than 700 MeV/$c$. A typical trigger rate was 55 Hz for the first-level trigger and 10 Hz for the second level trigger with the $K^-$'s of $1\times10^4$/sec.

## 2.6 Data acquisition

The schematic diagram of the data acquisition system (DAQ) is shown in Fig. 2.6. We built the DAQ systems for the data from the SCIFI-target and for these from the spectrometer independently.

The first-level trigger was applied to the second stages of the IIT's, and it initiated the DAQ sequence for the counters in the spectrometers. The digitization was performed by standard CAMAC modules and KEK-standard TKO modules. The data from the counters were stored in the CAMAC memory modules during the beam burst, and then they were written in magnetic tapes (Exabyte) by a $\mu$-VAX computer at the end of the burst.

The second-level trigger was applied to the third stage of the IIT's, and it initiated the DAQ sequence of the SCIFI-data. The images viewed by the CCD cameras were digitized with image digitizer modules and stored in the FI/FO modules. The video signals were recorded in standard video-tape recorders simultaneously. The data were read out continuously by standard parallel I/O registers of respective VME computers and were written in magnetic tapes (Exabyte) separately. The read-out sequence of the VME computers was continuous and irrespective to the trigger timing. A typical dead-time was 30 ms which was mainly due to the duration of 1 video frame. The correspondence between the spectrometer data and the SCIFI-data was made by the sequential event number. The numbers were fed into the image digitizer as well as the parallel I/O register of CAMAC and VME's to tag the event. The details of the image digitizer modules are described in Section 3.

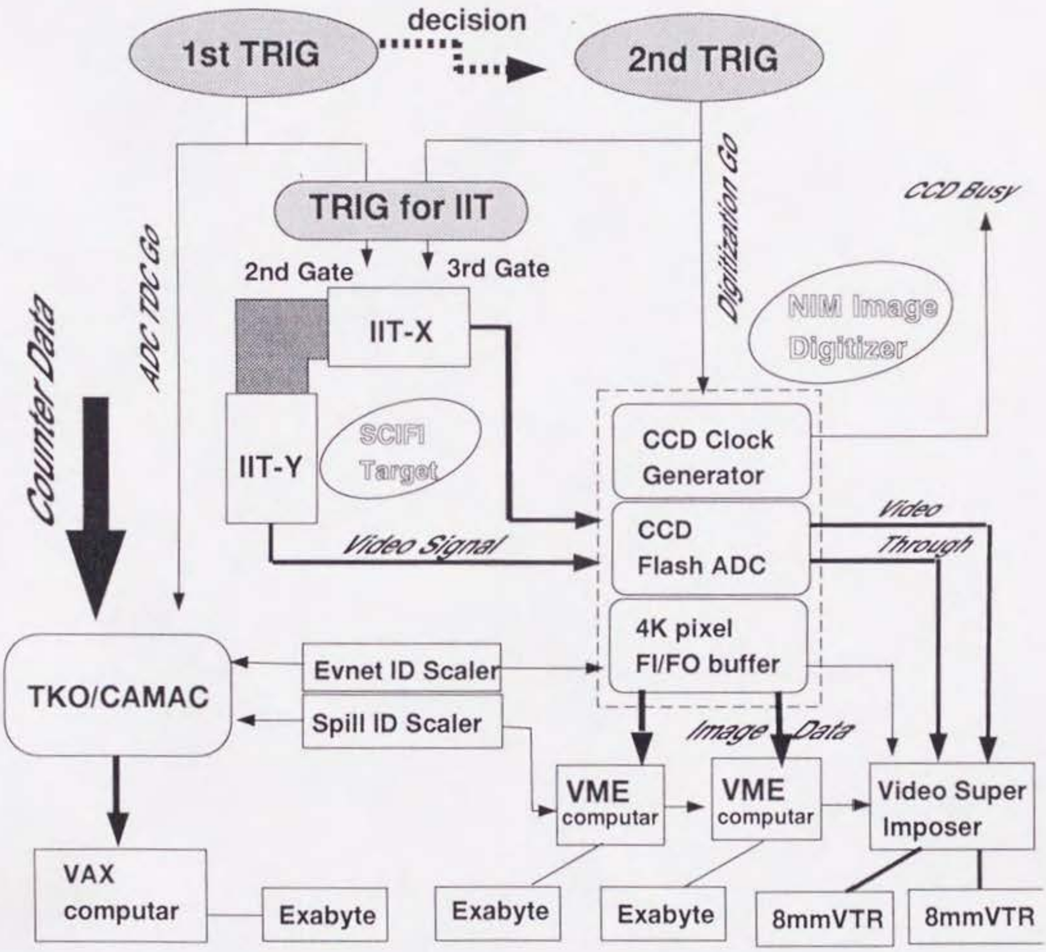


Figure 7: The schematic diagram of the data taking system.

# 3 The SCIFI-target system and the method of data analysis

## 3.1 Structure of SCIFI-target

### 3.1.1 Scintillating fiber block

The SCIFI-target consisted of about 30,000 plastic scintillating fibers of 20cm long. The scintillating fiber (KURARY SF-81) had a square cross section with the dimension of 500 $\mu$m$\times$500 $\mu$m. The core size was 480 $\mu$m square, and the clad thickness was 10 $\mu$m. The core material was made from polystyrene of which refractive index was 1.59 and density was 1.06 g/cm$^3$. The cladding material was made from polymethylmethacrylate (PMMA) of which refractive index was 1.49 and density was 1.18 g/cm$^3$. The spectrum of the transmitted light had a peak at 437 nm.

The schematic view of the scintillating fiber block is shown in Fig. 8. Sheets which consisted of 160 fibers were stacked alternately in the X (horizontal) and the Y (vertical) directions to provide three-dimensional views of the tracks of particle as shown in Fig. 1. The number of stacked fiber-sheets was 92 for each direction. The sheets were bonded with black acrylic glue of 50 $\mu$m thick, which also worked as extra mural absorber (EMA) in order to eliminate cross-talks of photons over the sheets. Overall effective areas were 8 cm$\times$10 cm in both X-Z and Y-Z planes. The sizes of the images were reduced to 8 cm$\times$7.8 cm on the readout surfaces where the sheets were stacked with spacers of 350 $\mu$m in thickness alternately. The stack of sheets was mounted in an acrylic case of 1 cm thick. The other ends of fibers were equipped with LED light sources through holes on aluminum plates for providing the position references.

### 3.1.2 Image intensifier tube

The SCIFI-target was viewed by two sets of the image intensifier tube (IIT), which amplified the photon images of tracks and were gated with external triggers in order to select events of interest. The IIT's (Delft PP0040) were assemblies of 3 stages of image intensifiers. The schematic view of the IIT is shown in Fig. 9.

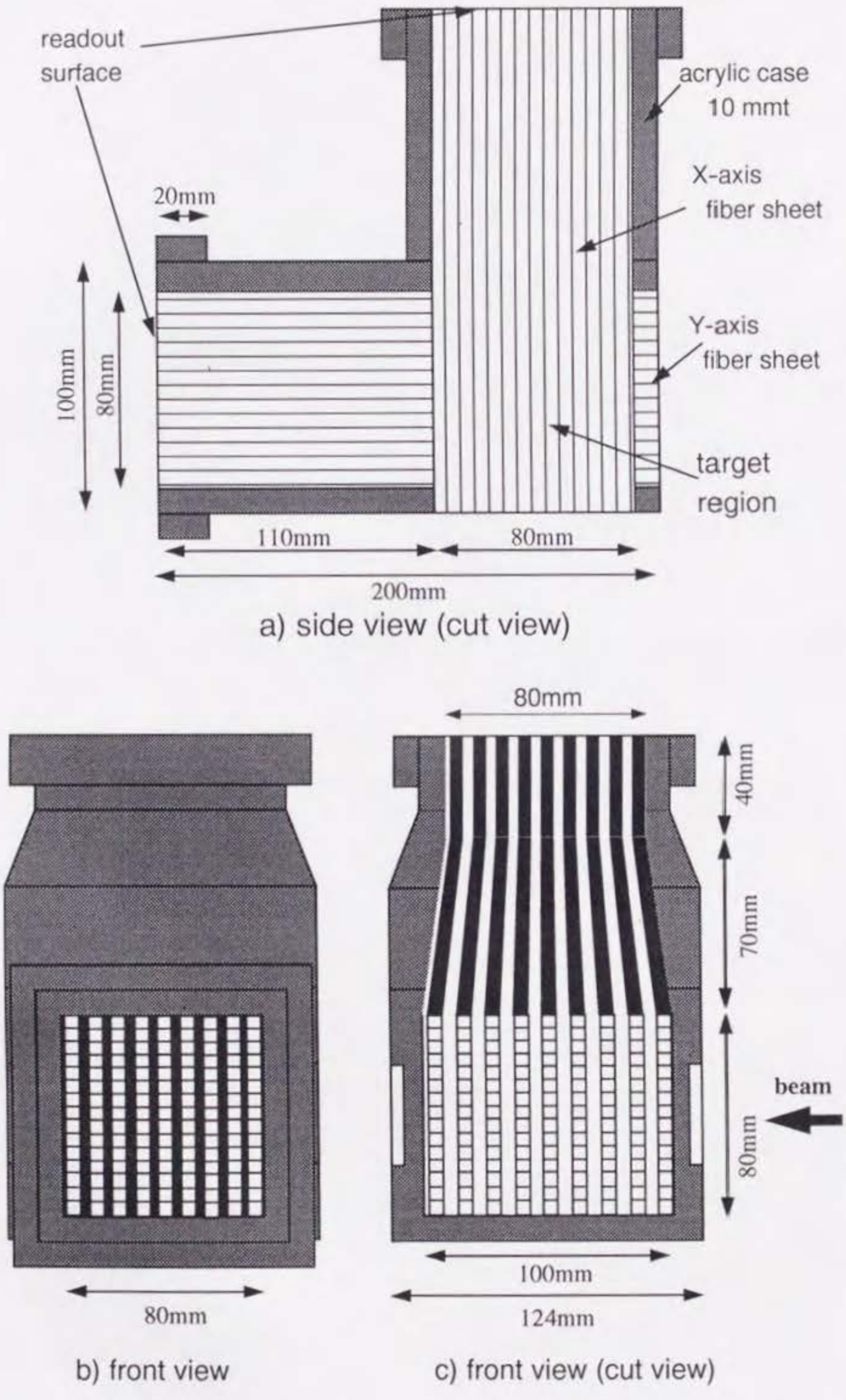


Figure 8: The schematic view of the scintillating fiber target.

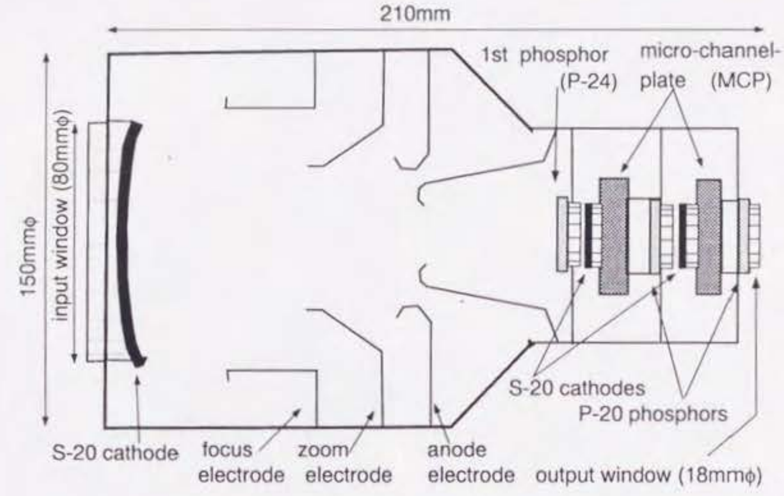


Figure 9: The schematic view of the image intensifier tubes.

The first stage was of an electrostatic type operated with DC voltage of 20 KV. The diameter of the input window was 80 mm$\phi$, and that of the output window was 18 mm$\phi$. Both input and output windows were made of glass fibers with diameter of 10 $\mu$m. The photo-cathode of the input window was equipped with S20. The photons from the scintillating fiber were converted to photo-electrons, and the image was demagnified by factor 5 with an electrostatic lens. Photons were produced by means of the bombardment of photo-electrons on P24 phosphor, of which decay time was 2.4 $\mu$sec, at the front of the output window made of optical fiber. Average production rate of photon per electron was 8 in the case that the voltage applied between the cathode and the anode was 20 KV.

In the second stage a micro-channel-plate (MCP) was used to multiply photo-electrons. Owing to the MCP, it had high photon gain with rather low voltage ($10^3$ at 750 V) and was easily triggered by changing the applied voltage between the cathode and the MCP. The MCP was gated by the first-level trigger as described later. The input and output windows of the diameters of 18 mm. The photo-cathode was made of S20. The output window was equipped with P20 phosphor of which decay time was approximately 50 $\mu$sec. The third stage was the same device as the second stage, whereas the MCP was gated with the second level trigger.

### 3.1.3 Operation of IIT and the gating system

Since photon emission from the phosphor continued during the decay time of phosphorescence, the time resolution of the IIT was determined by the decay time, and the phosphor played a role of "optical delay" of the image. It enabled us to select images of interest using trigger pulses from the counter system as shown in Fig. 10-a). Considering the beam intensity ($10^5$/sec) of the present experiment, we used the IIT's of electro-static type with the phosphor whose decay time was 2.4 $\mu$sec in order to prevent the exposure for more than two events in one picture. The decision time of the first-level trigger was 300 ns, thus the image had to be kept for the period. The first-level trigger was used to open the gate of the second stage, which kept the image for the phosphor decay time of 50 $\mu$sec. The second-level trigger was applied to the third stage, of which output was detected with a CCD camera.

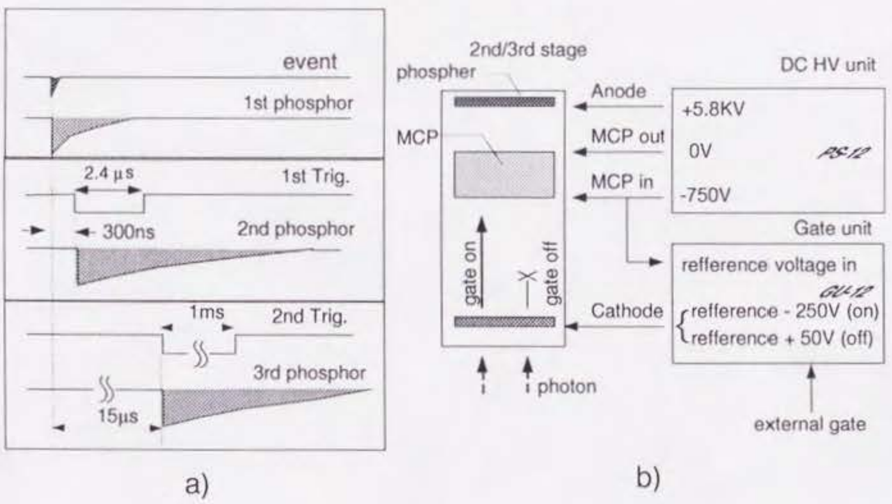


Figure 10: a) Schematic timing chart of gate signals and decay times of the phosphors of the IIT. b) The gate operation of the second and third stage.

The DC voltages 20 KV, 5 KV and 1 KV were applied to the anode, zoom and focus electrode of the first stage, respectively. The cathode electrode was grounded. The focusing property and magnification of the image were adjusted by changing the voltages on the focus and the zoom electrodes. The MCP's of the second and the third stages were operated with the applied voltage of 750 V. The voltages applied between the cathode and the MCP were -200 V to open the gate and +50 V to close it with respect to the MCP voltage as shown in Fig. 10-b). The rise time of the gate pulse was about 100 ns.

### 3.1.4 Magnetic shields

The fringing field of the spectrometer magnet affected the trajectories of photo-electrons in the IIT. This effect was considerably large for the electro-static focusing on the first stage, and caused distortion of the image. The IIT's were put in the magnetic shield to eliminate the effect (see Fig. 4). The shield consisted of two layers. The outer case was made of iron (SS-41) of 25 mm thick, and the inner case was made of $\mu$-metal (TMC-V) of 2 mm thick. The direction of the magnetic field at the target position was almost downward, and the strength was roughly 30 gauss. The magnetic field perpendicular to the tube direction was almost negligible at the cathode position of the first stage in the shield. The field along the tube direction was about 3 gauss for the vertical IIT and about 1.5 gauss for the horizontal IIT. The distortion of the images due to the magnetic field was corrected in the off-line analysis described in Appendix A.

### 3.1.5 CCD video camera

The photon images amplified with each IIT were viewed by a charge-coupled-device (CCD) camera through the optical lens systems. The lens system consisted of compound lenses of 135 mm and 50 mm coupled in tandem, where the lens of 135 mm attached reversely. The lens system demagnified the images from 16 mm to 6.6 mm for matching the image size to CCD-chip size. The CCD camera (SONY XC-77) contained a CCD-chip having 768$\times$493 pixels of 11.0 $\mu$m$\times$13.0 $\mu$m. The size of the CCD-chip was 8.8 mm$\times$6.6 mm. The pixels were serially read out, and the images were transfered to the image digitizer as video signals of the NTSC format. The read-out sequences of the two CCD cameras were synchronized with the image digitizer.

### 3.1.6 Image digitizer

The digitization of the video signals from the CCD cameras were performed with the image digitizer consisting of four NIM modules, a clock&coordinate generator module (CCG), flash ADC module (FADC) and two sets of the FI/FO memory buffer modules (FIFO). The schematic diagram of the system is shown in Fig. 11.

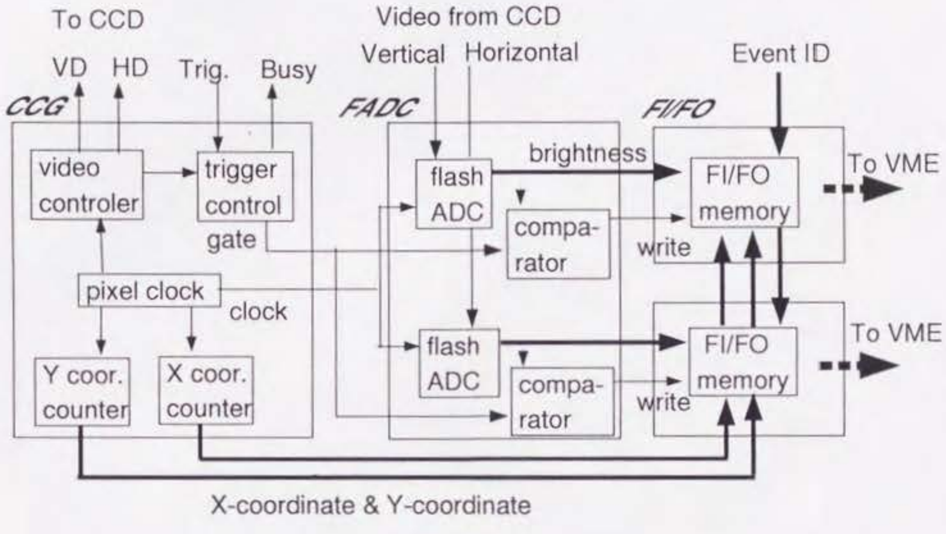


Figure 11: The schematic diagram of image digitizer modules

The CCG module provided a common clock to synchronize the whole system, and generated two-dimensional coordinates of each CCD pixel. The CCG module initiated a sequence of digitization when the second-level trigger occurred. A "CCD busy" signal was asserted during the read-out sequence in order to prohibit image overlap due to another track. The timing chart of the signal is shown in Fig. 12. The signals from CCG module controlled two CCD cameras and the FADC module with the same timing irrespective to the event timing. When a trigger occurred at the timing of "T" shown in Fig. 12, the photon image was exposed to the photo-sensitive regions of the CCD. In the NTSC format, the video signal of one frame consists of two parts, namely, the even-field and odd-field. The charge generated by the photons was kept in the photo-sensitive region of the CCD until the timing "E1" and/or "E2" which was the transfer time of either even-field picture or odd-field picture. When the transfer was completed, all the charge moved to the register-region of the CCD, and the photo-sensitive region was released for the next exposure. Thus after the timing "E2", that was the transfer time of "the second field", the "CCD busy" was negated although the data transfer from the CCD to the digitizer continued until the next charge transfer. The dead-time due to the CCD read-out was effectively 25 msec which was 1.5 times as long as the interval of the 1-field transfer (1/60 sec).

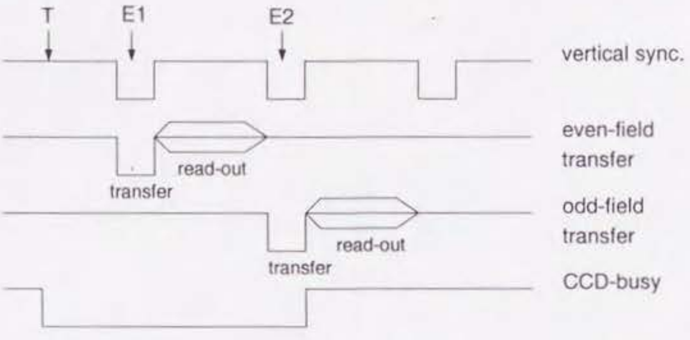


Figure 12: The timing chart of a typical image data acquisition cycle.

The two sets of flash ADC's in the FADC module digitized the pulse heights of the NTSC signals from the CCD cameras into 8-bit data of brightness for each pixel. The upper 7-bits were used, which were compared with the preset threshold value. The write-strobe signals to the FI/FO memory were generated for the pixels of which brightness was above the threshold. Then the data on the brightness, the coordinates on the CCD-chips and the serial event number of the second level trigger were stored in the memory of the FI/FO modules. The stored pixel data had the length of 32-bits which consisted of 10-bits for the X-coordinate, 9-bits for the Y-coordinates, 7-bits for the brightness and 6-bits for the serial event number. A typical number of pixels for one event was about 2,000, while the FI/FO buffer memory could storage the data of about 4,000 pixels. The data in each FIFO module were continuously read out by a standard VME I/O module, whenever the FI/FO buffer memory was not empty. During the read-out time a free space in the FI/FO buffer memory was monitored. When the free space of either FI/FO memory was less than half of the capacity, the trigger was prohibited in order to prevent overflow of the FI/FO buffer memory. Due to the effects the dead-time increased effectively by about 5 msec. Thus total dead-time was typically 30 ms.

## 3.2 Basic performance of the SCIFI-data

Figure 13-a) shows typical pictures of a $\pi^-$ of 1.6 GeV/$c$, a minimum ionizing particle (MIP) in the SCIFI-target. The left picture shows the X-Z projection obtained by the vertical IIT and the right picture shows the Y-Z projection obtained by the horizontal IIT. The gray-scale of small rectangles in Fig. 13-b) represents the brightness of the CCD pixels after pedestal subtraction. The fiducial areas defined by the size of the IIT and the CCD are shown as the areas surrounded with the lines in the pictures .

**Size and density of photon cluster:** Most of the clusters of the rectangles correspond to the image of one photon. We have applied the method of two-dimensional clustering to the CCD pixels with the weight of the brightness. The cluster spreads over 3×3 pixels typically with sigma of 180±40 $\mu$m as shown in Fig. 14-a). The distribution of the total brightness in a cluster, so-called "Harry distribution", is shown in Fig. 14-b).

The track has been identified as a sequence of clusters. The density of the cluster for a MIP track has been found to be 0.55/mm. The position of a cluster has been obtained as the center-of-gravity of the brightness of pixels, and the position resolution deduced from the residual distribution of the straight line fit on the clusters is 290 $\mu$m as shown in Fig.15. The resolution has been determined mainly by the size of scintillating fiber $\sigma_{fiber}$, the size of CCD pixel $\sigma_{CCD}$, the resolution of IIT $\sigma_{IIT}$, the accuracy of fiber-sheet alignment $\sigma_{align}$ and the distortion remained after the calibration $\sigma_{dist}$. The $\sigma_{fiber}$ has been estimated to be 500 $\mu$m/$\sqrt{12}$, and $\sigma_{CCD}$ has been about 90 $\mu$m which has been obtained from the pixel size, about ~22 $\mu$m, and the demagnification factor, about 13. The $\sigma_{IIT}$ has been found to be about 30 $\mu$m. We have estimated $\sqrt{\sigma_{align}^2 + \sigma_{dist}^2}$ to be 200 $\mu$m by a calibration as described in Appendix A. The resolution of the cluster, $\sigma_c$, has been evaluated with these values as;

$$\sigma_c \sim \sqrt{\sigma_{fiber}^2 + \sigma_{CCD}^2 + \sigma_{IIT}^2 + \sigma_{sys}^2} \sim 270\mu\text{m}, \tag{6}$$

where $\sigma_{sys}^2 \sim \sigma_{align}^2 + \sigma_{dist}^2$. The result is consistent with the measured value as shown in Fig. 15.

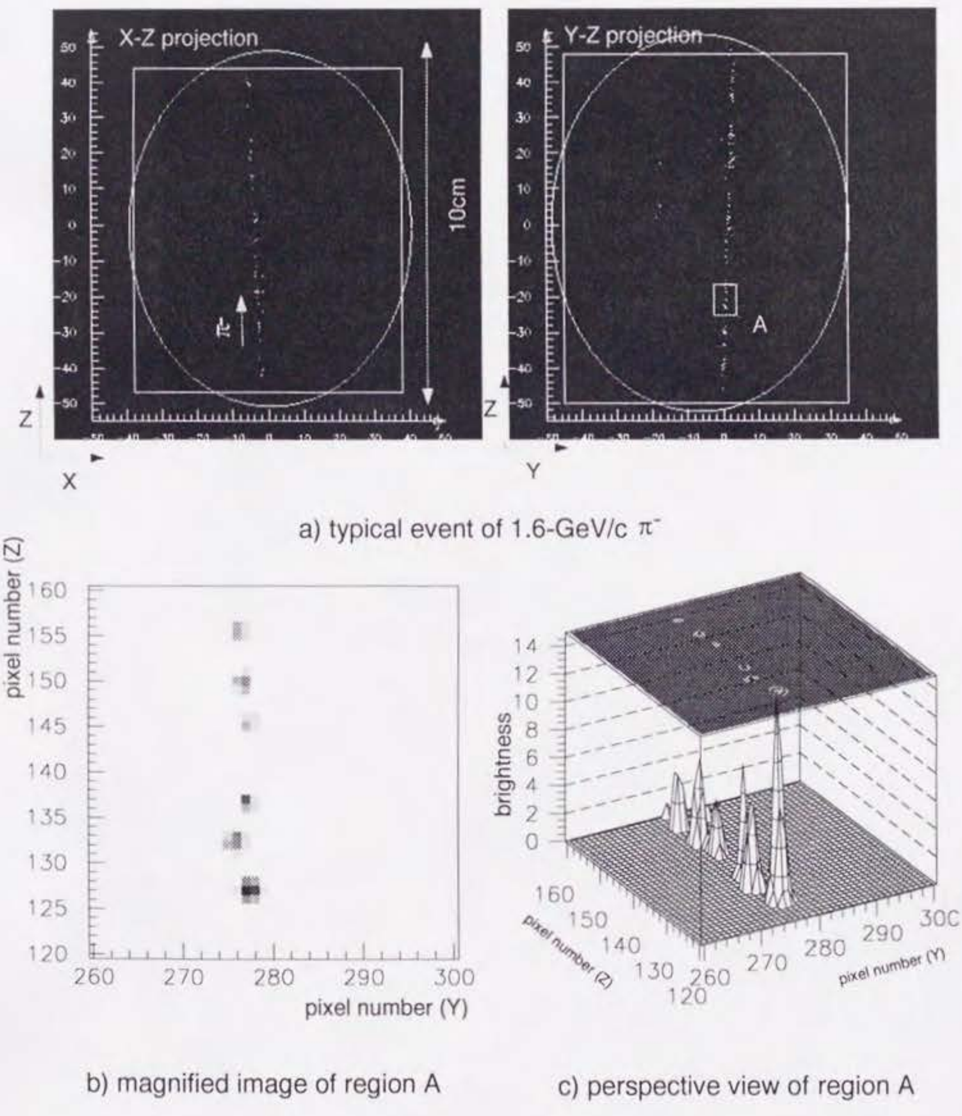


Figure 13: Typical picture of a minimum ionizing particle. A straight track of 1.6-GeV/$c$ $\pi^-$ is shown. a) Display of the track in the X-Z and Y-Z projections. b) The magnified view of the track in the region A of the Y-Z projection. Here, the axes show the pixel coordinates. Each rectangle corresponds to a pixel where the brightness is presented in gray-scale. c) The perspective view of the plot in b). The pixel brightnesses are shown as the heights.

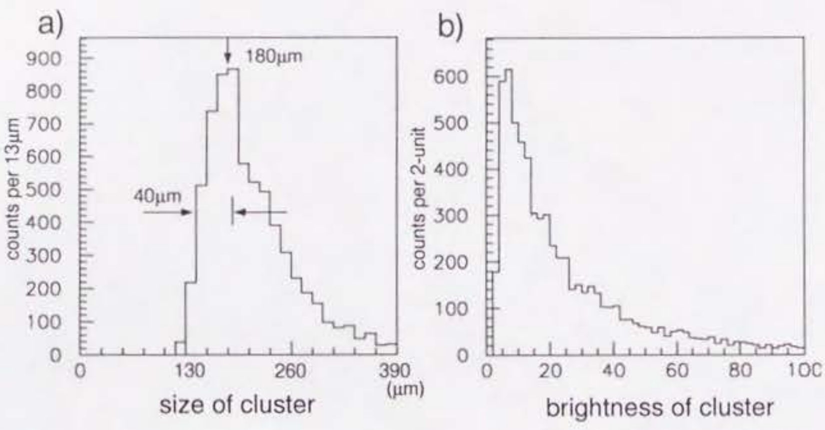


Figure 14: The properties of a cluster of one-photon obtained from the data on the tracks of MIP's. a) The distribution of the size of the cluster in r.m.s. b) The distribution of the brightness sum in a cluster.

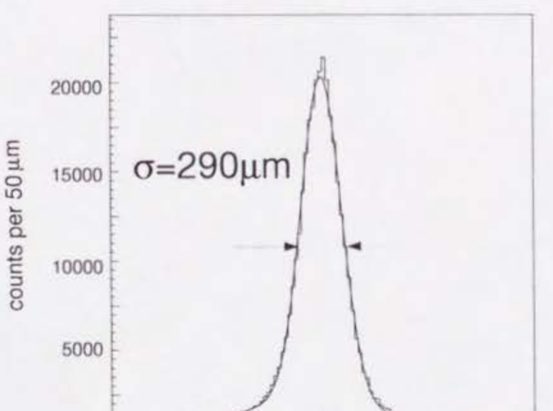


Figure 15: The residual distribution of the straight line fit on the cluster positions. A fit with two Gaussian distribution reproduces the distribution.

**Characteristics of track:** An example of image of a 500-MeV/$c$ proton which stopped in the SCIFI-target is shown in Fig. 16. In contrast to the tracks of MIP's, photon clusters stick together since the ionization of such a particle is more than four times as large as that of the track of MIP. We have observed the difference between the tracks of low energy particles and these of MIP's by means of the comparison of the brightness of the clusters along the tracks. Figure 17 shows the distribution of density of brightness along tracks of MIP's and that along typical $\Xi^-$ tracks ($\beta \sim 0.4$) produced by the $(K^-, K^+)$ reaction. The figure shows the clear difference between them.

We have carried out a straight-line fit on the data from pixels weighted by the brightness. The brightness distributions along the track directions are shown in Fig. 18, in which the widths are about 400 $\mu$m irrespective to the ionization. The brightness of $\Xi^-$ tracks is four times as large as that of the tracks of minimum ionizing $K^-$. The ratio of the ionization of the $\Xi^-$ to that of the $K^-$ agrees well with the difference of the brightness.

**Angular resolution of tracks:** In order to treat tracks of MIP's and of low-energy particles with the same algorism, we have generally use of the straight-line fit on the data from pixels as described above. The angular resolution for the tracks of MIP's has been evaluated by means of the comparison with the external tracks obtained with the $K^+$-spectrometer. The angular resolution of the external track has been less than 3 mrad. Figure 19 shows the angular resolution against the track length, which is written as $\sigma_\theta \sim 500/L$ mrad., where the $L$ is the track length in mm. The contribution of multiple scattering for the angular resolution, which is written as $0.41 \cdot \sqrt{L}$ mrad., is negligibly small for the tracks of MIP's. It is, however, considerably large for the tracks of low energy baryons. For example, the effect of multiple scattering of the 500-MeV/$c$ proton track is given as $2.9 \cdot \sqrt{L}$ mrad.

### 3.3 Analysis of the SCIFI-data

We describe the method of analysis of the SCIFI-data. First of all, we describe the scanning procedure to find a track in a picture. Then, the methods to obtain three-dimensional track information is presented. Finally we demonstrate the performance

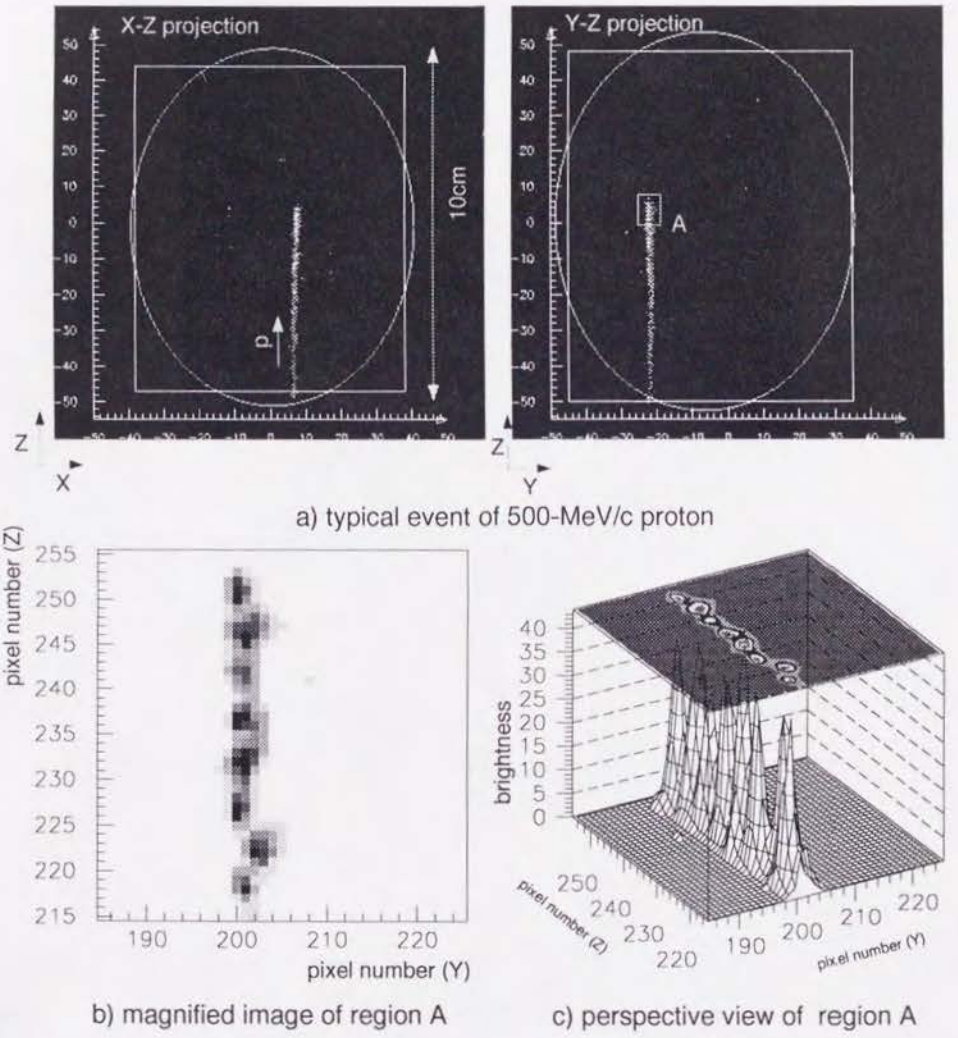


Figure 16: A typical picture of a low energy particle. A track of a 500-MeV/$c$ proton stopped in the SCIFI-target is shown. a) A display of the track. The X-Z and Y-Z projections are shown. b) The magnified view of the track in the region A on the Y-Z projection of a). Here, both axes show the pixel coordinates. Each rectangle corresponds to one pixel where the brightness is presented in gray-scale. c) The perspective view of the plots in b). The pixel brightness is shown as the height.

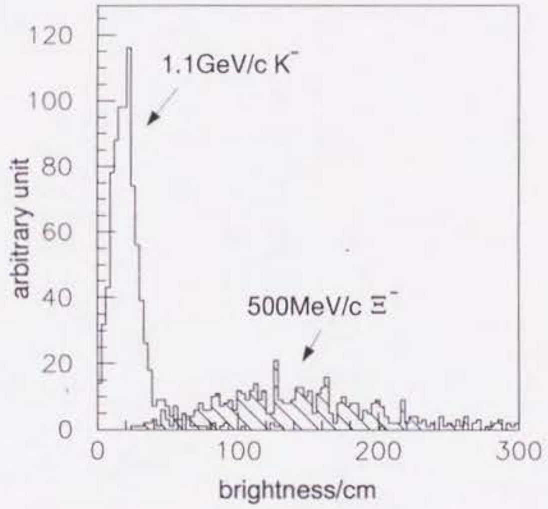


Figure 17: The distribution of brightness of the tracks of MIP's and of low energy particles. The peaks in the left side corresponds to the tracks of $K^+$'s with momenta around 1.1 GeV/$c$. The hatched broad peak corresponds to the tracks of $\Xi^-$'s whose momenta are roughly 500 MeV/$c$.

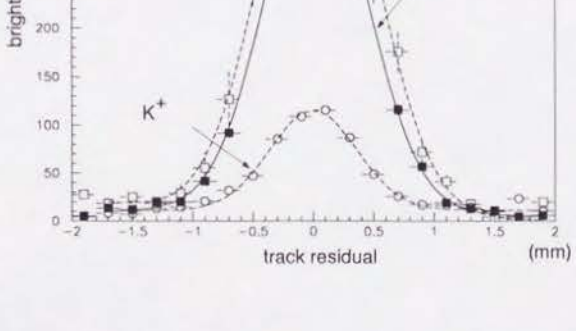


Figure 18: The brightnesses of the tracks for various particles produced by $\Xi^-$ decays. The open circles correspond to $K^+$'s around 1.1GeV/$c$ as typical MIP tracks. The black squares correspond to $\Xi^-$'s with momenta around 500 MeV/$c$. The white squares correspond to protons as typical decay products of $\Lambda$'s with momenta around 400 MeV/$c$.

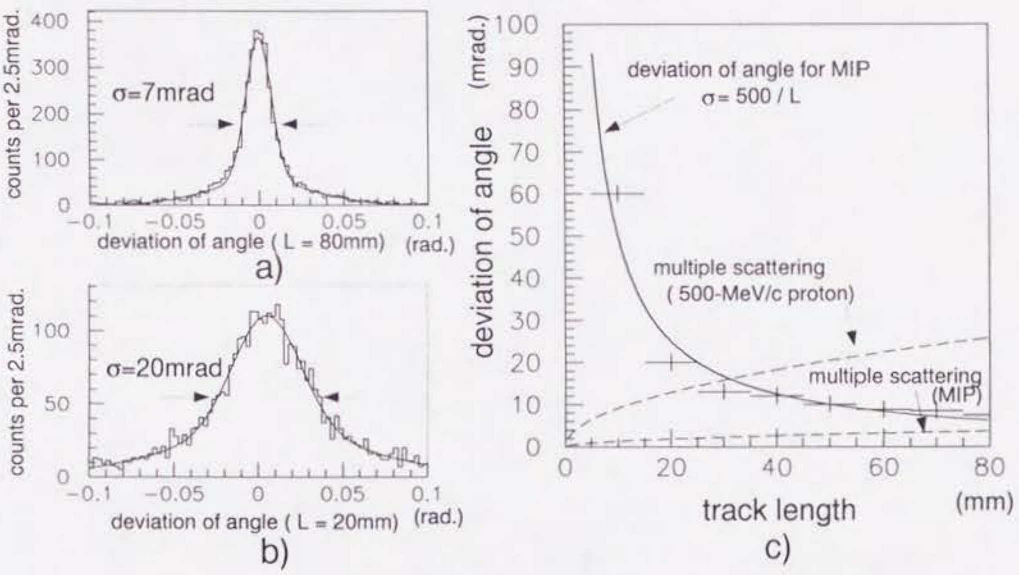


Figure 19: Angular deviations of the tracks of MIP's from the predictions with the spectrometer, a) for the track length (L) of 80 mm and b) for that of 20 mm. c) The angular resolution against the track length. The dependence on the track length is well described by the formula, $\sigma_\theta = 500/L$ mrad., which is shown as the solid line. The limits due to multiple scattering are shown with the dotted lines.

of the kinematical reconstruction.

### 3.3.1 Scanning of events

A typical $\Xi^-$ decay event is shown in Fig. 20. First of all, $K^-$ and $K^+$ tracks have been recognized using the external position information given by the counter system in the beam line and the $K^+$ spectrometer. The accuracy of the prediction for the $K^+$ has been 500 $\mu$m for the picture on the X-Z projection and 800 $\mu$m for the Y-Z projection. The accuracy for the prediction of the beam position has been about 1mm for both projections. Accidental overlapping of incident tracks have been separated by means of those predictions.

The $(K^-, K^+)$ reaction point has been identified as the cross point of the $K^-$ and $K^+$ tracks. When the emission of one or more charged particles are observed, the $(K^-, K^+)$ reaction point has been apparently identified as a vertex of multi prongs.

The $\Xi^-$'s and $\Sigma^-$'s have been identified by observing the "kink" topology due to weak-decays such as $\Xi^- \to \Lambda\pi^-$ and $\Sigma^- \to n\pi^-$. These weak-decays have been identified also with the sudden change of the brightness since the ionization of $\pi^-$, a decay product, is 1/4 of that of slow hyperons. Weak-decays of $\Lambda$'s have been identified by "Vee"-like topology formed with the decay products, proton and $\pi^-$.

Since the tracks on the X-Z and the Y-Z projections have the "same" Z-position, the correspondence between the tracks on the two projections has been done by referring the Z-position. The tracks of escaped particles, however, may have a stereo ambiguity similar to that of multi-wire chambers. Such an ambiguity can be solved using the external information or the internal kinematical constraint, for example, on the coplanarity.

### 3.3.2 Three-dimensional event reconstruction

Positions of $(K^-, K^+)$ interactions and decay positions of hyperons such as the $\Xi^-$ and $\Lambda$ have been measured on an event-display screen. Those positions have been examined by means of the method of the center-of-gravity of the brightness inside the square of 2 mm around the measured position. For the track identification a

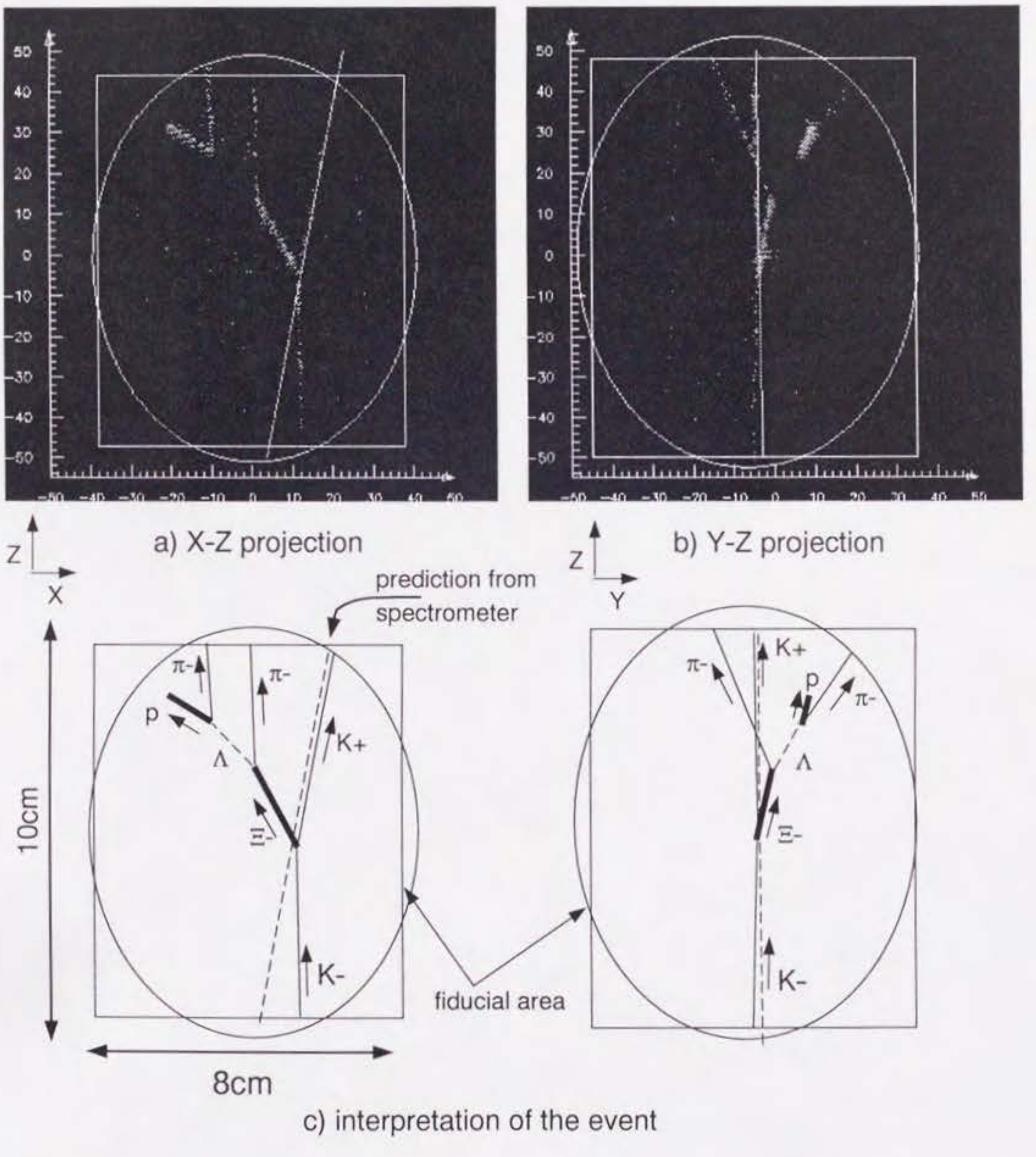


Figure 20: The display of a typical $\Xi^-$ decay. The weak-decay sequences of $\Xi^- \rightarrow \Lambda + \pi^-$ and $\Lambda \rightarrow n + \pi^-$ are clearly identified. a) The X-Z projection obtained with the vertical IIT. b) The Y-Z projection obtained with the horizontal IIT. The track prediction with the K$^+$-spectrometer is also shown as lines on both pictures which have good agreement with the images of the track of $K^+$'s. c) Interpretations of the tracks in a) and b).

corridor has been defined along the track, and the pixels in the corridor have been used for the straight-line fit to obtain a two-dimensional track. Finally the tracks in both projections have been combined to obtain a three-dimensional track. The vertex position has been defined as the closest position of the two tracks. The coplanarities of the tracks of the particles in $\Xi^- \to \Lambda\pi^-$ decay and $\Lambda \to p\pi^-$ decay are shown in Fig. 21 which show typical performance of the three-dimensional reconstruction in the SCIFI-target.

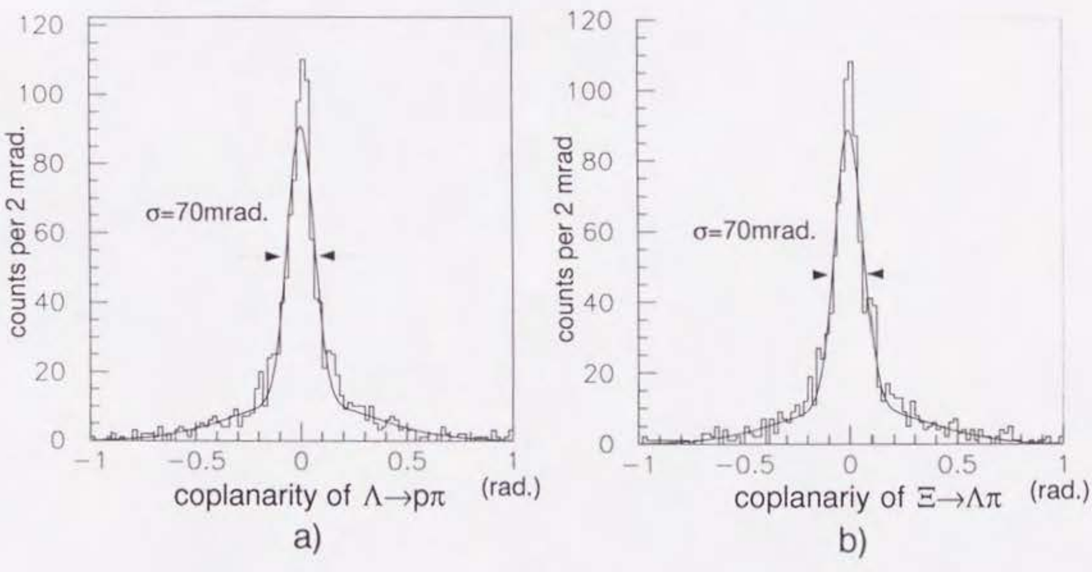


Figure 21: The coplanarities of decays, a) $\Lambda \to n\pi^-$ and b) $\Xi^- \to \Lambda\pi^-$. The coplanarity is defined as the angle between the direction of the mother particle and the decay plane

### 3.3.3 Kinematical reconstruction by means of the range measurement

The ranges of the particles have been obtained by the position measurement described in the previous section. The kinetic energy can be determined by the range in the SCIFI-target with the Bethe-Bloch formula. We have used the following empirical formula instead of the Bethe-Bloch formula for the sake of simplicity;

$$T = a \cdot R^b \; , \tag{7}$$

where $T$ is the kinetic energy of the particle, $a$ and $b$ are the constants given in Table 2 and $R$ is the range in the SCIFI-target of the particle. The accuracy for the range measurement has been 1 mm, which corresponds to the energy resolution of 10% for stopped protons of 1 cm long. The calibration has been done with stopped protons with the kinetic energy of 40 MeV at INS SF-cyclotron [41].

| | $\pi^-$ | proton | $\Sigma^-$ | $\Xi^-$ |
|---|---|---|---|---|
| $a$ | 14.1 | 32.5 | 36.3 | 38.0 |
| $b$ | 0.5653 | 0.5553 | 0.5535 | 0.5521 |

Table 2: The coefficients $a$ and $b$ for various particles which are used for the calculation of the kinetic energy from the range in the SCIFI-target. The parameters are given for the range $R$ in cm and the kinetic energy $T$ in MeV ( see the text).

If one of the charged particles from two-body decays stops in the SCIFI-target, the mass $M_0$ and momentum $p_0$ of the mother particle can be calculated as follows. Using the measured range $R$ and the decay angles $\theta_1$ and $\theta_2$ as shown in Fig. 22-a), the momentum of the mother particle, $p_0$, is determined from the momenta of decay products $p_1$ and $p_2$ as

$$p_0 = p_1 \cos\theta_1 + p_2 \cos\theta_2, \text{ where } p_1 = \sqrt{(a \cdot R^b + M_1)^2 - M_1^2} \text{ and } p_2 = p_1 \frac{\sin\theta_1}{\sin\theta_2}. \quad (8)$$

Here $M_1$ is the rest mass of proton. Then the mass $M_0$ can be obtained as

$$M_0 = \sqrt{E_0^2 - p_0^2} \quad \text{with} \quad E_0 = \sqrt{p_1^2 + M_1^2} + \sqrt{p_2^2 + M_2^2}. \quad (9)$$

Here we need to assume the mass of the decay products $M_1$, and $M_2$. The reconstructed mass distribution of $\Lambda$ are presented in Fig. 22-b), in which the mass resolution is shown to be 15 MeV/$c^2$.

### 3.3.4 Detection efficiencies for scanning

**Detection of single tracks:** A cluster with 3 photons or more has been required for the identification of the track. Since a track of MIP produces a cluster with 0.55 photon per mm in average, the track of 15 mm long has about 8 photons, which gives the detection efficiency of about 99%. If a particle doesn't pass through two layers of the scintillating-fiber-sheets, the track appears only in the X-Z or the Y-Z picture

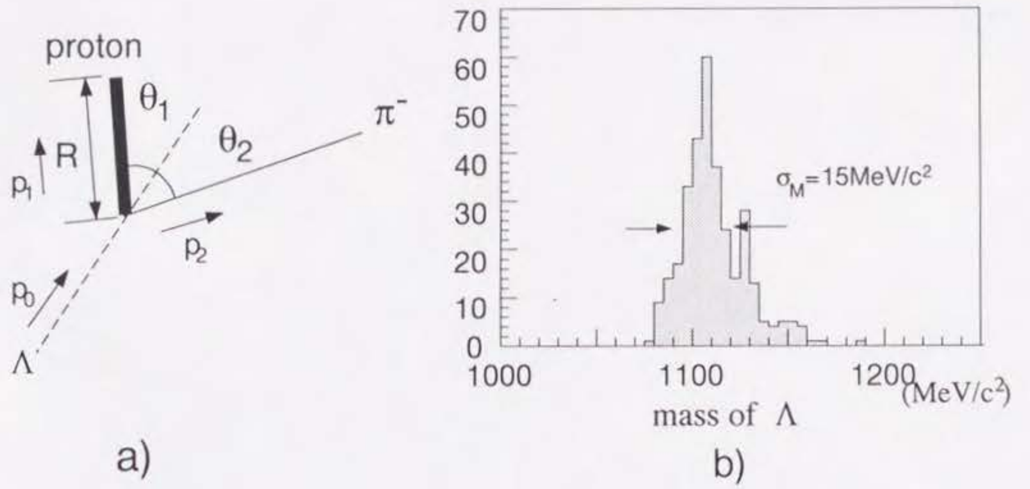


Figure 22: a) The kinematical parameters in the two body decay $\Lambda \rightarrow p\pi^-$ are shown. The $R$ is defined as the range of proton. b) The distribution of the reconstructed mass of Λ from $\Xi^-$ decay.

since the fiber-sheets are stacked alternately for both directions. A track must be longer than 1.5 mm (more than 3 layers) along the beam axis for three-dimensional reconstruction.

**Detection efficiency for $\Xi^-$:** The $\Xi^-$ and Λ are identified by observing their weak-decay topologies that show "kink-track" or "Vee-track" in pictures. The detection efficiency for $\Xi^-$'s is low in the case that the decay position of $\Xi^-$ is close to the vertex point of the $(K^-,K^+)$ reaction. Such a low efficiency is due to the minimum visible distance between the vertex position and the decay position in the SCIFI-target. It is shown in the decay length distribution of $\Xi^-$ in Fig. 23 a). The detection efficiency, $\eta_\Xi$, as a function of the decay length, $R_\Xi$, was deduced by comparing the measured decay length distribution to that of the Monte Carlo simulation described in Appendix B. The efficiency is consistent with unity if the decay length is longer than 5mm as shown in Fig 23-b). We neglect the dependence of the efficiency on the flight length of $\pi^-$, $R_\pi$, since the track of $\pi^-$ produced in the $\Xi^-$ decay has sufficiently long flight length in the SCIFI-target.

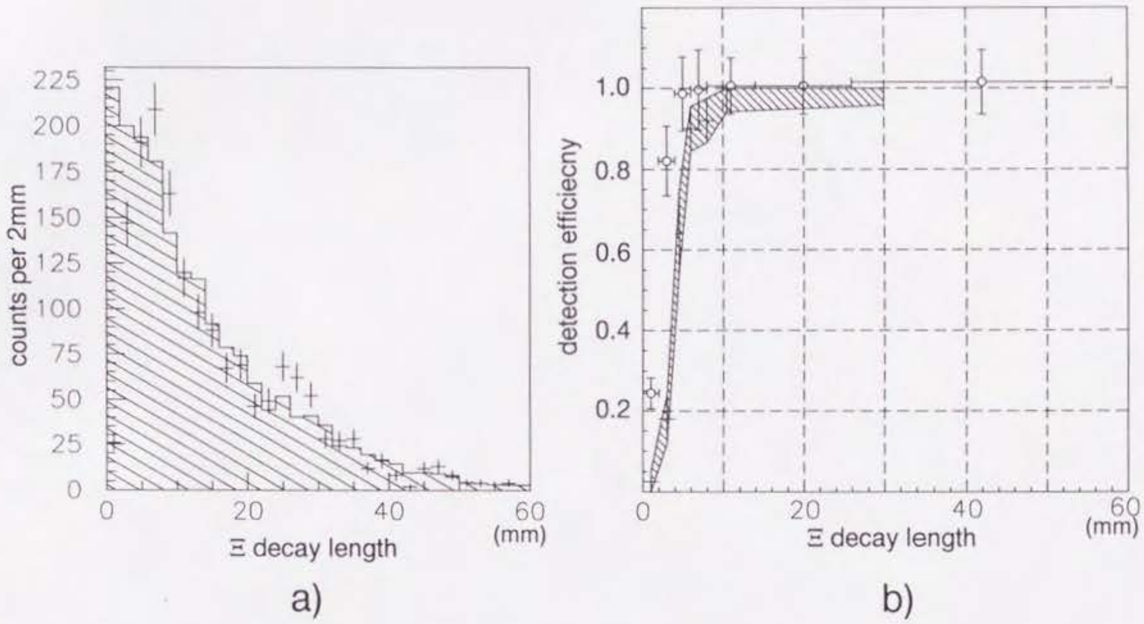


Figure 23: a) The decay length distribution of $\Xi^-$'s which are associated with charged decays of $\Lambda$'s is shown with the crosses. The hatched histogram shows the result of a calculation by a Monte Carlo simulation. The normalization has been done in the region where the decay length is 10 mm to 30 mm. b) The detection efficiencies for $\Xi^-$'s as a function of the decay length are shown as the open circles. They are obtained as the ratio of the observed data to the results of simulation. The error bar corresponds to one standard deviation of the statistical error. Also are shown the detection efficiency deduced from the simulated pictures. The width of the hatched area corresponds to one standard deviation of the statistical error.

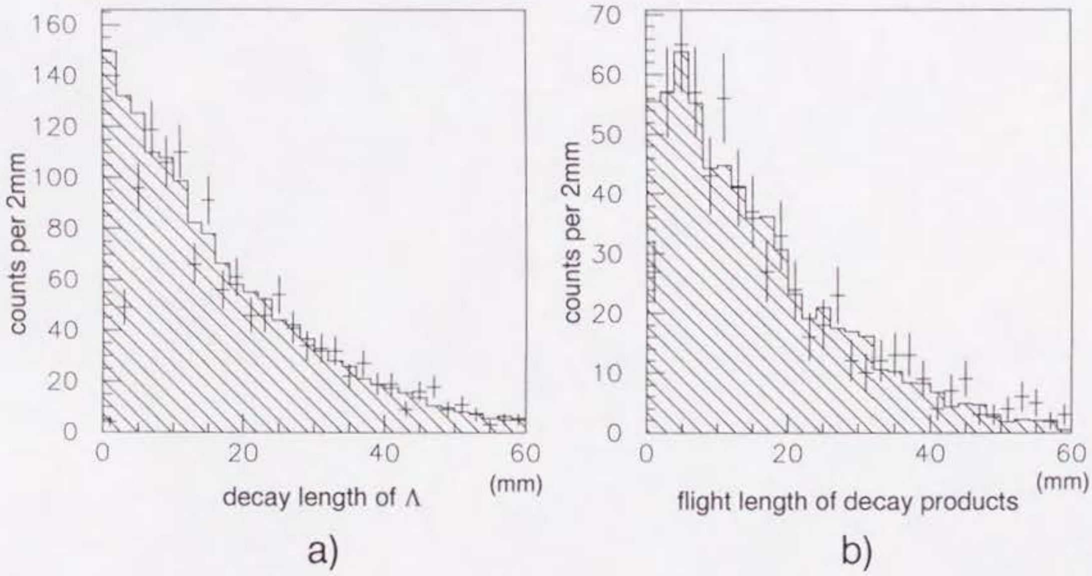


Figure 24: a) The decay length distribution of Λ's is shown. The hatched histogram is an expected distribution from a Monte Carlo simulation. The normalization has been done in the region where the decay length is 10 mm to 30 mm. b) The flight lengths of one of the charged decay products of Λ's are shown. The shortest track among the proton and $\pi^-$ from Λ decay is adopted. The hatched histogram is an expected one obtained by a Monte Carlo simulation. The normalization has been done in the region where the decay length is 10 mm to 30 mm.

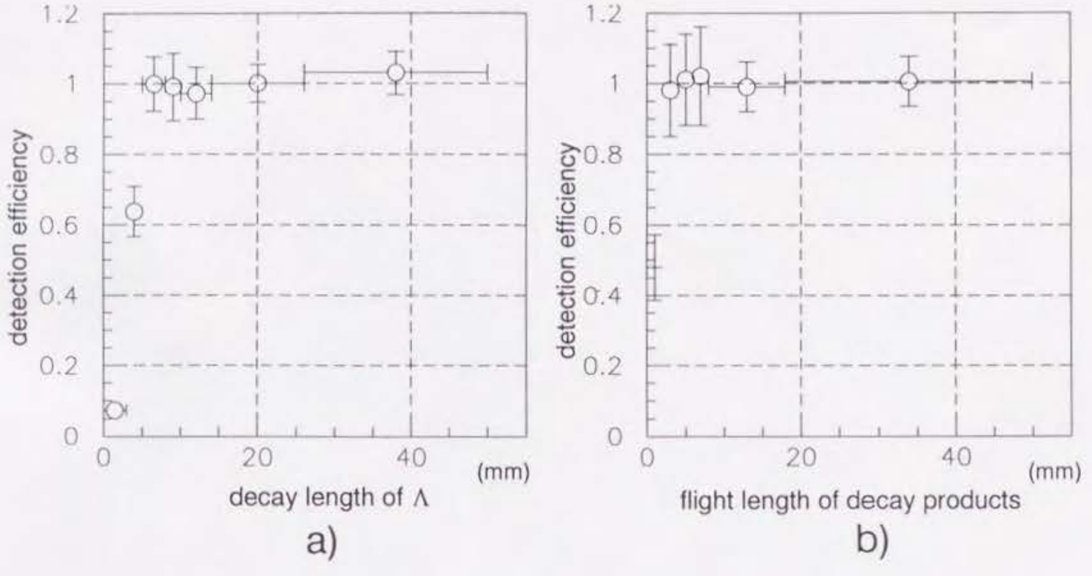


Figure 25: a) The detection efficiency for $\Lambda$ as a function of its decay length $R_\Lambda$ where $R_p$ is longer than 5 mm. b) The detection efficiency for $\Lambda$ as a function of the flight length shortest track of its decay products $R_p$, where $R_\Lambda$ is longer than 5 mm.

**The detection efficiency for $\Lambda$:** The similar effects are also observed in the detection of $\Lambda$'s by means of the search for "Vee-track". In this case, the efficiency, $\eta_\Lambda$, depends on the $\Lambda$ decay length, $R_\Lambda$, and the flight-length of the shortest decay products, $R_p$.

The decay length distribution of $\Lambda$ obtained from the $\Xi^-$ decay and the flight length distribution of the shortest decay products in the $\Lambda$ decay are shown in Fig. 24. We have obtained the efficiencies by comparing them to the expected distributions derived from a Monte Carlo simulation. Figure 25 shows the efficiencies as a function of the decay length of $\Lambda$, $\eta_\Lambda(R_\Lambda)$, and that as a function of the length of the shortest decay products, $\eta'_\Lambda(R_p)$. The efficiencies, $\eta_\Xi(R_\Xi)$ and $\eta_\Lambda(R_\Lambda)$ are in good agreement each other, while $\eta'_\Lambda(R_p)$ shows higher values in the region of $R_p \leq 5$ mm.

**Examination by the simulated pictures:** We have exmained $\eta_\Xi(R_\Xi)$ and $\eta_\Lambda(R_\Lambda, R_p)$ by scanning the simulated pictures generated by the GEANT program as mentioned in Appendix B. The pictures of quasi-free $\Xi^-$ productions in $(CH)_n$ with the decay sequences have been reconstructed by the same method as the analysis of the experimental data. The obtained efficiency curve for finding a $\Xi^-$ as a function of the decay length agrees with that of the experimental data as shown in Fig. 23. In the region $R_\Xi \geq 5$ mm, 147 events have been found to be detected among 155 generated samples. It corresponds to the efficiency of 95%. The $\eta_\Lambda(R_\Lambda, R_p)$ also has been examined by scanning the same pictures. The correlation between $R_\Lambda$ and $R_p$ is shown in Fig. 26. Here the open circles show the detected events while closed circles are ones which are not detected. In the region of $R_\Lambda \geq 5$ mm and $R_p \geq 5$ mm total 44 events among 46 generated samples are detected. It corresponds to the efficiency of 95%. Two events have not been found due to the accidental overlapping of tracks described below.

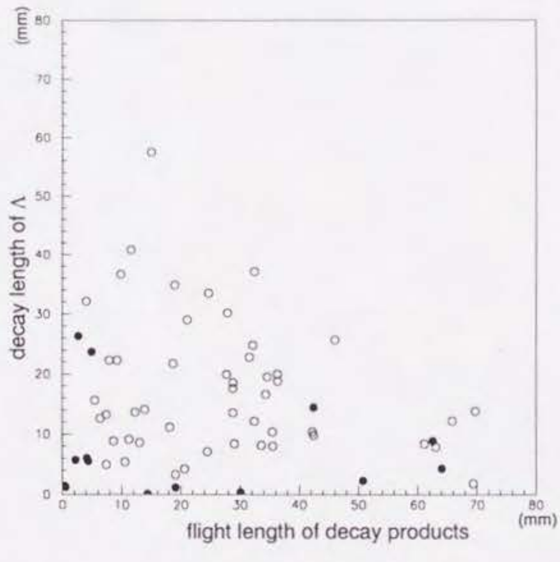


Figure 26: The simulated correlation of the decay length of $\Lambda$ against the flight length of the shortest track of the decay products. The open circles shows the events have been detected in the scanning and the closed circles show undetected ones.

**Inefficiency from other sources:** We discuss the origins of inefficiency which are not attributed to the minimum visible distance between two tracks. Several cases are considered.

One of the sources is an accidental overlap of tracks at a vertex point. Such kind of inefficiency occurs when a $K^+$ track or a tracks of beam particle overlap accidentally at the vertex point of a "Vee-track" in both of the X-Z and Y-Z pictures.

The effect becomes negligible if the distance between the vertex point and the track of the particles is longer than 1 mm in one of the pictures. The inefficiency due to the overlapping has been estimated to be about 2% in the case of $\Xi^-$ decays.

The inefficiency comes also from the uncertainty of determination of the angle between two decay products. The minimum detectable angle of a "kink-track" has been estimated from the angular resolution of the SCIFI-target, which is about 50 mrad. for a track of 1cm long. Although the inefficiency owing to such an origin is negligible in the case of $\Xi^-$ decay, but the effects are strongly correlated with the event kinematics. Detailed evaluation of the detection efficiency for the $H \to \Sigma^- p$ search is discussed in Section 4.

# 4 Analysis of the possible candidates for the $H$ particle

## 4.1 Pre-selection by $(K^-, K^+)$ tagging

### 4.1.1 Analysis of $K^-$

We have collected $5\times10^6$ triggers in the SCIFI-target. The background events due to other reactions included in the $(K^-, K^+)$ reactions have been eliminated in the off-line analysis in order to obtain true $(K^-, K^+)$ reactions.

The incident $K^-$'s have been selected using the aerogel Čelenkov counter in the on-line trigger process and have identified using the information of time-of-flight between T1 and T2 in the off-line analysis. The TDC data of T1 and T2 have been corrected with the pulse hight information obtained with the ADC data. The resolution of time-of-flight was 85 psec. The obtained histogram of the time difference between T1 and T2 is shown in Fig. 27. To reject the contamination with $\pi^-$ and $\overline{p}$, we have used $K^-$'s of which deviation from the center of the time-of-flight spectrum was within $\pm$300psec.

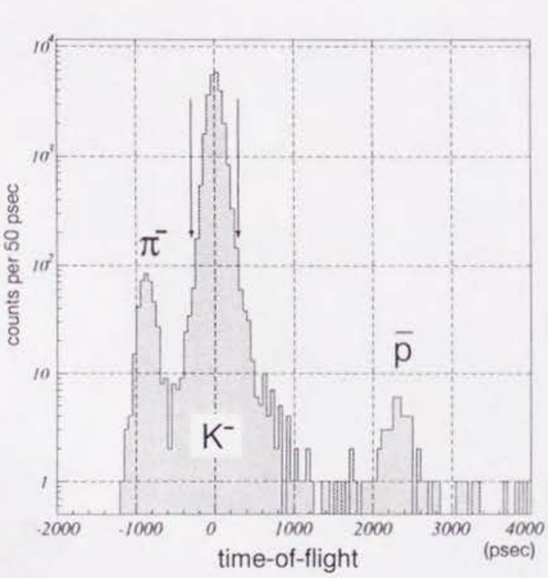


Figure 27: The TOF spectrum of the incident particles. The arrows show cut values to obtain $K^-$'s

The tracks of the $K^-$'s have been obtained from the hit positions on BPC3, BPC4 and BPC5 using the beam transportation matrix. They have been useful for the position prediction of $K^-$ in the SCIFI-target. The reconstruction efficiency has been 80%.

### 4.1.2 Analysis of $K^+$

The scattered particles with positive charge have been selected by the first-level trigger with use of the information from CT and FTOF. The contamination with $\pi^+$ has been eliminated with the veto signal from SAC. The contamination with proton has been reduced by the mass trigger. In the off-line analysis the momenta of particles have been determined by using the data on the the hit positions on the drift chambers and the FTOF counter.

The tracks of the $K^+$'s have been obtained from the hit positions on CDC, DC1, DC2, DC3 and FTOF. The FTOF has provided the vertical position by using the time difference between the signal from the photo-tube on both the top and the bottom of the counter. The spatial resolution is 14.8 mm in vertical direction. We required the hits all on the vertical and horizontal planes of DC1, DC2, DC3 and at least 4 hits on CDC in the region of the acceptance of the $K^+$-spectrometer. First the spline fit on these hits and then the Runge-Kutta fit have been applied to obtain the trajectories and the momenta of the scattered particles. We have rejected the tracks of which positions predicted by FTOF is different from the positions of the tracks by more than 7 cm in horizontal or than 3 cm in vertical. The background events due to $K^-$ decays have been rejected with this cut. The tracking efficiency is about 80% in total.

The velocity of the particle has been determined by the time-of-flight measurement between T2 and FTOF after pulse-hight correction of TDC data. The resolution of time-of-flight is 110 psec. The mass of the scattered particle has been calculated to be;

$$M = p \cdot \sqrt{\beta^{-2} - 1}, \tag{10}$$

where $M$, $p$ and $\beta$ are the mass, momentum and velocity of the particle, respectively. The obtained mass distribution is shown in Fig. 28. The particles in the mass region of 400 MeV/$c^2$ to 600 MeV/$c^2$ of the spectrum has been selected as the $K^+$'s. The

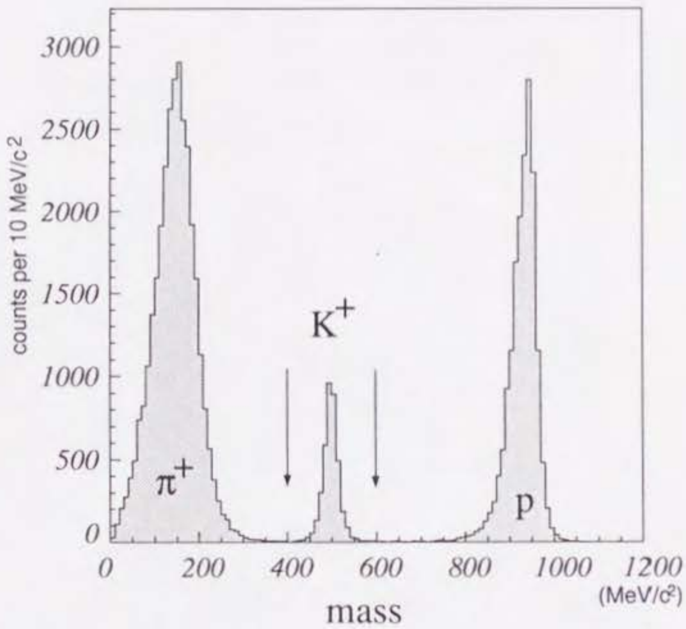


Figure 28: The mass spectrum of the scattered particles. The particles in the region between two arrows have been selected as the $K^+$'s

mass resolution for the $K^+$ is 18.5 MeV/$c^2$. The obtained momentum spectrum for $K^+$ is shown in Fig. 29. The momentum resolution has been obtained to be 0.5% at 1.1 GeV/$c$.

The total number of the $(K^-, K^+)$ reactions tagged by the spectrometer is about 10,000. The number of contamination misidentified as the $K^+$ deduced from the tail of mass spectrum is less than 1% of the total number of the $K^+$. The backgrounds are from $(K^-, \pi^+)$ reactions. Another background is due to the $K^0$ production, which are eliminated by analyzing the SCIFI-data as explained in Section 4.2.

## 4.2 Scanning of quasi-free ($K^-$,$K^+$) reaction

The pictures of $(K^-, K^+)$ reactions tagged by the spectrometer have been scanned by human eyes and have been categorized to the $(K^-, K^+)$ reactions into several cases according to the event topologies[41]. The results of the classification are shown in Table 3. We have required that the $(K^-, K^+)$ reaction point has been observed in the fiducial area. We have rejected the background events due to the neutral kaon

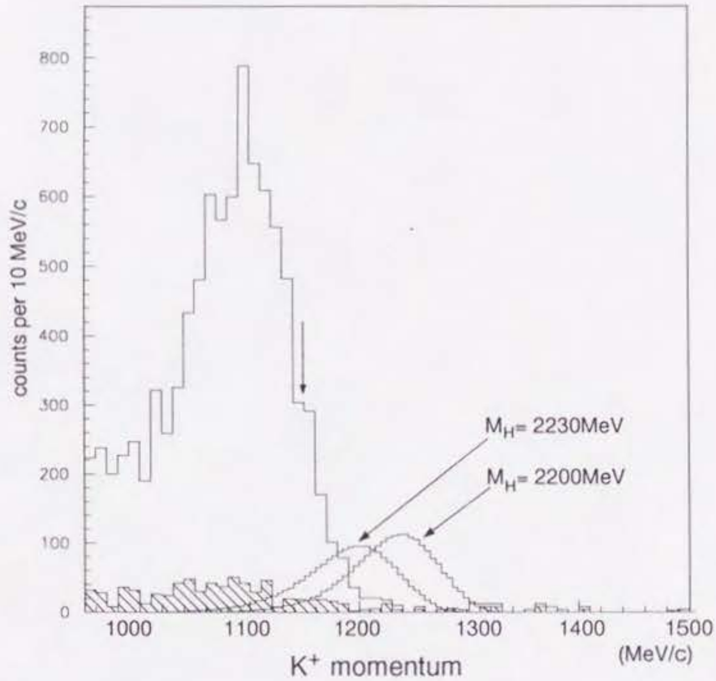


Figure 29: The momentum spectrum of $K^+$. The plain histogram shows the data before the deduction by SCIFI-data. The hatched histogram shows the background events rejected by scanning SCIFI-data. Also shown are the peaks corresponding to the direct $H$ production for $M_H$=2200 MeV/$c^2$ and $M_H$=2230 MeV/$c^2$ in the process, $K^- + (pp) \rightarrow K^+ + H$ expected from a Monte Carlo simulation. The arrow shows the $K^+$-momentum cut to analyze the data of direct $H$ production.

| | $p_{K^+} \geq$950MeV/$c$ | $p_{K^+} \geq$1150MeV/$c$ |
|---|---|---|
| $(K^-, K^+)$ in fiducial | 8294 | 697 |
| $(K^-, K^+)$ out of fiducial | 1537 | 149 |
| neutral kaon | 172 | 57 |
| prediction mismatched | 359 | 44 |
| double scattering | 47 | 8 |

Table 3: The numbers of $(K^-, K^+)$ events and background events deduced by scanning the pictures. Here "prediction mismatched" means the events of which positions of $K^+$ tracks mismatches with the predicted tracks from $K^+$-spectrometer.

productions;

$$K^- + p \to K^0 + n, \quad K^0 \to \overline{K^0}, \quad \text{then} \quad \overline{K^0} + p \to K^+ + n, \tag{11}$$

and

$$K^- + p \to K^0 + n, \quad \text{then} \quad K^0 \to \pi^+ + \pi^-, \tag{12}$$

In the latter case, the $\pi^+$ has been miss-identified as the $K^+$. These events have been rejected by observing the disconnection of the $K^-$ track and the $K^+$ track which corresponds to the neutral kaons. We have rejected the events of which $K^-$ or the $K^+$ were scattered additionally in the picture. We have rejected also the events of which the positions of the $K^+$ tracks mismatch with the predicted position given by the information from the spectrometers.

The number of $(K^-, K^+)$ reactions after these selections is 8,294. We have studied the pictures more carefully in the region where $K^+$ momenta are greater than 1150MeV/$c$ in order to search for the $H$ dibaryon which decays into $\Sigma^-$ and proton.

## 4.3 Search for the $H$ decay in $P_{K^+}$ ≥1150 MeV/$c$

### 4.3.1 Expected signal of the $H$ : decay topology

In this section we discuss the kinematics of production and the decay of $H$ into $\Sigma^- p$. We have searched for the $H$ produced in a carbon nucleus directly through the process;

$$K^- + (pp) \to H + K^+, \tag{13}$$

where $(pp)$ is a proton-pair in a carbon nucleus.

The momentum distribution of $K^+$'s for the $H$ mass of interest has been calculated by a Monte Carlo simulation assuming the process above. The results are shown in Fig. 29. The momentum of $K^+$ decreases with the increase of the $H$ mass. The lower limit of $K^+$ is about 1100 MeV/c for $M_H$=2230 MeV/$c^2$. We have put an emphasis on the heavy $H$ search (2200 MeV/$c^2$ $\leq M_H \leq$2230 MeV/$c^2$). We have analyzed the events in which $K^+$'s have momenta higher than 1150 MeV/$c$. This cut gives 90% efficiency for the analysis.

Under these constraints, the reactions;

$$K^- + (pp) \to H + K^+ + \pi^0 \quad , \quad \text{and} \tag{14}$$

$$K^- + (pn) \to H + K^+ + \pi^- \tag{15}$$

are not allowed kinematically. Therefore, no charged particles should be observed at the $(K^-, K^+)$ vertex point except short ones (less than a few cm) which are possibly low-energy protons evaporated from the residual nucleus.

A signature of the $H$ is the sequential weak decay chain ;

$$H \to \Sigma^- + p, \quad \text{then} \quad \Sigma^- \to \pi^- + n. \tag{16}$$

The decay length distribution of $H$ calculated by a Monte Carlo simulation is shown in Fig. 30-a) in the case that the lifetime of $H$ is $3\times10^{-10}$. In this case, about 70% of the $H$ is expected to decay in the SCIFI-target.

The charged decay products, the $\Sigma^-$ and proton, show a topology of a "Vee-track" which is similar to that of $\Lambda \to \pi^- p$ decay. Since the ionization of $\Sigma^-$ and proton are more than 4 times as large as these of minimum ionizing particles, a significant difference in "brightness" of the tracks from minimum ionizing tracks is observed. The distribution of the flight length of the proton is shown in Fig. 30-b). About 50% of the protons stops in the SCIFI-target and the rests escape from the target. As shown in Fig. 30-c), the mean decay length of $\Sigma^-$ is about 10 mm. About 60% of $\Sigma^-$'s is expected to decay into $\pi^- n$ with the 100% branching ratio in the SCIFI-target, and about 10% is expected to stop and interact with material in the SCIFI-target. The rests are expected to escape from the target. A momentum of the $\pi^-$ from the $\Sigma^-$ decay is around 200 MeV/$c$. Although about 99% of $\pi^-$ have momenta sufficient to escape from the SCIFI-target, the reaction cross section of $\pi^-$ is large at this momentum region (about 360 mb for carbon) because of the $\Delta$ resonance. Thus some of the $\pi^-$'s interact with a nucleus in the target. Taking this effect into account, we have estimated that the probability of escape of $\pi^-$ from the target is about 90%. It produces a minimum ionizing track in the picture. Thus the decay chain of the $H$ is observed in the picture as a "kinked Vee-track" as shown in Fig. 31, which we search for as the signature of $H$.

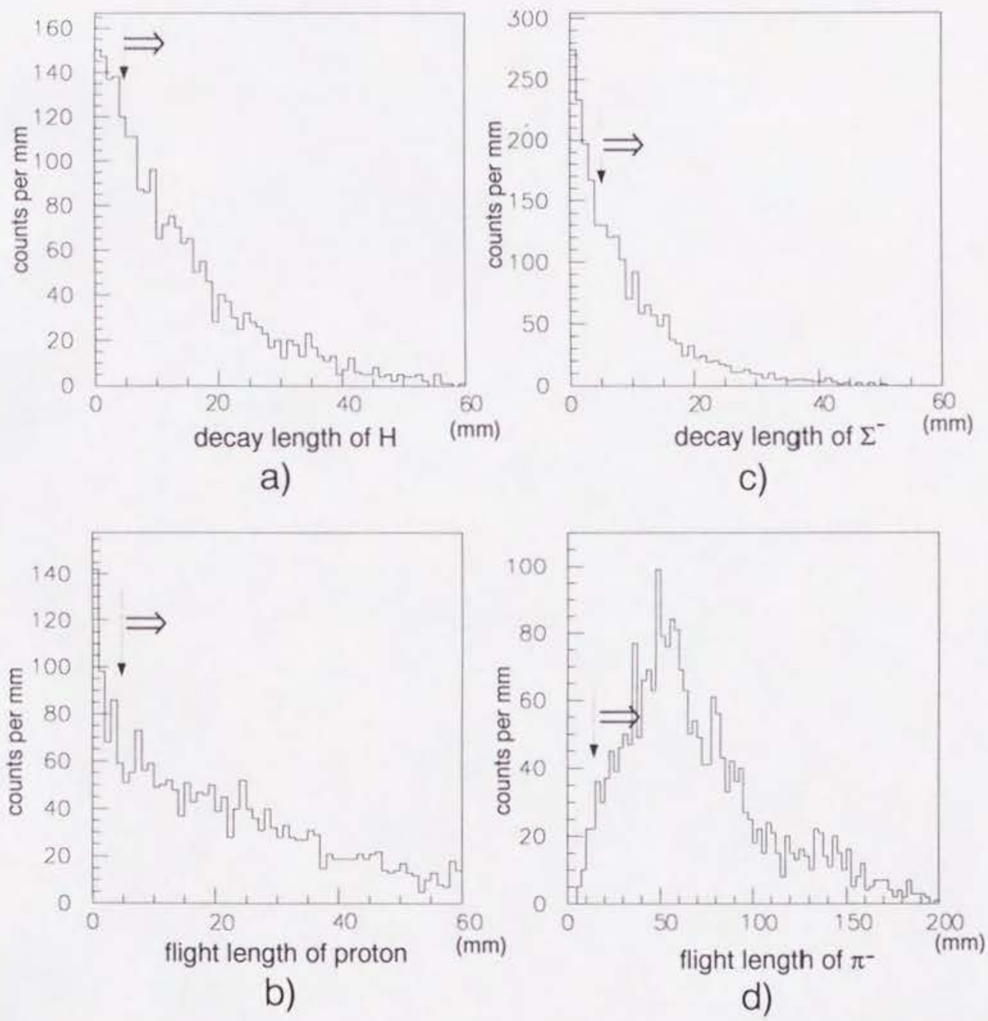


Figure 30: a) Results of a Monte Carlo simulation which show the decay length of $H$. b) The flight length of the proton, one of the decay products of $H$, in the SCIFI-target. c) The decay length of the $\Sigma^-$ produced in the $H$ decay. d) The flight length of the $\pi^-$ from the $\Sigma^-$ decay. The mass of $H$ is assumed to be 2200 MeV/$c^2$ and the lifetime of $H$ is assumed to be $3\times10^{-10}$ sec. The arrows show the cut value according to the requirements B and C (see the text).

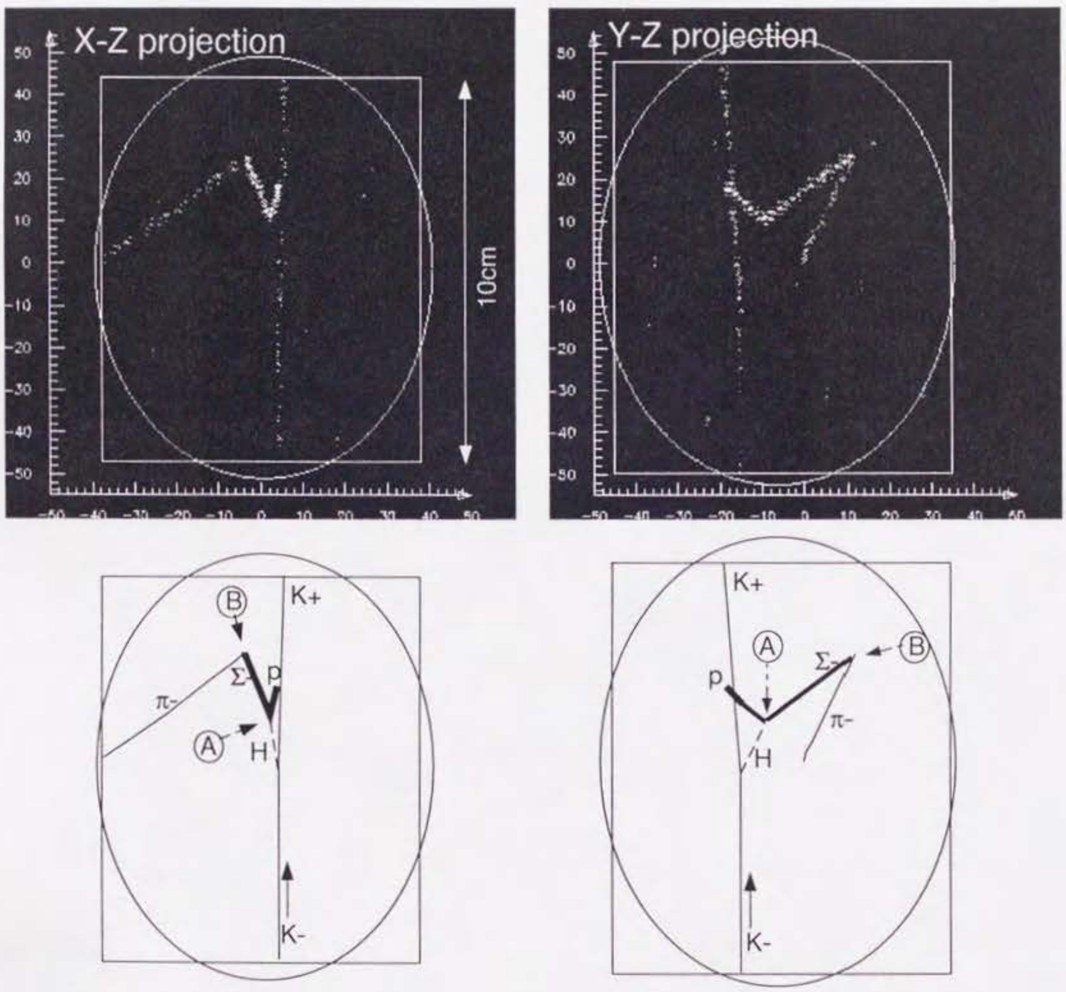


Figure 31: A typical track image of $H \to \Sigma^- p$ generated by the GEANT simulation. Such a track is . The production of $H$ via a reaction $K^- + (pp) \to K^+ + H$ and sequential weak decays, $H \to \Sigma^- + p$, then $\Sigma^- \to n\pi^-$ are shown. Such a track image is named as "kinked Vee-track" which is expected to be detected in the SCIFI-target (see the text).

### 4.3.2 Requirements to search for "kinked Vee-track"

Considering the conditions discussed above, we have set the following requirements for the "kinked Vee-track" as a $H \rightarrow \Sigma^- p$ candidate.

**Requirement A:** The two kink points , the decay point of $H \rightarrow \Sigma^- p$ (A in Fig. 31) and the decay point of $\Sigma^- \rightarrow n\pi^-$ (B in Fig. 31), are observed in the fiducial area of the picture.

The first one is simply related to the fiducial area of the detection. In addition, we require a $\pi^-$-like track for one of the decay products of $\Sigma^- \rightarrow n\pi^-$ as discussed in Section 4.3.1.

**Requirement B:** The $\pi^-$ from the $\Sigma^-$ decay has a flight length longer than 15 mm before it escapes from the fiducial area of the picture.

As discussed in the case of the $\Xi^-$ decay in Section 3, the $H$ whose decay point is close to the production point is difficult to be detected by scanning. The same difficulty occurs also for the decay of $\Sigma^-$. To evaluate detection efficiencies of these events, we have considered a "kinked Vee-track" as a combination of a "Vee-track" and a "kink-track". Then the detection efficiency of the "kinked Vee-track", $\eta_{KV}$, is evaluated as a simple multiplication of the detection efficiency for $\Xi^-$, $\eta_{\Xi}$, and that for $\Lambda$, $\eta_{\Lambda}$, as;

$$\eta_{KV} \sim \eta_{\Lambda}(R_H, R_p) \times \eta_{\Xi}(R_{\Sigma}) \times \eta_o \tag{17}$$

The $\eta_{KV}$ is the detection efficiency of the $H$ in the scanning of the "kinked Vee-track" in the pictures. Here we used $R_H$ (decay length of the $H$) instead of $R_{\Lambda}$ in $\Lambda$ decay and $R_{\Sigma}$ (decay length of $\Sigma$) instead of $R_{\Xi}$ in $\Xi^-$ decay.

As shown in Fig. 23 and Fig. 25, the detection efficiencies for the $\Sigma^-$, $\Lambda$ and proton are consistent with unity if the flight length longer than 5 mm. The evaluation of the efficiencies for the flight length shorter than 5 mm is difficult. On the basis of the above result, we must fulfill the following requirement.

**Requirement C:** The decay lengths of the $H$ and the $\Sigma^-$ produced in the decay $H \rightarrow \Sigma^- p$ are longer than 5 mm. The flight length of the produced proton is also longer than 5 mm.

We have defined the detection efficiencies due to the following requirements D,E and F as $\eta_o$. In contrast to the $\Lambda$ from the $\Xi^-$ decay, the $\Sigma^-$ and the proton from the $H$ decay go to opposite directions, thus the kink between them can be identified. The visibility is related to the angular resolutions of the tracks. Since we have set the minimum length to be 5 mm for each track the angular resolution $\sigma_\theta$ is 0.1 rad., which corresponds to the resolution of the opening angle of the kink to be 0.14 rad. We have required the angle between the $\Sigma^-$ and the proton, $\theta_{\Sigma p}$, and the angle between the $\Sigma^-$ and the $\pi^-$, $\theta_{\Sigma\pi}$, to be greater than $2 \cdot \sigma_\theta$, $\sim$0.28 rad. for one of the projected planes, X-Z or Y-Z.

**Requirement D:** Both $\theta_{\Sigma p}$ and $\theta_{\Sigma\pi}$ are more than twice of the angular resolution, that is 0.28 rad., in either of the X-Z or Y-Z plane.

To measure the three-dimensional positions of the initial and end points of tracks, we have required all the charged tracks to pass through at least 3 layers of fiber-sheets. It corresponds to the requirement for the flight lengths of $\Sigma^-$, proton and $\pi^-$ along the direction of the beam axis to be longer than 1.5 mm.

**Requirement E:** Charged tracks are longer than 1.5 mm perpendicular to the layers of the scintillating-fiber-sheets.

As seen in Section 3, the overlapping of tracks of $H \to \Sigma^- p$ with the $K^+$ track or that with other beam tracks causes the inefficiency. To avoid the ambiguity due to overlap we require the following condition.

**Requirement F:** The distance between the $K^+$ track and the decay point of $H$ is longer than 1 mm in either of the X-Z projection and the Y-Z projection.

### 4.3.3 Detection efficiency of "kinked Vee-track"

The overall detection efficiency of the scan is;

$$\eta_H = \eta_{P_K(M_H)} \times \eta_{decay}(M_H, \tau_H) \times \eta_{\pi out} \times \eta_{KV}(M_H, \tau_H), \tag{18}$$

where the $\eta_{P_K}$ is the fraction of the events in which momentum of $K^+$ is above 1150 MeV/$c^2$. The $\eta_{P_K}$ is about 0.95 for the total $H$ production in the case of $M_H$=2200

MeV/$c^2$ and about 0.83 in the case of $M_H = 2230$ MeV/$c^2$. The $\eta_{decay}$ is a fraction of the events which satisfy Requirement A. It is determined by the lifetime of $H$ and by that of $\Sigma^-$. The $\eta_{decay}$ calculated by a Monte Carlo simulation is about 60% for $H$ with the lifetime of $10^{-10}$sec and about 30% for that with $10^{-9}$ sec. The $\eta_{\pi out}$ is a fraction of the events which satisfy Requirement B. The $\eta_{\pi out}$ is insensitive to $M_H$ and $\tau_H$ due to the large Q-value of the decay $\Sigma^- \rightarrow \pi^- n$. It is 85% for the $H$ with the mass of 2200 MeV/$c^2$ and the lifetime of $3\times10^{-10}$ sec.

The $\eta_\Lambda(R_H, R_p) \times \eta_\Xi(R_\Sigma)$ is consistent with unity with Requirement C as discussed in Section 3. From the Monte Carlo study, about 30% of the $H$ remains after Requirement C are fulfilled for the $H$'s which have met Requirements A and B.

The efficiencies $\eta_D$, $\eta_E$ and $\eta_F$ due to Requirements D,E and F, respectively, have also been evaluated using a Monte Carlo simulation. In Requirement D, about 99% of the events remain after the $\theta_{\Sigma p}$ cut and about 95% remain after the $\theta_{\Sigma\pi}$ cut. The efficiency of $\eta_E$ is about 0.9, and that of $\eta_F$ is about 0.97. The efficiencies discussed here are summarized in Table. 4.

| Requirement | A | B | C | D | E | F | $p_{K^+} \geq$1150MeV/$c$ |
|---|---|---|---|---|---|---|---|
| efficiency of each cut (%) | 51.5 | 87.1 | 29.2 | 94.6 | 89.8 | 97.8 | 95.3 |
| efficiency of the combined cut (%) | 51.5 | 44.8 | 13.1 | 12.4 | 11.2 | 10.9 | 10.4 |

Table 4: The efficiencies of the cut according to Requirements A to F for the mass of 2200 MeV/$c^2$ and the lifetime of $3\times10^{-10}$ sec. The efficiencies in the lower column show the efficiencies of the combined cuts. For example, the efficiency in the column "C" shows that of the combined cuts A to C.

The detection efficiency of $H$, $\eta_H$, which meets all the requirements A to F is shown in Fig. 32 as functions of the mass and the lifetime. The efficiency has highest value, that is, 11% for $H$ with the mass of 2230 MeV/$c^2$ and the lifetime of $3\times10^{-10}$ sec. It slightly decreases with increase of the $H$ mass, whereas it is not so sensitive to the $H$ mass.

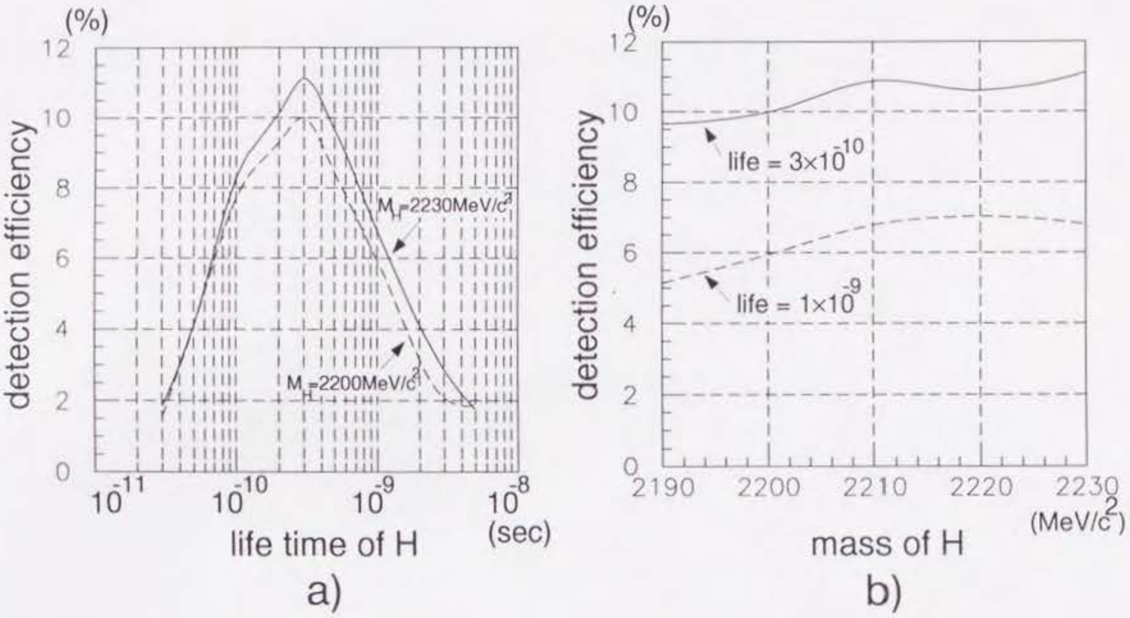


Figure 32: The overall detection efficiency of the $H$ decaying into $\Sigma^- p$. a) The efficiency as a function of the lifetime of $H$. The solid line shows the efficiency for $M_H$=2230 MeV/$c^2$ and the dashed line for $M_H$=2200 MeV/$c^2$. b) The overall efficiency as a function of the $H$ mass for the cases that the $\tau_H$ is $3 \times 10^{-10}$ sec and $3\times10^{-9}$ sec, respectively.

### 4.3.4 Evaluation of the detection efficiency by scanning of the simulated pictures

We have examined the detection efficiency for the $H$ by scanning simulated pictures of the $H \to \Sigma^- p$ decay generated by the GEANT program described in Appendix B. The example of a simulated picture of the $H$ decay is shown in Fig. 31.

The lifetime of the $H$ has been assumed to be $3 \times 10^{-10}$ sec and the mass to be 2200 MeV/$c^2$. To reduce the number of events to be scanned we have chosen the samples in which decays $H \to \Sigma^- p$ and $\Sigma^- \to \pi^- n$ have occurred in the fiducial area of the pictures. The flight lengths of $H$'s, $\Sigma^-$'s and protons are required to be longer than 1 mm. The number of the scanned samples is 193 while the number of generated events of the $H$ which decays into $\Sigma^- p$ is 518. We have mixed artificially 207 events which have $\Lambda$'s produced at the $(K^-, K^+)$ vertex and decayed into $p\pi^-$, in order to fake the $H \to \Sigma^- p$ events. This method has minimized a scanning bias due to the prejudice to the events. We have applied the same criteria and the same programs for scanning of the real data.

The correlation between $R_H$ and $R_\Sigma$ with $R_p \geq 5$ mm is shown in Fig. 33. The closed circles show detected events which are scattered in the region where the track lengths are greater than 5 mm. The open circles correspond to the events which are not detected ones.

After all the cuts from C to F have been performed, 44 events have been found, while 45 events have been expected from the detection efficiency described in the previous section. One event has not been found since the distance between the decay vertex of $H \to \Sigma^- p$ and the $K^+$ track is very close to the value required by F (2.3 mm in the X-Z picture and 0.9mm in the Y-Z picture). Thus we have concluded that the detection efficiency is almost 100% with Requirements A to F.

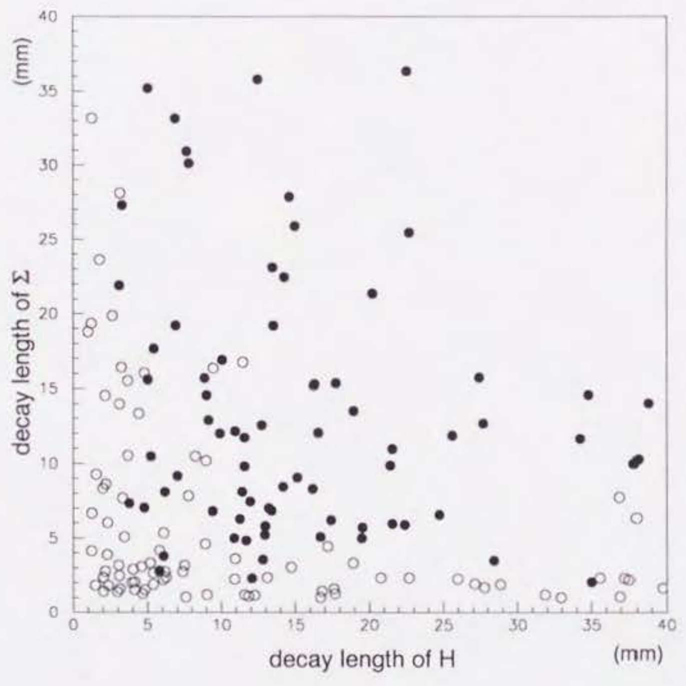


Figure 33: The result of scanning of simulated pictures of $H$. The correlation between the decay length of the $H$ and that of the $\Sigma^-$ is shown with the condition of the proton flight length being greater than 5 mm. The closed circles have been found by scanning, while the open circles have not been found.

### 4.3.5 Search for "kinked Vee-track"

Search for $H \to \Sigma^- p$ decay has been performed in the $K^+$ momentum region greater than 1150 MeV/$c$. The pictures of 697 events in this region have been scanned to find a "kinked Vee-track". First, we have carried out the cuts with Requirements A and B in order to search for the "kinked Vee-track"s from the event topologies. If the $H$ is produced via the quasi-free process, no charged track is observed at the $(K^-, K^+)$ vertex as discussed before. Nevertheless, we have not required any hypothesis for the topology of $(K^-, K^+)$ vertex in this scanning in order to be free from unknown bias about the production mechanism.

After Requirements A and B, 6 events have remained. By Requirements C to F applied for these 6 events, 2 events are discarded, since one of the charged tracks in "Vee-track" has not passed through more than 4 sheets. The 4 events have been reconstructed as the final samples to be examined with the kinematical constraints of $H \to \Sigma^- p$ decay.

## 4.4 Analysis of $H \to \Sigma^- p$ candidates

The pictures of the 4 events are shown in Fig. 34 to Fig. 37. The reconstructions of the three-dimensional tracks have been done by the similar method as described in Section 3. The summary of the 4 events are listed in Table 5. The two events B and D are associated with one prong at the $(K^-, K^+)$ vertexes which can be interpreted as possible $\pi^-$ emissions via $\Xi^-$ decays with short decay length. However, we have adopted them as candidates for further tests with kinematical constraints.

| event | A | B | C | D |
|---|---|---|---|---|
| $K^+$ momentum (MeV/$c$) | 1189 | 1192 | 1169 | 1223 |
| Number of prongs at $(K^-, K^+)$ vertex | 0 | 1 | 0 | 1 |
| Opening angle for $H$ decay (rad.) | 1.69±0.26 | 1.10±0.16 | 2.44±0.12 | 1.59±0.07 |
| Visible energy of proton(MeV) | 26.9±3.6 | 29.5±2.7 | 37.1±2.1 | 73.4±1.3* |
| Visible energy of $\Sigma^-$ (MeV) | 83.6±6.8 | 75.5±1.6 | 50.1±2.0 | 63.8±2.8 |

Table 5: The summary of $H \to \Sigma^- p$ candidates. The values with asterisk show the visible energy with escaped proton.

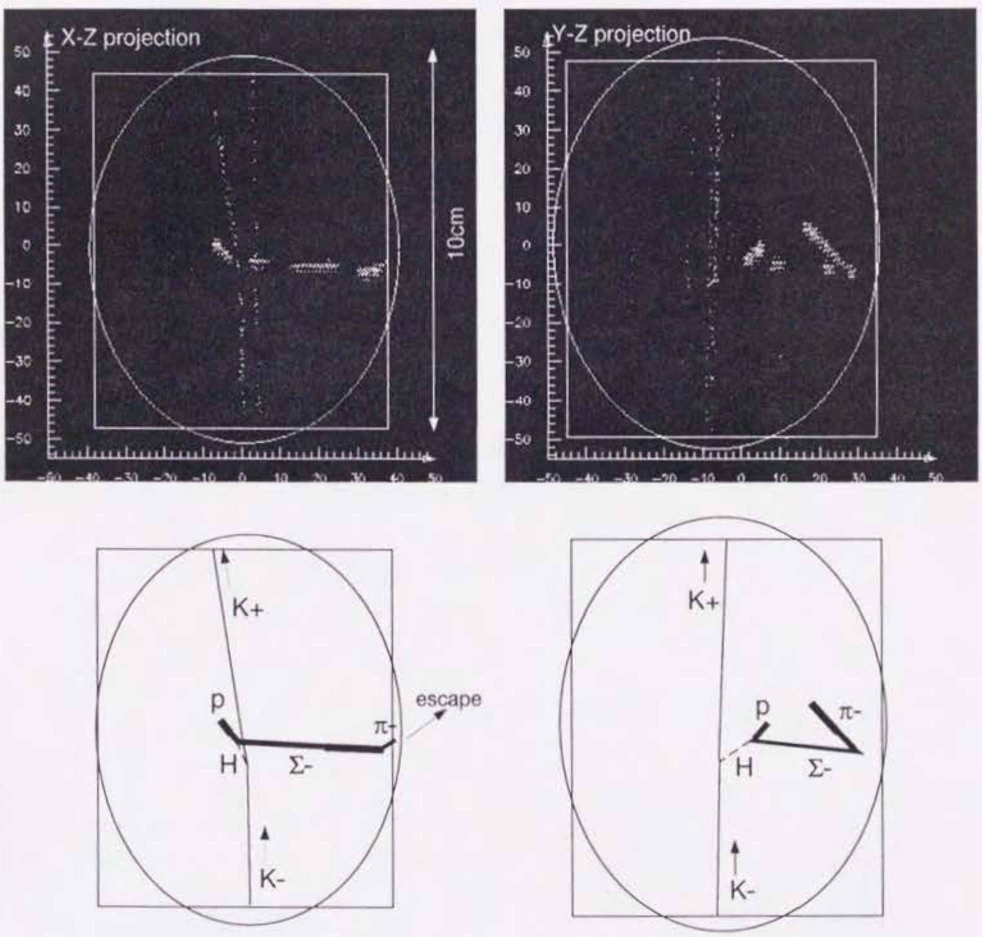


Figure 34: A candidate of "kinked Vee-track" Event A. A possible interpretation for the event is shown under the picture.

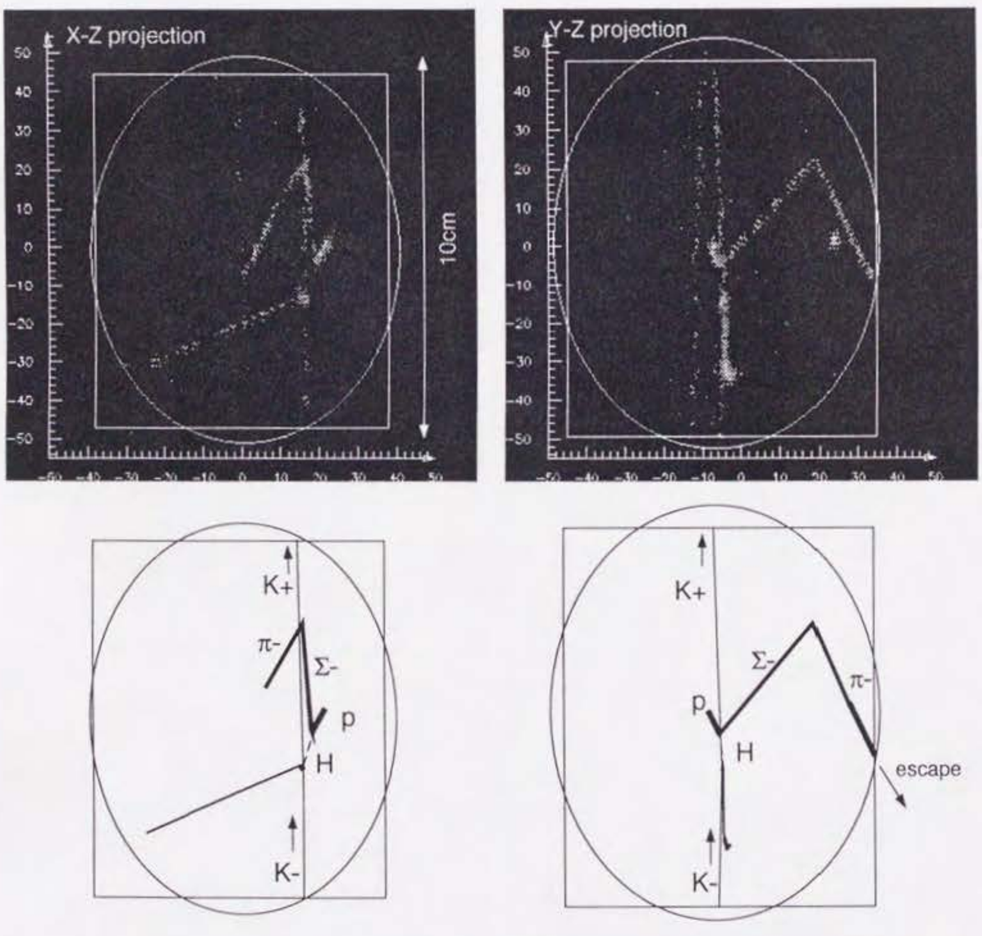


Figure 35: A candidate of "kinked Vee-track": Event B

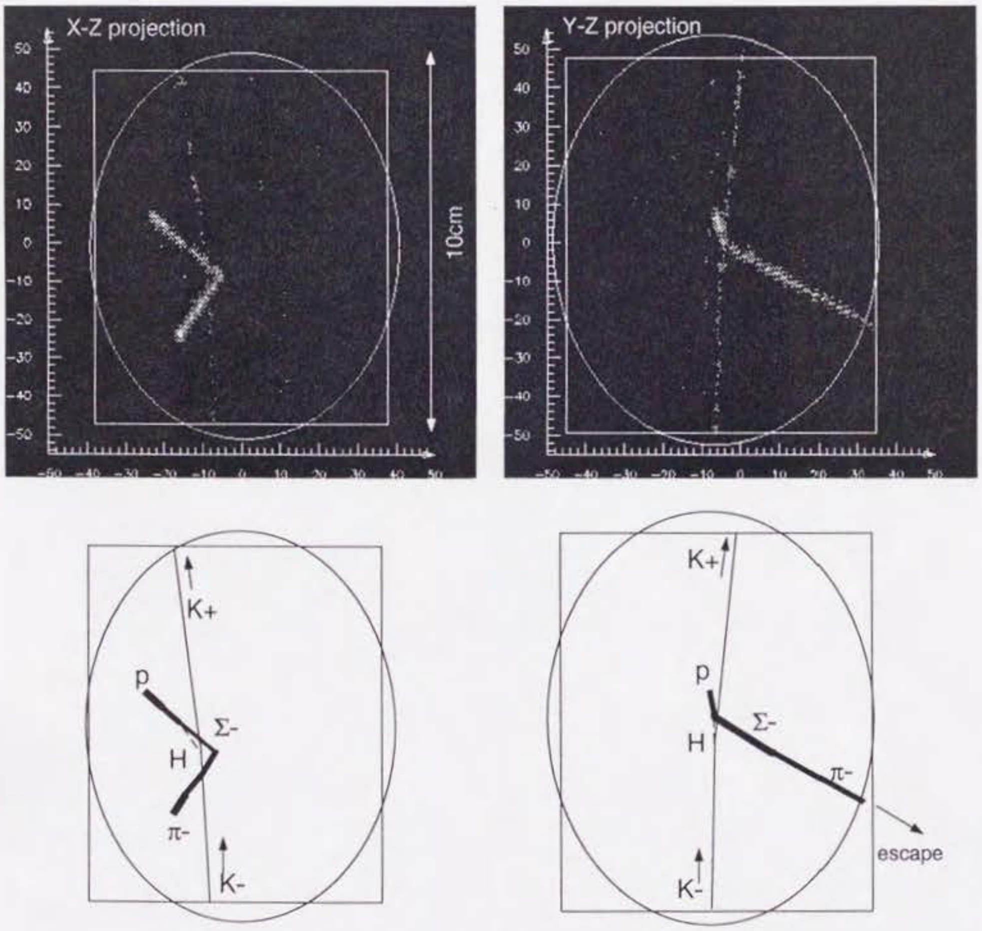


Figure 36: A candidate of "kinked Vee-track": Event C

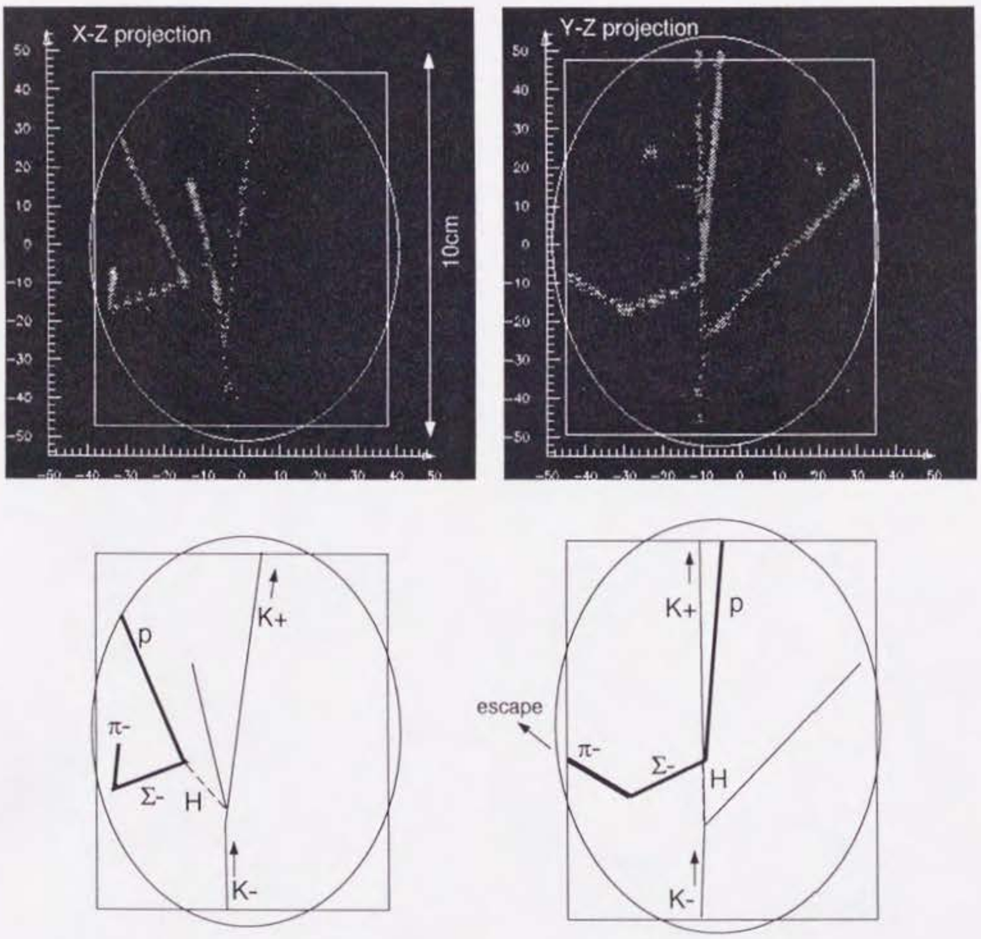


Figure 37: A candidate of "kinked Vee-track": Event D

The crossing point of the $K^-$ and $K^+$ tracks gives the $(K^-, K^+)$ interaction point. In the events B and D other tracks are associated at the $(K^-, K^+)$ interaction points where the position is determined within the accuracy of 1mm. The intersection of the $K^-$ or $K^+$ tracks in the decay plane determined by the two tracks which form the "Vee-track" also gives the $(K^-, K^+)$ interaction point within the accuracy of 1mm along x and y axes and 4mm along z axis. We have used the position determined by the method for the event A and C. The positions of $(K^-, K^+)$ interaction points determined by the different methods agree with each other for all the four candidates within the resolutions.

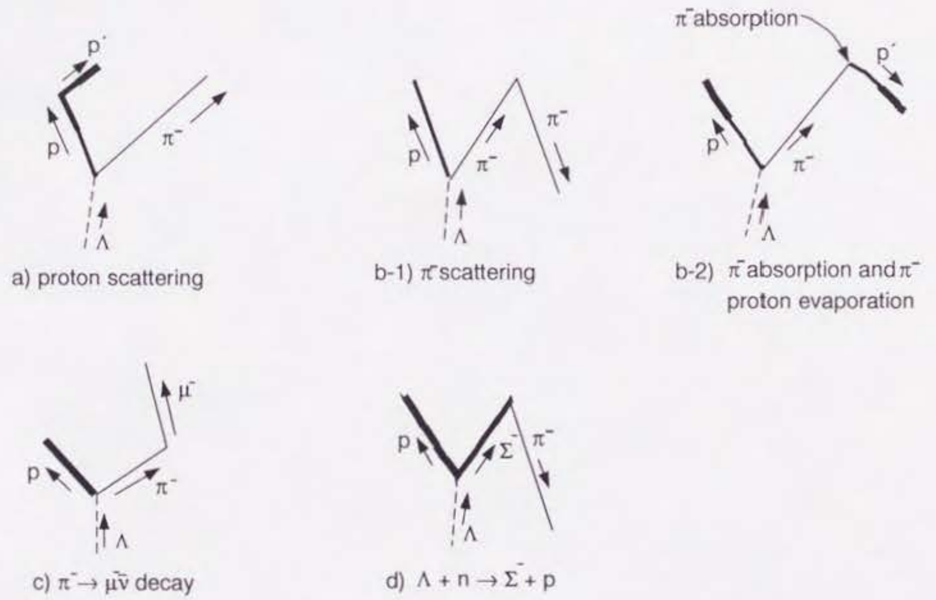


Figure 38: Possible fake events for $H \to \Sigma^- p$.

We have considered the mechanism which fakes $\Lambda$ decays as the $H$ decay. In scanning of a "kinked Vee-track" we have observed 194 $\Lambda$ events ("Vee-track"), in which 173 events are associated with one prong at the $(K^-, K^+)$ vertex indicating the $\Xi^-$ decay at short distance. The $\Lambda$'s can be produced also in the following reactions;

$$\Xi^- + p \to \Lambda + \Lambda, \tag{19}$$

$$\Xi^- + p \to \Sigma^0 + \Lambda \quad \Sigma^0 + \Sigma^0, \quad \text{then} \quad \Sigma^0 \to \Lambda + \gamma, \tag{20}$$

$$\Xi^- + p \to \Xi^0 + n, \quad \text{then} \quad \Xi^0 \to \Lambda + \pi^0. \tag{21}$$

There are several possibilities to fake "kinked Vee-track" event as shown in Fig. 38. These possibilities must be eliminated. The cases a) and b) are caused by the interaction of the proton or $\pi^-$. The case c) is caused by the inflight decay of the $\pi^-$ into $\mu^-$. The probability of these cases has been estimated by using a Monte Carlo simulation. We have found that 0.55% of $\Lambda$'s from $\Xi^-$ decays fakes the "kinked Vee-track" due to the interaction of decay products, proton or $\pi^-$, and that 0.05% of the $\Lambda$'s fakes due to $\pi^- \to \mu^- \bar{\nu}$ decay. Therefore, number of fake "kinked Vee-track" is expected to be 1.2 events from $\Lambda$'s from $\Xi^-$ decays. They are able to be eliminated by examination using the kinematics of the $H$ decay. The $\Lambda$ interaction shown in Fig. 38-d) is rather serious, but the momentum of $\Lambda$ from $(K^-, K^+)$ reaction is around 500 MeV/$c$ which is lower than the threshold momentum, 670 MeV/$c$ for this reaction. Assuming that the cross section of the reaction $\Lambda + n \to \Sigma^- + p$ is about 100 mb, the probability of the reaction for $\Lambda$'s from $\Xi^-$ decays has been estimated to be less than $10^{-4}$. We have found the fake events via the process is less than 0.02 events, which is negligibly small.

### 4.4.1 Kinematical constraints on the $H$ candidates

We have examined the four candidates using kinematical constraints on the $H \to \Sigma^- p$ decay to separate from the background events. The first one is the "visible momentum" of the $H$ which is reconstructed by using the ranges and the emission angles of the assumed $\Sigma^-$ and proton. The minimum energy of a particle can be measured with its flight length in the SCIFI-target as described in Section 3. It is called "visible energy".

The visible energy is equal to the kinetic energy of the particle if the particle stopped in the SCIFI-target. If the particle decays or escapes from the target, the visible energy is smaller than the real kinetic energy. The visible energy of the $\Sigma^-$, $T_\Sigma$, is obtained as described in Section 3;

$$T_\Sigma = a \cdot R_\Sigma^b, \tag{22}$$

where $R_\Sigma$ is the decay length of the $\Sigma^-$. The constant $a$ and $b$ are explained in Section 3. The visible momentum of $\Sigma^-$, $p_\Sigma^{vis}$, is obtained from $T_\Sigma$ and the rest mass of the

$\Sigma^-$, $M_\Sigma$ as;

$$p_\Sigma^{vis} = \sqrt{(T_\Sigma + M_\Sigma)^2 - M_\Sigma^2}. \tag{23}$$

The visible momentum of $H$ is obtained from $p_\Sigma^{vis}$, and the decay angles of the $\Sigma^-$ and the proton, $\theta_\Sigma$, $\theta_p$ as,

$$p_H^{vis} = p_\Sigma^{vis} \cdot (\cos\theta_\Sigma + \sin\theta_\Sigma / \tan\theta_p). \tag{24}$$

The visible momentum which is calculated by the same method with the hypothesis that the "kinked Vee-track" corresponds to the $\Lambda \to p\pi^-$ decay. The results of $p_H^{vis}$ and $p_\Lambda^{vis}$ are listed in Table 6. The $p_H^{vis}$ for the events A,B,C, and D against the $K^+$ momentum are shown in Fig. 39. The dashed line shows the kinematical limit of the momentum of $H$ calculated for the following process which has the maximum Q-value;

$$K^- +^{12} C \to K^+ +^{10} B + H. \tag{25}$$

We have found that the two events A and D are inconsistent with the $H \to \Sigma^- p$ hypothesis. With the $\Lambda \to p\pi^-$ hypothesis, the visible momenta of the two events, A and D, are consistent with a typical momentum of $\Lambda$ from $(K^-, K^+)$ reaction.

| event | a) $p_H^{vis}$ $(MeV/c)$ | b) $p_\Lambda^{vis}$ $(MeV/c)$ |
|---|---|---|
| A | 1343 ± 242 | 266 ± 120 |
| B | 1155 ± 600 | 228 ± 154 |
| C | 772 ± 409 | 151 ± 90 |
| D | 1926 ± 261 | 378 ± 73 |

Table 6: a) The visible momentum of the $H$ ($p_H^{vis}$) reconstructed from the visible energies of $\Sigma^-$ and proton. b) The "visible momentum" of $\Lambda$ ($p_\Lambda^{vis}$) obtained by the same method under the hypothesis that the $\Lambda \to p\pi^-$ decays produced "kinked Vee-track"s (see the text).

The second constraint is the "visible momentum balance" of the $\Sigma^-$ and proton from the $H$ decay. The visible momenta of the $\Sigma^-$ and proton are obtained from their flight lengths ;

$$p_\Sigma^{vis} = \sqrt{(T_\Sigma + M_\Sigma)^2 - M_\Sigma^2}, \tag{26}$$

$$p_p^{vis} = \sqrt{(T_p + M_p)^2 - M_p^2}, \tag{27}$$

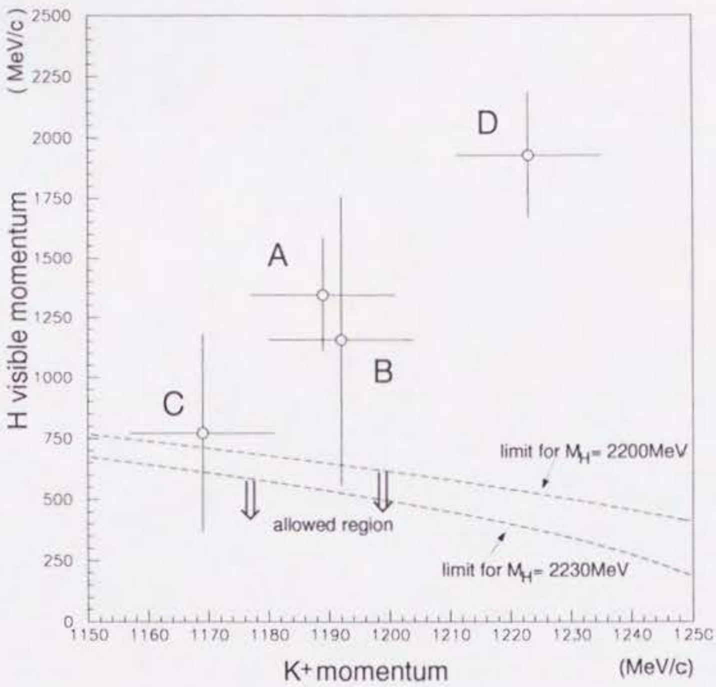


Figure 39: The scatter plot of the visible momentum of the $H$ and the momentum of $K^+$. The dashed lines correspond to kinematically allowed limits for the direct $H$ production. Th upper line corresponds to the $H$ mass of 2200 MeV/$c^2$ and the lower line to 2230 MeV/$c^2$. The areas below the dashed lines are allowed regions.

where $T_\Sigma$ and $T_p$ are the visible energies of $\Sigma^-$ and proton obtained from their flight lengths, respectively. The visible momentum balance, $\Delta p_H^{vis}$, is defined as;

$$\Delta p_H^{vis} = p_p^{vis} \cdot \sin\theta_p - p_\Sigma^{vis} \cdot \sin\theta_\Sigma. \tag{28}$$

If the proton stops in the SCIFI-target, the $\Delta p_H^{vis}$ should be a positive value, since the $p_p^{vis}$ for the stopped proton is equal to the initial momentum, while the $p_\Sigma^{vis}$ for the decaying $\Sigma^-$ is always underestimated. The $\Delta p_H^{vis}$ has been calculated for three events A,B and C in which protons have stopped in the SCIFI-target. The $\Delta p_\Lambda^{vis}$ is the visible momentum balance which is calculated by the same method with the hypothesis of $\Lambda \rightarrow p\pi^-$. The results are listed in Table. 7. The correlation between $\Delta p_H^{vis}$ and the decay opening angle is shown in Fig 40. The region H and $\Lambda$ show kinematically allowed region with 90% confidence level. The area H corresponds to the decay $H \rightarrow \Sigma^- p$, and the area $\Lambda$ corresponds to the region due to $\Lambda \rightarrow p\pi^-$. The three events A,B and C are not consistent with the $H$ but consistent with the $\Lambda$. By combining the kinematical constraints discussed above, we have concluded that all the 4 events A,B,C and D are fake events due to the $\Lambda$ decays. Therefore, there remains no candidate of the $H \rightarrow \Sigma^- p$ decay.

| event | a) $\Delta p_H^{vis}(MeV/c)$ | b) $\Delta p_\Lambda^{vis}(MeV/c)$ |
|---|---|---|
| A | -367 $\pm$ 91 | -12 $\pm$ 62 |
| B | -225 $\pm$ 65 | 20 $\pm$ 52 |
| C | -215 $\pm$ 57 | 22 $\pm$ 45 |

Table 7: The "visible momentum balance" for a) $H \rightarrow \Sigma^- p$ decay and b) $\Lambda \rightarrow p\pi^-$ decay.

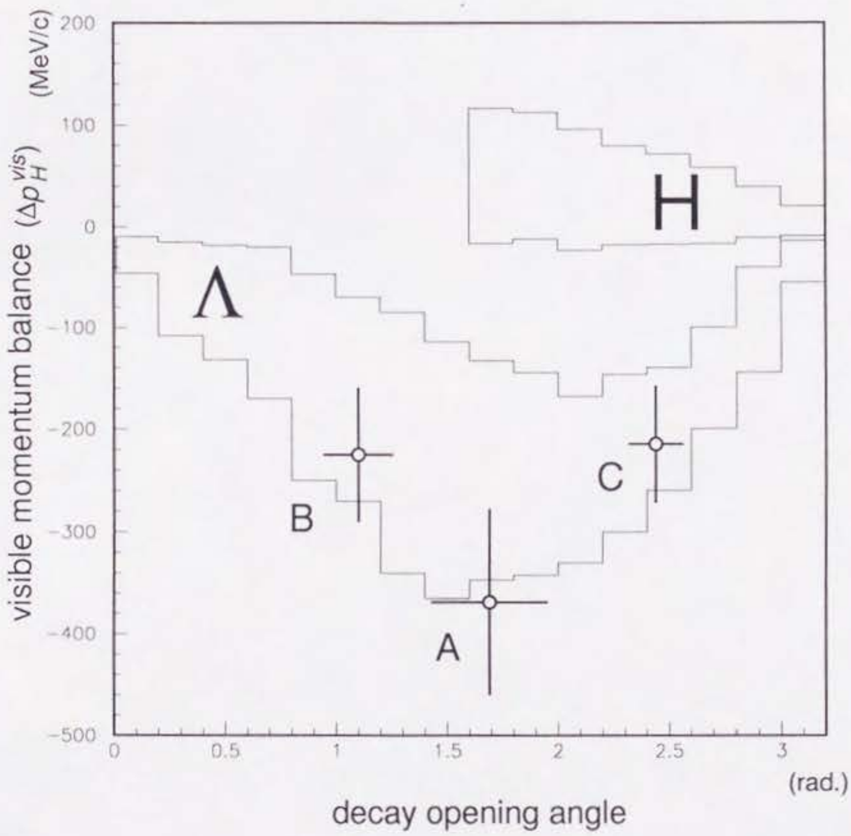


Figure 40: The "visible momentum balance" is plotted against the decay opening angle. The area H and $\Lambda$ show kinematically allowed regions which are derived from the Monte Carlo simulation. The area H corresponds to the decay $H \to \Sigma^- p$ with the $H$ mass of 2230 MeV/$c^2$, and the area $\Lambda$ corresponds to the decay $\Lambda \to p\pi^-$. The boundaries shown by the solid lines has 90% confidence level for the decays.

## 5 Results and discussion

We have searched for the $H$ in the decay products of the reaction, $K^- + C \rightarrow K^+ + H + X$ , in the SCIFI-data. The "kinked Vee-track" topology corresponding to the sequential weak decay, $H \rightarrow \Sigma^- + p$ followed by $\Sigma^- \rightarrow \pi^- + p$, has been searched for. Possible four candidates have been remained after scanning the SCIFI-data where the $K^+$ momentum is higher than 1150 MeV/$c$. We have rejected all the four events as the fakes of $\Lambda \rightarrow p\pi^-$ decay by means of the examination using the decay kinematics. From the null observed candidate the upper limit for the production cross section is obtained as;

$$Br \cdot \sigma_H \leq \frac{2.30}{N_{(K^-,K^+)} \cdot \eta_H} \cdot \sigma_{(K^-,K^+)}, \tag{29}$$

where $Br$ is the decay branching for $H \rightarrow \Sigma^- p$. The $\eta_H$ is the detection efficiency for the decay $H \rightarrow \Sigma^- p$ as described in Section 4.3. The upper limit for the $\sigma_H$ depends on the mass and the lifetime of $H$. The $\sigma_{(K^-,K^+)}$ is the differential cross section of the $(K^-, K^+)$ reaction at 0 degree on $(CH)_n$ target with $P_{K^+} \geq 950$ MeV/$c$. The absolute cross section has been obtained for $K^+$ momentum greater than 950 MeV/c (8,294 events). The cross section of the $(K^-, K^+)$ reaction has been taken from the experimental results in which the nuclear mass number dependence of the reaction was measured for various nuclear targets[45]. The 10% uncetainity of the measured cross section has not been included here. The possibility that the produced $\Xi^-$ escapes from the target nucleus[41] stops outside of the nucleus[42] and is absorbed in another nucleus is about 3% of the total $(K^-, K^+)$ reactions. Therefore, our measurement includes the production of $H$ through the process. However, it does not affect the final result of the upper limit for the direct $H$ production cross section, because no candidate of the $H$ production has been found. The results are shown as a function of the lifetime of $H$ in Fig. 41, and as a function of the $H$ mass in Fig. 42.

According to the prediction by Jaffe with the MIT bag model [2], the branching-ratios of the $H$ which decays into 2 baryons are expected as $\Sigma^- p : \Sigma^0 n : \Lambda n = 5 : 3 : 2$. If the $H$ mass is greater than 2190 MeV/$c^2$, the decay $H \rightarrow \Lambda p \pi^-$ is also allowed. However, the branching of this decay is suppressed by the kinematical phase factor for the mass near 2200 MeV/$c^2$.

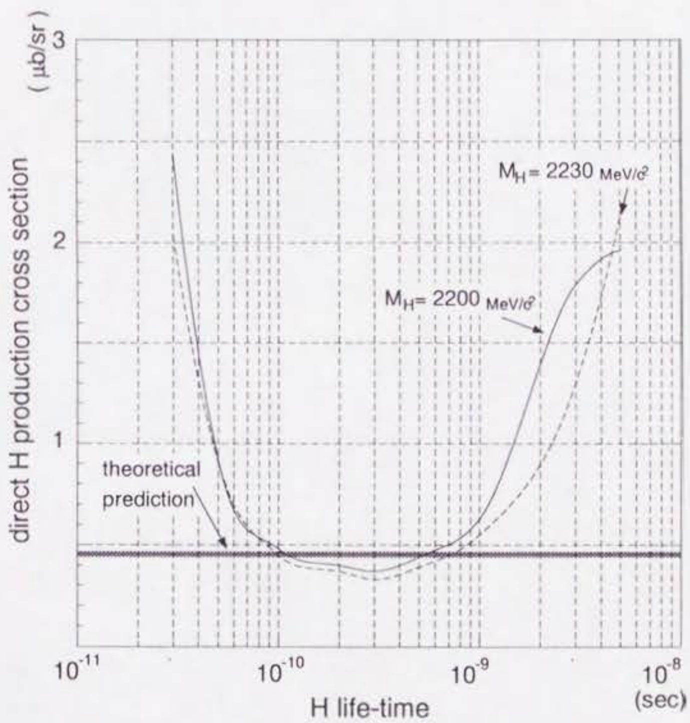


Figure 41: The obtained upper limit for the cross section of the direct $H$ production as a function of the lifetime is shown. The branching for the decay $H \rightarrow \Sigma^- p$ is assumed to be 100%. The solid line corresponds to $M_H$=2200 MeV/$c^2$, and the dashed line corresponds to $M_H$=2230 MeV/$c^2$. The straight line shows a theoretical prediction of the cross section.

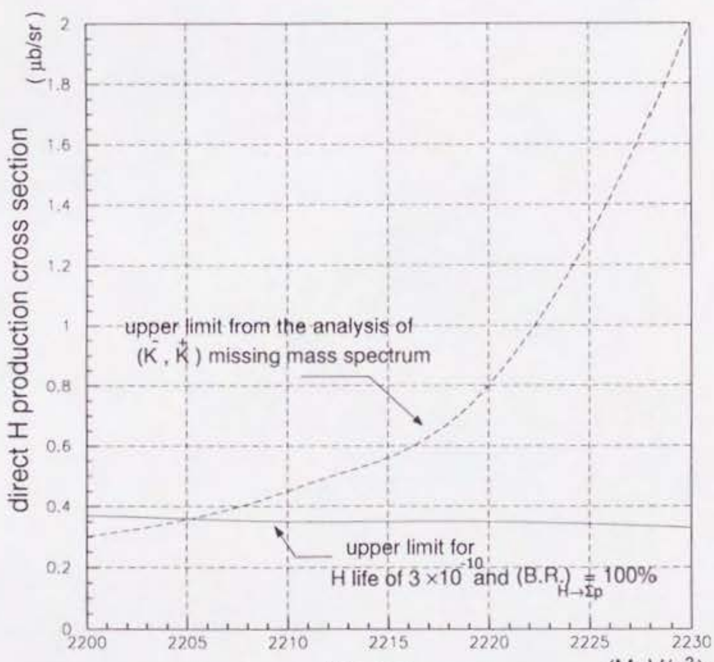


Figure 42: The upper limit for the cross section of the direct $H$ production as a function of the mass of $H$ with the lifetime of $3\times10^{-10}$ sec is shown by the solid line. The branchings for the decay $H \rightarrow \Sigma^- p$ is assumed to be 100%. The dashed line shows the upper limit of the cross section deduced from only the missing mass spectrum of the $(K^-, K^+)$ reaction (90% C.L.) obtained in this experiment in Ref.[42, 44].

It is difficult to assume the value of the branching-ratio $Br$ from the present theoretical works. Accordingly, the obtained upper limit is presented here assuming the branching ratio for the decay $H \rightarrow \Sigma^- p$ to be 100%. The upper limit is found to be to 0.3 $\mu$b to 0.5 $\mu$b with the $H$ lifetime of $10^{-10}$ sec to $10^{-9}$ sec. The result is insensitive to the $H$ mass in the region higher than 2200 MeV/$c^2$ as shown in Fig. 41. The theoretical prediction using the method of Arts and Dover [19] is also shown in Fig. 41. The obtained upper limit is of the same order as the predictions for the $H$ with the lifetime of $10^{-10}$ to $10^{-9}$ sec and with assumption that the decay branching for $\Sigma^- p$ is 100% . The obtained upper limit is plotted as a function of the $H$ mass for the lifetime of $3\times10^{-10}$ sec in Fig. 42. The direct $H$ production in this mass region was also searched for by the analysis of the missing mass spectrum of $(K^-, K^+)$ reaction in the experiment [42, 44] performed simultaneously with this experiment. It provided the upper limit without assumption of the decay branching-ratio of the $H$. The dashed curves in Fig. 42 show the results.

The present results which have been obtained by searching the decay of $H$ in the SCIFI-data put the new limit for the $H$ near the $\Lambda\Lambda$ threshold (2200 MeV/$c^2 \leq M_H \leq$2230 MeV/$c^2$). It has been shown that the direct $H$ production in this mass region is rejected by means of the analysis of missing mass spectrum as well as the searching for the decay products in the SCIFI-data.

# 6 Conclusion

The $H$ dibaryon search via $(K^-, K^+)$ reactions with the $K^-$ momentum of 1.66 GeV/$c$ has been performed at KEK 12-GeV Proton Synchrotron. In the present experiment a newly developed detector, SCIFI-target have been used as a visual detector in order to detect the image of $(K^-, K^+)$ reactions followed by the $H$ decay into $\Sigma^- p$ in the target. A $K^+$ spectrometer which tags the $(K^-, K^+)$ reactions has been used to confirm double strangeness transfer in the SCIFI-target. The SCIFI-target consists of 30,000 plastic scintillating fibers which are viewed by two sets of image intensifier tubes from the orthogonal directions providing three-dimensional information of the tracks. The tracks have been clearly identified as sequences of bright spots. The position resolution of the centroid of spot has been obtained to be 290 $\mu$m.

The $H$ dibaryon through the direct production process, $K^- + C \to K^+ + H + X$ followed by the sequential weak-decay, $H \to \Sigma^- + p$, then $\Sigma^- \to \pi^- + n$ , has been searched for in about 8,000 pictures of $(K^-, K^+)$ reactions tagged with the $K^+$ spectrometer having the momentum resolution of 0.5% and the mass resolution of 18.5 MeV/$c^2$ for $K^+$'s of 1.1 GeV/$c$.

The candidates of the possible $H$ decays into $\Sigma^- p$ have been examined whether the decay kinematics are satisfied by the visible energy determined from the ranges of decay products. No candidate of the $H$ decay has been found. The upper limit of the production cross section of $H$ decaying into $\Sigma^-$p has been obtained to be 0.35 $\mu$b to 0.5 $\mu$b for the $H$ with the mass of 2200 to 2230 MeV/$c^2$ and the lifetime of $10^{-10}$ to $10^{-9}$ sec.

The SCIFI-target has played important roles in this experiment owing to its unique feature as the triggerable visual detector. It has been worked as an active target providing three-dimensional information on $(K^-, K^+)$ interaction vertexes, which has been used to reject background reactions such as neutral kaon productions. It has been also used to detect weak decay products of hyperons such as
$Xi^-$, $\Lambda$ and the $H$ produced via $(K^-, K^+)$ reactions. In addition, the method of kinematical cuts has been successfully applied to separate the $H$ decays from the background events due to $\Lambda$ decays using the SCIFI-target.

In the present experiment the scintillating fiber has been used as an active target for the first time, and such a triggerable vertex detector has been proved to be useful, and the method for applying it to the scattering experiment has been established. Several kinds of experiments of hyperon-neucleon scattering has been performed and planned by using the SCIFI-target [46, 47, 48]. We believe that it will open a new field of particle and nuclear physics in future.

# Acknowledgements

It is my great pleasure to express heartfelt thanks to many people for their collaboration, advice and encouragement during the present work. Also I would like to acknowledge all the person who gave me the opportunities to work on the particle and nuclei physics in my years of graduate school.

First of all, I would like to address my sincere thanks to Prof. Akira Masaike who has been my supervisor. He gave me a chance to start my life of physicist in my days of under-graduate and graduate school. He started the Group for Particle & Nuclei Physics in Kyoto University as a new activity of experimental physics which opens a new field where the various categories of physics such as elementary particle physics, nuclear physics, low-temperature physics and astro physics, have crossed over each other. The present work entirely owe to his spirits for physics and leader-ship in this group. I am very happy to be a member of his group.

I would like to express my thanks with grate respect to Prof. Ken'ichi Imai who is the spokesman of two experiments which I have participate. He introduced the hadron physics with strangeness quantum number and opened my eyes to the exciting subject of exotic hadron physics through the experiments. He is also a great innovator who initiates the SCIFI-target presented in the work. It is my great pleasure that he gave me a chance to realize this novel electric bubble chamber. He has always shown me the way to the successful goal with his keen insight for the physics.

I would like to thank to Prof. Hideto En'yo for his powerful support and tireless devote to this work. He has provided his skillful technic and unique idea during the construction, data taking, and analysis. Also he encouraged me so many times with his aggressive and tough attitude in the present work. The present experiment could be hardly carried out without his countless efforts.

I would express my gratitude to all the members of E224 collaboration. I would thank to S.Yamashita for his great effort on the spectrometers and the careful analysis of $K^+$'s. I'd like to thank M.S.Chung for the calibration of the SCIFI-data and his tough work on the analysis of $\Xi^-$ productions. I am grateful to Y.Goto for on-line and off-line programs as well as many useful suggestions for the analysis of SCIFI-data. I'd like to thank to H.Funahashi for his masterpiece, the aerogel Čerenkov counters, R.Takashima and M.Iinuma for their hard works on the TOF counters, P.Tlusty for his expertise in the experiment which always helped us, M.Sekimoto, Y.Matsuyama, N.Saito for the construction of chambers and S.Makino, S.Yokkaichi, M.Yoshida, R.Susukita, S.Mihara, Y.Matsuda and other members of the Group for Particle & Nuclei Physics for many contributions. Also I would like to express my thanks to beautiful Miss. Mari Hayashi, who is a secretary of our group, for her kindhearted supportment. I would like to thank S.Aoki who made the image digitizers. No one could carry out this experiment without his digitizers. Also thank to T.Yoshida for contribution for the mass trigger and T.Iijima for many precious suggestions and encouragements. I would address heartfelt thanks to Prof. C.Nagoshi for the tough work on the SCIFI-data analysis and also for her hearty encouragement with delicious foods. Also thanks to Prof. F.Takeutchi, A.Higashi, K.Omata and I.Nomura for the various supports and suggestions.

It is my pleasure to address grateful thanks to Prof. Y.M.Shin and Prof. K.S.Sim for giving us a good opportunity to work with many Korean physicists. Also thank to Korean collaborators, J.M.Lee, K.S.Chung, I.S.Park and J.K.Ahn for their devoted contributions and friendship.

This work was supported by many staffs of KEK. Their devotion was strongly appreciated. I explain thanks to Prof. K.Nakai who was the head of the physics division of the KEK-PS for many supports and suggestions. I would thank to people of Beam Channel Group, M.Takasaki, K.Tanaka, Y.Yamanoi, especially to M.Ieiri, who is also the collaborator, for their hard works to maintain the beam line day and night. I also would thank to people who supported the hardware and software for data taking, M.Nomachi, Y.Yasu, H.Kodama, T.Osuka, O.Sasaki for the various support.

I'd like to express thanks to Prof. T.Fukuda for his helpful suggestions on the hyper-nuclear physics which make the present work match more fruitful. Also many theorists who support the present work are strongly appreciate. I'd like to thank Prof. Yazaki, Prof. Akaishi, Prof. Y.Yamamoto, Prof. T.Motoba, Prof. M.Oka, and Prof. S.Takeuchi for the countless discussions and suggestions for the $H$ particle and hyper-nuclei physics. Also I would appreciate for two great theorists, R.Jaffe and C.B.Dover who suggested the $H$ search experiment.

I would thank to Prof. K.Niwa, M.Nakamura, T.Nakano, H.Tajima, H.Togawa and S.Nakanishi who were the collaborator of the previous emulsion experiment for the $H$ search. It is my great pleasure to work with them at my initiation of particle physics. I am indebted to Prof. A.Konaka, who is the first innovator of the SCIFI-target, for his early works for the developments.

I owe to express my acknowledgments to the companies, KURARY, Delft and HAMAMATSU for their powerful support to the present work. I would appreciate to Japan Society of Promotion of Science for the financial support which helped the present work strongly.

Finally I thank my parents and friends for their hearty support and continuous encouragement, by which I have been able to spend the happiest time of my life.

# Appendix

## A.1 Position calibration of the image data

We describe the method of the position calibration of the SCIFI-data. There are three sources which affect the position resolution. The first one is a so-called pin-hole distortion of the images due to the electro-static lens of the IIT. The second one is the distortion of the images due to the fringing magnetic field of the spectrometer which affect the orbit of photoelectrons in the electric-focusing lens. The third one is the miss-alignment of the fiber sheets. Each effect was corrected separately by using the reference pictures as shown in Fig. 43 and the pictures of straight tracks of minimum ionizing particles.

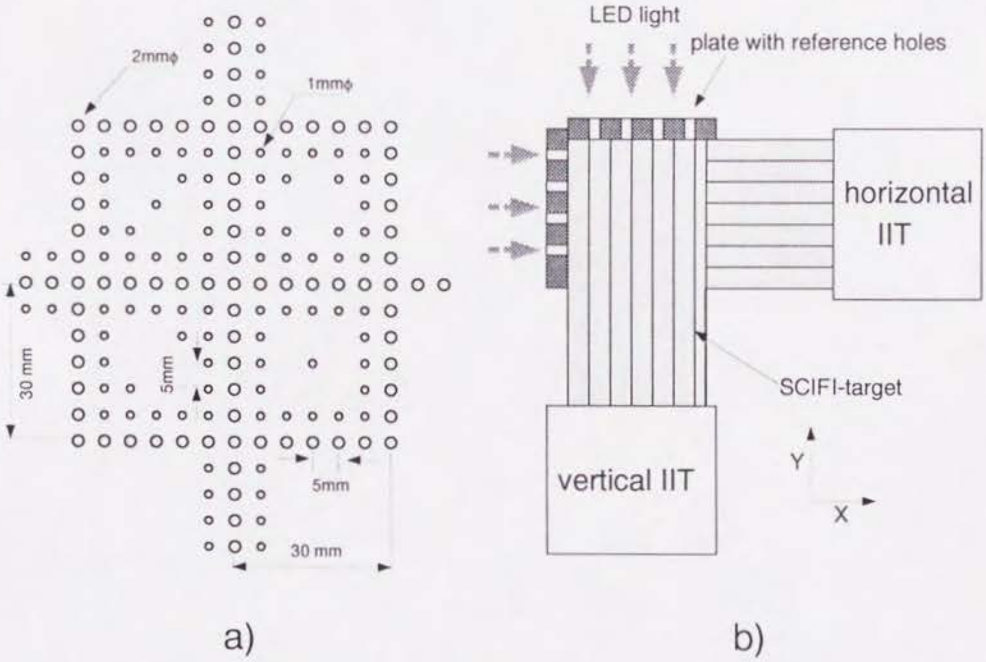


Figure 43: The position calibration system for the SCIFI-data which generated a reference picture with the LED light. The plate with reference holes is shown in a) and the setup is schematically shown in b).

### A.1.1 Correction of pin-hole distortion

A pin-hole distortion in the X-Z projection is described in the following formula;

$$\begin{pmatrix} x_{pin} \\ z_{pin} \end{pmatrix} = (1 + a_1 r + a_3 r^3 + \cdots) \begin{pmatrix} x_{real} - x_c \\ z_{real} - z_c \end{pmatrix} + \begin{pmatrix} x_c \\ z_c \end{pmatrix}, \tag{1}$$

where $x_{real}$ and $z_{real}$ are the real positions, and $x_{pin}$ and $z_{pin}$ are the positions in the distorted image. The distortion depends only on $r$, the distance from the optical center of the IIT ($x_c$,$z_c$) to the real positions ($x_{real}$,$z_{real}$), i.e.;

$$r = \sqrt{(x_{real} - x_c)^2 + (z_{real} - z_c)^2}. \tag{2}$$

The same relation holds for the Y-Z projection. Figure 44 shows the distorted image of the reference picture which was taken without the magnetic field.

The $x_{real}$ and $z_{real}$ are calculated from the CCD integer coordinates ($I_{x-CCD}$, $I_{z-CCD}$) with the following formula;

$$\begin{pmatrix} x_{real} \\ z_{real} \cdot \eta_{shrink} \end{pmatrix} = \eta_{mag} \cdot \begin{pmatrix} I_{x-CCD} \cdot \Delta x_{pxl} \\ I_{z-CCD} \cdot \Delta z_{pxl} \end{pmatrix} + \begin{pmatrix} x_{off} \\ z_{off} \end{pmatrix}, \tag{3}$$

where $\Delta x_{pxl}$ and $\Delta z_{pxl}$ are the sizes of the CCD pixels, $11\mu$m and $13\mu$m, respectively. Here $\eta_{mag}$ is the demagnification factor from the fiber output to the CCD and the $\eta_{shrink}$ is the demagnification factor along the Z-axis due to shirking of the sheet-gap at the read-out position of the SCIFI-target. The $x_{off}$ and $z_{off}$ are the offset parameters to cope with the alignment between the CCD camera and the IIT.

Combining the Equation (1) and (3), the parameters $a_1, a_3, x_c, z_c, z_{off}$ and $x_{off}$ were deduced using the MINUET package to minimize the difference between the observed positions and the hole positions. The result of the correction is also shown in Fig. 44.

### A.1.2 Correction of distortion due to the magnetic field

The effect of the fringing magnet field on the image of gaps of fiber-sheets is shown in Fig. 45, where the pin-hole distortion has been already corrected. The effect is more serious in the X-Z picture than in the Y-Z picture. The photoelectrons moved helically at the electro-static lens on the first stage of the IIT due to the magnetic field component parallel to the IIT axis. We assume that the amount of rotation of

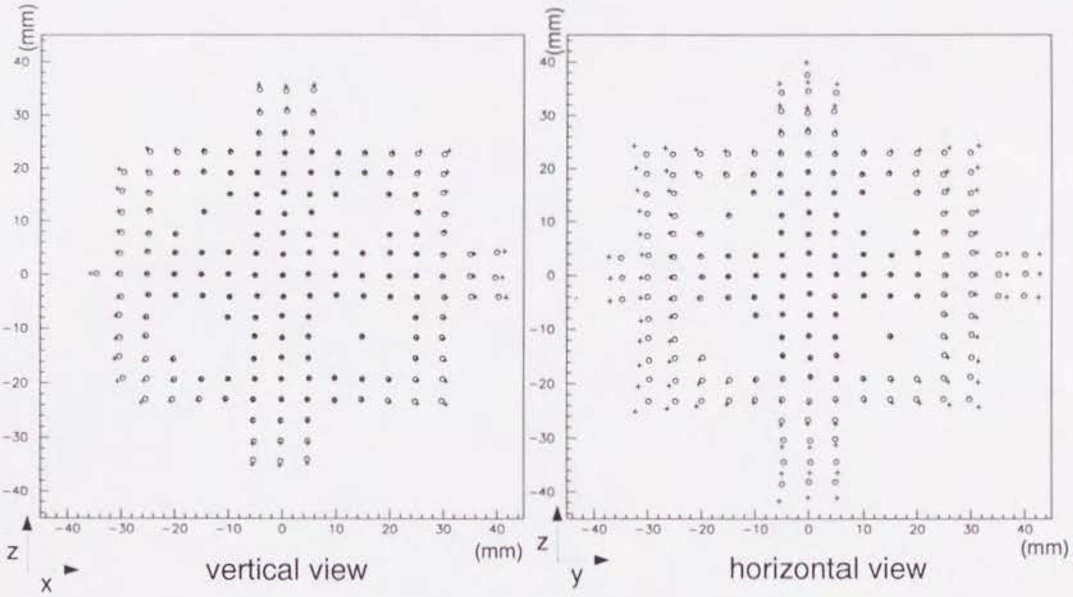


Figure 44: The pin-hole distortion and its correction. The crosses show the distorted positions, and the circles show the corrected positions.

photoelectrons depends mainly on the distance from the optical center of the IIT. The distortion effect can be written as;

$$\begin{pmatrix} x_{mag} \\ z_{mag} \end{pmatrix} = \begin{pmatrix} \cos\theta & -\sin\theta \\ \sin\theta & \cos\theta \end{pmatrix} \begin{pmatrix} x_{real} - x_c \\ z_{real} - z_c \end{pmatrix} + \begin{pmatrix} x_c \\ z_c \end{pmatrix}, \qquad (4)$$

where the $x_{mag}$ and $z_{mag}$ are the positions distorted by the magnetic field. The rotation angle $\theta$ depends on the distance from the center of the IIT. We found that the angle $\theta$ is not axially symmetric. We parametrize $\theta$ as;

$$\theta = (p_0 + p_1 r + p_2 r^2)\,(1 + \alpha\cos\phi + \beta\sin\phi + \gamma\cos\phi^2 + \delta\sin\phi^2),$$

where $r$ is the distance from the IIT center and $\phi$ is the angle around the IIT axis;

$$r = \sqrt{(x_{real} - x_c)^2 + (z_{real} - z_c)^2},$$

$$\phi = \arctan\left(\frac{x_{real} - x_c}{z_{real} - z_c}\right).$$

The parameters to be determined are $p_0, p_1, p_2, \alpha, \beta, \gamma$ and $\delta$. We have chosen the parameters so as to make the image of the fiber sheet straight using the MINUIT package.

The rotation and the curvature of the sheet-image have been observed as shown in Fig. 45. The distortion in the Y-Z picture is small compared to the X-Z picture. Similar to the X-Z projection, the Y-Z projection have been corrected so as to reconstruct the straight line of the fiber sheets.

### A.1.3 Misalignment of the fiber sheets

The misalignment of the fiber-sheets occurred in the stacking process. Figure 46 shows the images of the straight lines viewed through the scintillating fibers. The picture shows the misalignment of the fiber clearly. To correct this effect we observed tracks of minimum ionizing particles, and the photon clusters are binned into the unit of fiber sheet. Figure 47 shows the peak value of the residual distribution from the fitted track. The largest shift of the peak is $400\mu m$ which is comparable to the fiber size. We have made corrections on the fiber-sheet positions so as to compensate the observed shifts.

### A.1.4 Evaluation of the calibrations

To evaluate how well the calibrations have been made we have re-exmained the picture of the reference holes. The central positions of the holes are compared to the real positions of those as shown in Fig. 48. We have concluded that the systematic error $\sigma_{sys}$ for the position determination is about $200\mu m$, which includes uncertainty of the corrections of distortion, $\sigma_{dist}$, and remaining misalignment of the fiber-sheets, $\sigma_{align}$.

# Appendix

## B.2 GEANT simulation program

We have developed a Monte Carlo simulation program to evaluate the performance of the total system. On the first stage of the program the productions of $\Xi^-$ and $H$ through the quasi-free $(K^-, K^+)$ reactions in the SCIFI-target have been simulated. On the second stage the generated particles have been fed into the GEANT package to simulate the decay and the further reaction sequences and to generate

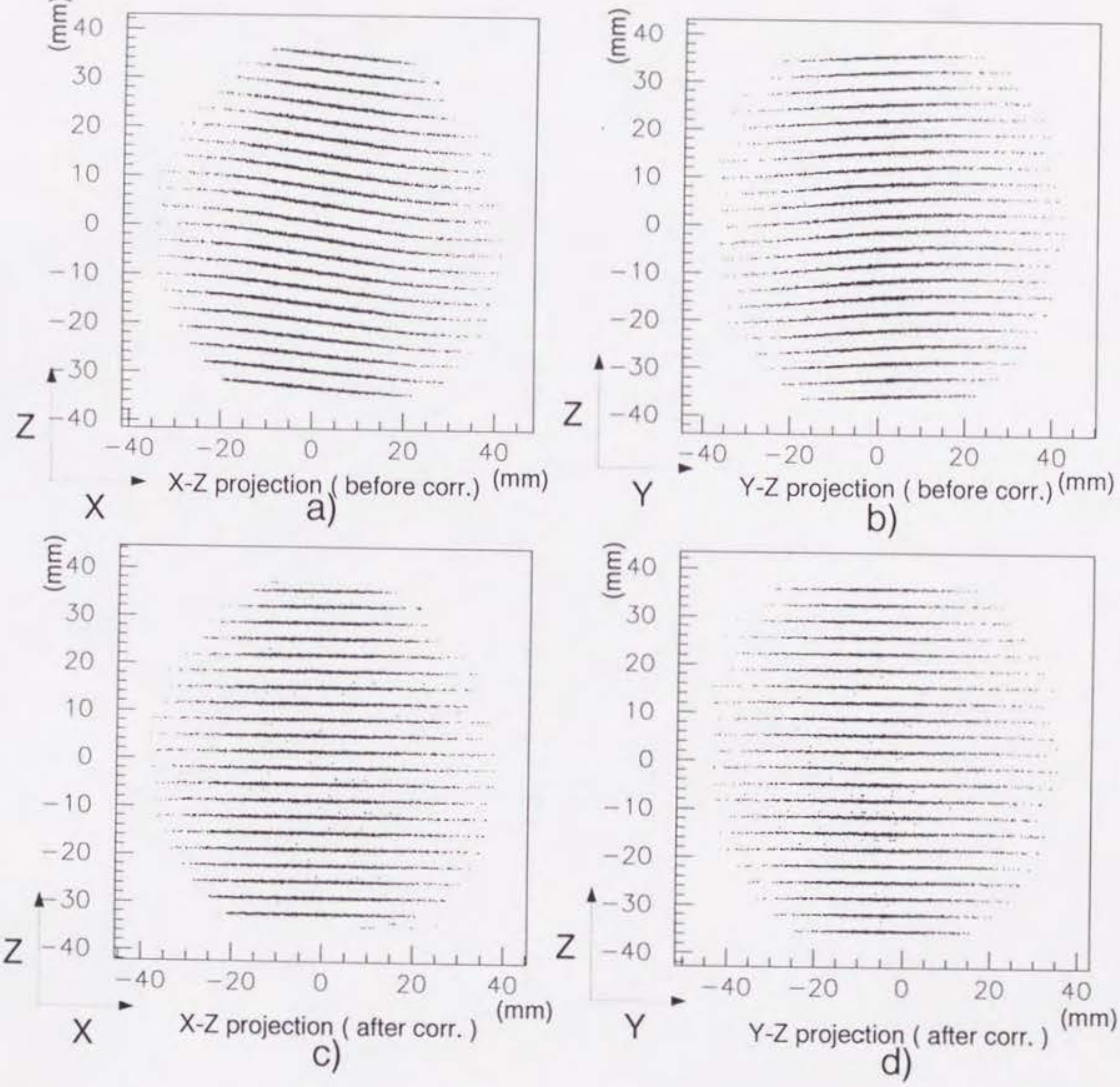


Figure 45: The images of the fiber sheets are shown. The pictures are obtained by accumulating photon clusters of many tracks. The pin-hole distortions of the pictures due to electric-static lens are corrected in this pictures. a) and b) show the images on X-Z projection and Y-Z projection, respectively, before the correction of the magnetic field effect. c) and d) show that after the correction

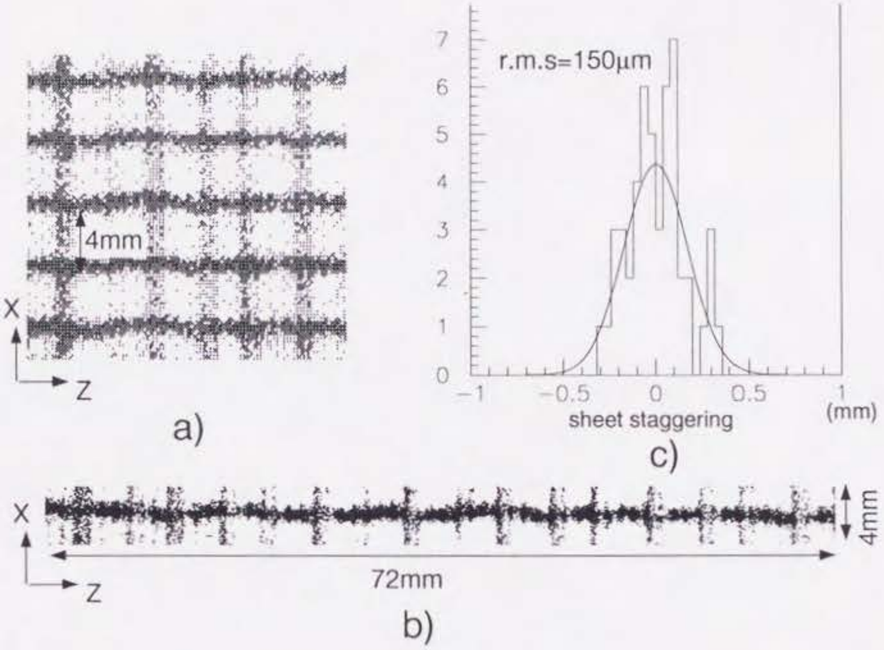


Figure 46: a) The typical image of straight lines viewed through the SCIFI-target. The miss-alignment of fibers makes the images of lines stagger. It is corrected to be a straight tracks. b) The distribution of typical fluctuation of alignment of the fiber-sheets.

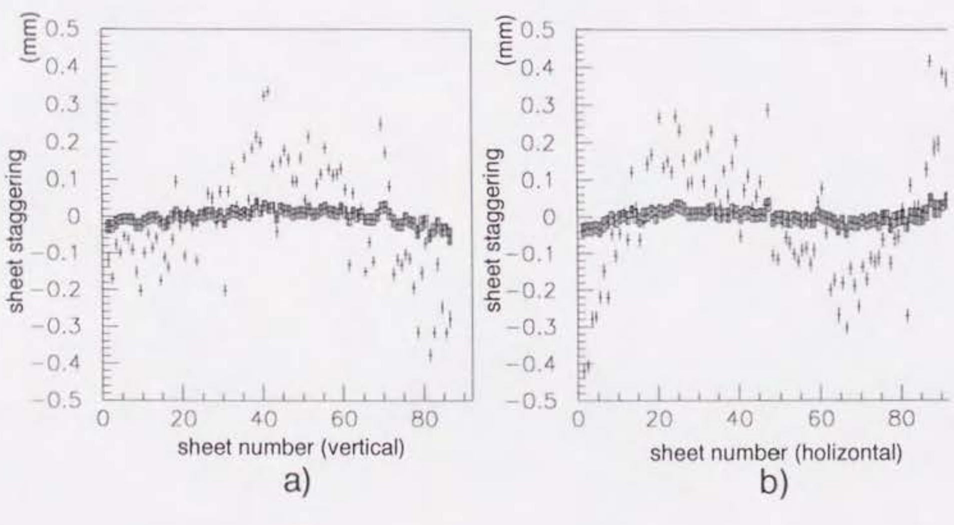


Figure 47: The distribution of the fluctuation of the fiber-sheets alignment obtained from the linear-fitting for MIP tracks, a) for the vertical IIT and b) for the horizontal IIT. The crosses shows the values before the alignment and the small boxes show after the alignment.

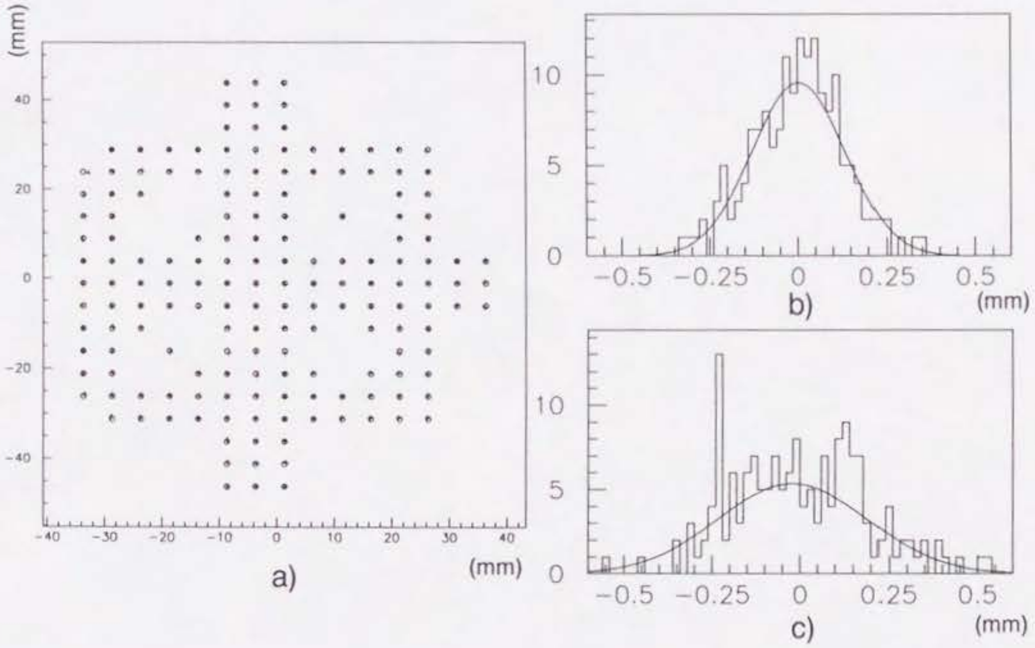


Figure 48: The evaluation of the residual distortion after all the corrections. a) The crosses are the corrected positions and the circles show the reference positions. The distances along the x-axis between the corrected positions and the reference positions are shown in b) and along the y-axis in c). The r.m.s's of the distributions are 130 $\mu$m for x and 200 $\mu$m for y.

simulated pictures which imitate the SCIFI-data in order to check the performance of the analysis by means of scanning.

The production kinematics has been calculated in the following 2-body reactions;

$$K^- + p \rightarrow \Xi^- + K^+, \tag{1}$$

$$K^- + (p) \rightarrow \Xi^- + K^+, \tag{2}$$

$$K^- + (pp) \rightarrow H + K^+, \tag{3}$$

where (p) and (pp) are a proton and a proton-pair inside a carbon nucleus, respectively. We have subtracted the nuclear potential, 7 MeV, from the rest mass of these protons. The fermi-motion has been introduced into the initial momentum of (p) and (pp) with the harmonic oscillator potential model. The output of the simulation has also been used to make a cross check on the detection efficiency of particles such as $\Xi^-$, $\Lambda$ and $H$. Using GEANT, the decay and interaction of generated particles have been included. The ionization in each scintillating fiber has been obtained, which is used to generate the simulated pictures as follows;

- To generate photons according to the ionization in each scintillating fiber. The number of photons are adjusted to reproduce the observed cluster density for a MIP track.
- To generate a photon cluster for each incident photon according to the measured cluster distribution as shown in Fig. 14. The center of the cluster position is smeared by the overall position resolution. The brightness of the cluster is given so as to reproduce observed data.
- The brightness of the photon cluster is distributed into the corresponding pixels on the CCD-chip.

In addition, the accidental incident particles have been mixed at the rate of 0.3 track per event to simulate the actual data situation. Detailed description of generating of the simulated picture is found in Ref. [43].

# References


[1] For detailed reviews, see Ann. Rev. Nucl. Part. Sci. **46** 332 (1990)

[2] R.L. Jaffe, Phys. Rev. Lett. **38**, 195 (1977)

[3] P.J.Mulders, A.T.Aerts, and J.J.de Swart, Phys. Rev. **D21** (1980) 2653

[4] K.F.Liu and C.W.Wong, Phys. Lett. **113B** (1982) 1.

[5] S.Takeuchi and M.Oka, Phys. Rev. Lett. **66** (1991) 1271.

[6] M.Oka, K.Shimizu and K.Yazaki, Nucl. Phys. **A464** (1987) 700.

[7] B.Sivestre-Brac, J.Carbonell and C.Gignoux, Phys. Rev. **D36** (1987) 2083.

[8] U.Straub, Z.Zhang, K.Bräuer, A.Faessler, S.B.Khadkikar and G.Lübeck, Nucl. Phys. **A508** (1990) 385c

[9] A.P.Balachandran, A.Barducci, F.Lizzi, V.G.J.Rodgers, and A.Stern, Phys. Rev. Lett. **52** (1984) 887.

[10] S.A.Yost and C.R.Nappi, Phys. Rev. **D32** (1985) 816.

[11] Y.Iwasaki, T.Yoshié and Y.Tsuboi, Phys. Rev. Lett. **60** (1988) 1371.

[12] A.S.Caroll et al., Phys. Rev. Lett. **41** (1978) 777.

[13] A.M.Badalyan and Yu.A.Simonov, Sov. J. Nucl. Phys. **36** (1982) 860.

[14] H.Ejiri et al., Phys. Lett. **B228** (1989) 24.

[15] B.Shahbazian et al., Z.Phys **C39** (1988) 151.

[16] B.Shahbazian et al., Phys. Lett. **B316** (1993) 593.

[17] A.N.Alekseev et al., Sov. J. Nucl. Phys. **52** (1990) 1016.

[18] K.Imai, Nucl. Phys. **A547** (1992) 199c-210c.

[19] A.T.M. Aerts and C.B. Dover, Phys. Rev. **D28**, 450 (1983)

[20] A.T.M. Aerts and C.B. Dover, Phys. Rev. **D29**, 433 (1984)

[21] S.Aoki et al., Phys.Rev.Lett. **65** (1990) 1729.

[22] S.Aoki et al., (in preparation).

[23] P.D.Barnes, Nucl. Phys. **A547** (1992) 3c.

[24] T.Iijima, *the Memoirs of the Faculty of Scinece, Kyoto University, Series A of Physics, Astrophysics, Geophysics and Chemistry*, 1995 (to be published), PhD thesis Kyoto Univ. 1995, unpublished.

[25] M.Danysz et al., Nucl. Phys. **49** (1963) 121.

[26] D.Powse, Phys. Rev. Lett. **17** (1966) 782.

[27] S.Aoki et al., Prog. Theor. Phys. **85** (1991) 1287.

[28] J.K.Ahn et al., Nucl. Phys. **A547** (1992) 211c-216c.

[29] A.R.Weindberg et al., Nucl Instr. Meth. **A283** (1989) 646.

[30] K.Kuroda et al., Nucl Instr. Meth. **A300** (1991) 259.

[31] P.Lendermann et al., Nucl Instr. Meth. **A344** (1994) 143.

[32] A.Cardini et al., Nucl Instr. Meth. **A346** (1994) 163.

[33] H.Burmeister et al., Nucl Instr. Meth. **A225** (1984) 530.

[34] J.Badier et al., Nucl Instr. Meth. **A337** (1993) 326.

[35] S.Dagoret et al., Nucl Instr. Meth. **A346** (1994) 137.

[36] A.Konaka et al., Nucl Instr. Meth. **A256** (1987) 70.

[37] M.N.Atkinson et al., Nucl Instr. Meth. **A225** (1984) 1.

[38] M.N.Atkinson et al., Nucl Instr. Meth. **A263** (1988) 333.

[39] C.Angelini et al., Nucl Instr. Meth. **A277** (1989) 132.

[40] J.K.Ahn et al., Nucl. Instr. Meth. (to be submitted).

[41] M.S.Chung, PhD thesis, Korea Univ. 1995, unpublished.

[42] S.Yamashita, *the Memoirs of the Faculty of Scinece, Kyoto University, Series A of Physics, Astrophysics, Geophysics and Chemistry*, 1995 (to be published), PhD thesis Kyoto Univ. 1995, unpublished.

[43] Y.D.Kim et al., unpublished.

[44] J.K.Ahn et al., Phys. Rev. Lett. (to be submitted).

[45] T.Iijima et al., Nucl. Phys. **A546** (1992) 588.

[46] KEK E251 experiment, M.Ieiri et al.

[47] KEK E289 experiment, M.Ieiri et al.

[48] BNL E885 experiment.